AN ABSTRACT OF THE THESIS OF

Brian A. Logue for the degree of Doctor of Philosophy in Chemistry presented on April 20, 2000. Title: The Role of Iron-Oxides in U(VI) Adsorption and the Kinetics of Contaminant Organic Reduction.

Redacted for Privacy

Abstract Approved: _____

John C. Westall

Contaminant transport in ground water is an important environmental process that affects a host of natural systems. Transport of contaminants is affected by many processes, including aqueous complexation, adsorption, and redox reactions. One of the most important components of an aquifer that controls transport is iron-oxide. In this study, the effect of iron-oxides on an inorganic radionuclide and representative organic contaminants were studied. Specifically, the role of iron-oxides in both the adsorption of U(VI) on natural iron-rich sands and the reduction of carbon tetrachloride (CT) and nitrobenzene (NB) by iron-oxide coated gold electrodes was investigated.

U(VI) was adsorbed to an iron-rich silica sand (containing appreciable amounts of Al) over a range of experimental conditions. It was found that the iron-oxide components of the heterogeneous sorbent were essential in determining the adsorption behavior of U(VI). Four mathematical models were investigated in an attempt to elucidate the advantages and disadvantages of applying the proposed models to adsorption data.

The effect of citrate on the adsorption of U(VI) by the iron-rich sand was also studied, with citrate generally decreasing the affinity of the sorbent for U(VI). Removal of highly reactive Fe and Al phases from the surface by citrate was investigated as a possible explanation of the adsorption behavior of U(VI). Alteration of the sorbent

surface by citrate was found to play a determining role in decreasing the adsorption capacity of the iron-rich sand for U(VI).

The rates of reduction of CT and NB by Fe(III)-oxide coated gold electrodes were studied to gain insight into what controls reduction reactions on zero-valent metals. Fe(III)-oxide films were deposited on gold electrodes, and Fe(II) sites were introduced into the films by controlled electrochemical reduction of a small fraction of the Fe(III) in the oxide. Mass transport kinetics were controlled through use of a well-defined flow-through system approximating a wall-jet electrode configuration. The results from this study support the view that the oxide film acts as a physical barrier, inhibiting direct contact between the gold electrode and the contaminant organics, increasing the diffusion path length through the film, and creating adsorption sites for the organic contaminants.

The Role of Iron-Oxides in U(VI) Adsorption and the Kinetics of
Contaminant Organic Reduction

By

Brian A. Logue

A THESIS

submitted to

Oregon State University

in partial fulfillment of
the requirements for the
degree of

Doctor of Philosophy

Presented April 20, 2000
Commencement June 2000

Doctor of Philosophy thesis of <u>Brian A. Logue</u> presented on <u>April 20, 2000</u>.

APPROVED:

Redacted for Privacy

Major Professor, representing Chemistry

Redacted for Privacy

Chair of Department of Chemistry

Redacted for Privacy

Dean of Graduate School

I understand that my thesis will become part of the permanent collection of Oregon State University libraries. My signature below authorizes release of my thesis to any reader upon request.

Redacted for Privacy

Brian A. Logue, Author

ACKNOWLEDGEMENTS

CONTRIBUTION OF AUTHORS

TABLE OF CONTENTS

LIST OF FIGURES

LIST OF TABLES

THE ROLE OF IRON-OXIDES IN U(VI) ADSORPTION AND THE KINETICS OF CONTAMINANT ORGANIC REDUCTION

Chapter 1: Introduction

Contaminant transport in ground water is an important process that affects a host of natural environmental systems. Transport of contaminants is affected by many processes, including aqueous complexation, adsorption, and redox reactions. One of the most important components of aquifers that controls the transport of contaminants is iron-oxides. In this study, the effects of iron-oxides on an inorganic radionuclide and representative organic contaminants were studied. Specifically, the role of iron-oxides in the adsorption of U(VI) on natural iron-rich sands, and the reduction of carbon tetrachloride (CT) and nitrobenzene (NB) by oxide coated gold electrodes was investigated.

Iron-oxides are ubiquitous in soils and sediments. Precipitation, dissolution, and reprecipitation of these oxides continually occur in a water borne system, which lends to iron-oxides appearing as coatings on sediments and soils. Iron-oxides also have a large surface area as compared with other components of soils, which leads to much of the surface area of soils being attributable to iron-oxides. Both of these factors allow iron-oxides to control adsorption properties of soils even if they are minor components. Therefore, an understanding of the interaction of a contaminant with iron-oxides is an important component of a subsurface transport model.

In this thesis, two processes affecting the transport of contaminants in the subsurface environment will be focused on: adsorption and reduction. The role of iron-oxides in each of these processes will be investigated. The research reported in this thesis

is separated into three manuscript chapters. A general introduction is written for each chapter, below.

Modeling Adsorption of U(VI) to Heterogeneous Iron-Rich Sorbents (Chapter 2)

Because of their hazardous potential, transport of radioactive heavy metals through the subsurface environment is an especially important process. These metals must be isolated from the biosphere, yet inadequate disposal efforts have lead to the leaching of radionuclides away from disposal sites (Olsen et al., 1986). Because iron-oxides are strong adsorbents of heavy metals, they are one of the most important factors controlling the transport of heavy metals in ground water. In this study (Chapter 2), the effect of iron-oxides on the adsorption of U(VI) to heterogeneous environmental sands is investigated.

Uranium can exist in a host of oxidation states. The most stable oxidation state in aerated aqueous solutions is U(VI) (Langmuir, 1978). U(IV) is another common oxidation state, but it is effectively insoluble under most environmental conditions. Therefore, transport of uranium occurs mainly in the VI oxidation state. U(VI) exists in many forms in aqueous solution as seen in Figure 1.1. UO_2^{2+} is the predominant species at low pH values. As the aqueous pH increases, a host of hydrolysis products are formed from U(VI) and surrounding water molecules. If carbonate is present, species involving carbonate will predominate at high pH values. The complicated aqueous chemistry of U(VI) may translate into complicated adsorption phenomena.
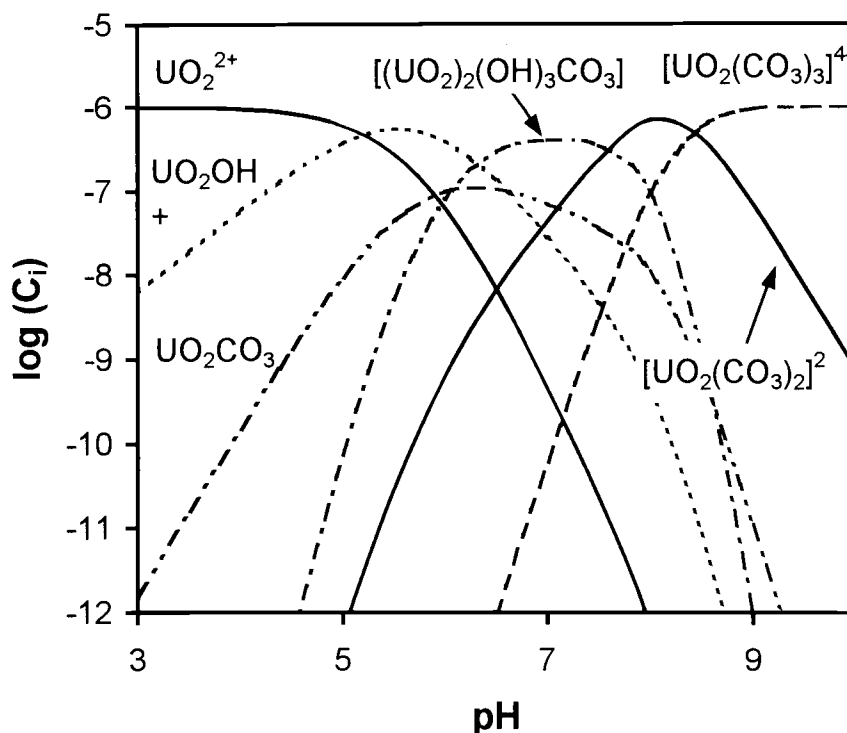
Figure 1.1. Aqueous speciation of U(VI) as a function of pH. $[CO_2^{2-}] = 10^{-3.5}$ atm, $[U(VI)] = 1$ μM, and 0.01 M Na^+. Calculated using reaction constants from Grenthe et al. (1992).

Adsorption of U(VI) on iron minerals is of great importance because of the affinity of U(VI) for iron-oxides and the widespread occurrence of these oxides in the subsurface environment. U(VI) adsorption on iron minerals has been studied by many workers (Hsi and Langmuir, 1985; Payne et al., 1994; Waite et al., 1994; Redden et al., 1998). Most attempts to characterize adsorption of UO_2^{2+} have involved synthetic minerals in laboratory environments. These studies on synthetic or pure minerals offer insight about adsorption of UO_2^{2+} onto an iron-rich surface, but applicability of laboratory based models for real, heterogeneous environmental sorbents remains open to question.

One commonly used approach for describing adsorption of a chemical species on a mineral sorbent is a surface complexation model (SCM) (Davis and Kent, 1990). The initial implementation of SCMs used a single site with an electrostatic component to describe adsorption. Severe limitations for this type of model became apparent when applied to multi-component systems or data gathered over a wide range of conditions. The SCM idea was expanded by using more than one site to describe adsorption by a mineral sorbent. With this approach, adsorption is described as a superposition of Langmuir type adsorption sites. Equation 1.1 describes the summation of Langmuir isotherms to determine the overall isotherm.

$$C_s = \sum_{i=1}^{n} \frac{K_i C_w T_i}{1 + K_i C_w} \qquad (1.1)$$

where C_s is the adsorbed concentration, C_w is the aqueous concentration of the analyte, T_i is the site concentration of surface sites of type i, K_i is the reaction constant of the adsorption reaction between the analyte and surface sites of type i, and n is the total number of surface site types involved in adsorption of an analyte. Figure 1.2 represents the summation of three Langmuir isotherms to model a typical environmental isotherm.

The mathematical models described above can be incorporated into transport code and used to help describe the transport of U(VI) through iron-rich materials. Determination of the abundance and affinity of iron sites that adsorb U(VI) (T_i and K_i in Equation 1.1) is an important component of these comprehensive transport models.
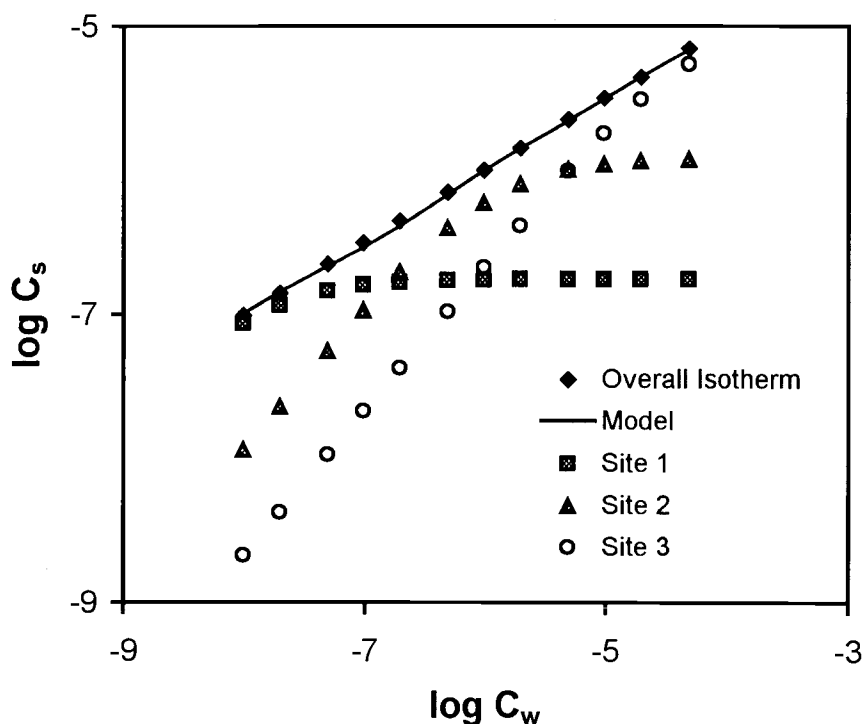
Figure 1.2. Representation of a Freundlich isotherm (n = 0.5, log K_F = -3) by multiple Langmuir isotherms.

Generally, parameterizing a mathematical model which describes adsorption of metals to heterogeneous environmental sorbents has been approached in two ways (Westall et al., 1998). In the *classical* approach, adsorption isotherms of heterogeneous environmental sorbents are hypothesized to be some linear combination of isotherms of the components that make up the heterogeneous material (Cowan et al., 1992; Waite et al., 1992). Equation 1.2 mathematically describes the classical approach to modeling adsorption.

A separate model must be developed for all the components that influence adsorption and weights (w_1, w_2, w_3, and w_4 in Equation 1.2) for each of these models must be assigned to each of the components to determine the overall adsorption:

$$C_s = w_1 C_{s,\text{iron-oxide}} + w_2 C_{s,\text{aluminum-oxide}} + w_3 C_{s,\text{organic}} + w_4 C_{s,\text{clay}} + \cdots \quad (1.2)$$

where C_s is the concentration of analyte sorbed to each of the individual components of the heterogeneous environmental sorbent. Adsorption of metals on pristine reference materials, such as laboratory synthesized oxides, is studied in a laboratory environment. The individual isotherms of reference materials are weighted to form a model which may predict adsorption data gathered on the heterogeneous sorbent of interest.

In a second approach, the *affinity spectrum* approach, heterogeneous environmental sorbents of interest are themselves used in adsorption experiments. A semi-empirical model based on some distribution of complex properties is used to represent the data because of the complexity of the environmental sorbent. When using this approach, one generally fixes the surface reaction constants (K_i in Equation 1.1) and adjusts the individual site concentrations (T_i in Equation 1.1) to best describe adsorption data gathered on the heterogeneous environmental sorbent of interest. The affinity spectrum approach for modeling adsorption data systematically simplifies models and usually allows for better interpolation of adsorption data than the classical approach because the sorption data are modeled directly.

The Effect of Citrate on U(VI) Adsorption (Chapter 3)

The presence of chelators can drastically affect the adsorption and transport behavior of heavy metals. Several studies have found enhanced migration of heavy metal contaminants away from disposal facilities in the presence of complexing agents (Means et al., 1978; Olsen et al., 1986; Price and Ames, 1976; Killey et al., 1984). A number of laboratory studies have also produced similar results (Elliott and Denneny, 1982;

Azizian, 1998). By contrast, enhanced adsorption has also been observed (Redden et al., 1998; Zachara et al., 1995; Girvin et al., 1993). Because of the large contrast in the adsorption behavior of heavy metals in the presence of chelators, the effect of a specific organic complexing agent and a heavy metal must be know to effectively model transport of a heavy metal in the presence of chelators. In this chapter, the effect of citrate on the adsorption of U(VI) to a heterogeneous sand was investigated.

Shown in Figure 1.3 are several reactions that can affect the adsorption properties of a heavy metal (M) in the presence of an organic complexing agent (L). These reactions include, but are not limited to, strong solution complexes between a complexing agent and a heavy metal (I), redox phenomena (II), ternary complexes between the surface and a metal-ligand complex (III), and surface alteration of a sorbent (IV).
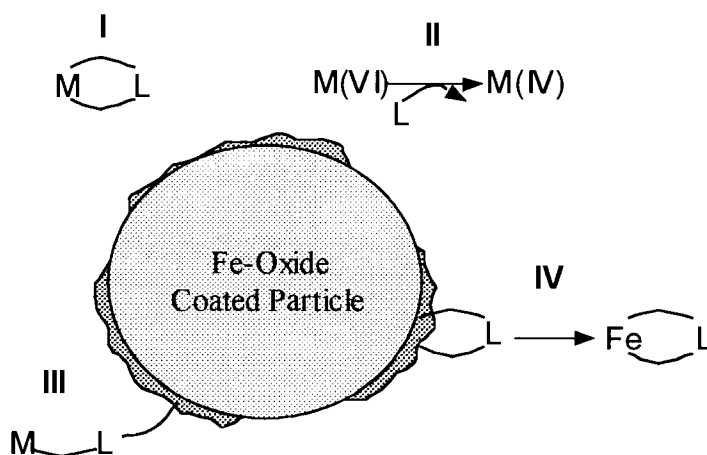
Figure 1.3. Schematic representation of some possible reaction mechanisms for altering the adsorption behavior of a metal. I) strong aqueous complex, II) redox reaction with a complexing agent as mediator or electron donor, III) ternary surface complex, IV) surface alteration.

Citrate was chosen as a model organic complexing agent. As with other complexing agents, citrate can complicate U(VI) adsorption phenomena by increasing, decreasing, or not appreciably influencing adsorption depending on the sorbent of interest, the concentration of citrate, and the aqueous pH (Redden et al., 1998).

One little-studied mechanism that could change the adsorption properties of U(VI) is surface alteration (Figure 1.3, IV). Citrate has been found to effectively extract amorphous Fe when used with ascorbate (Reyes and Torrent, 1997), and ligand promoted dissolution has been found to alter oxide surfaces by many workers (Kraemer et al., 1998; Holmen and Casey, 1996; Klewicki and Morgan, 1999). Therefore, citrate could alter the surface of a sorbent both *physically* (e.g., loss of surface area) and *chemically* (e.g., change in the chemical composition of adsorbing oxide phases). Alteration of the heterogeneous environmental sorbent surface was found to be the main process controlling the adsorption behavior of U(VI) in the presence of citrate.

Influence of Iron-Oxide on Reduction by Zero-Valent Metals (Chapter 4)

The degradation of organic contaminants *in-situ* (in ground) is an important remediation technique that can be used to destroy hazardous contaminants without the expense of physically removing them from the subsurface environment. One promising technology that can be used to achieve *in-situ* degradation of organic contaminants is a permeable reactive barrier (PRB). Because of the abundance and low cost of zero-valent iron, it has been used extensively as a medium for PRBs (Tratnyek, 1996). One important factor affecting the performance of zero-valent iron PRBs is the presence iron-oxide. In this study, the role of iron-oxide on the reduction rate of two model organic contaminants (CT and NB) was investigated.

Figure 1.4 illustrates one common mode for using zero-valent iron PRBs in the subsurface environment. Ideally, a contaminant (CCl_4) is transported from a point source (a contaminant well in Figure 1.4) through the subsurface by groundwater flow. The contaminant is transported through the zero-valent iron PRB and is reduced within the PRB to non-hazardous chemicals (CH_4 and Cl^- in Figure 1.4).

Contaminant Plume

Fe(0) PRB

Contaminant Well

$CCl_4 + 4H^+ + 8e^- \longrightarrow CH_4 + 4Cl^-$

Ground Water Flow
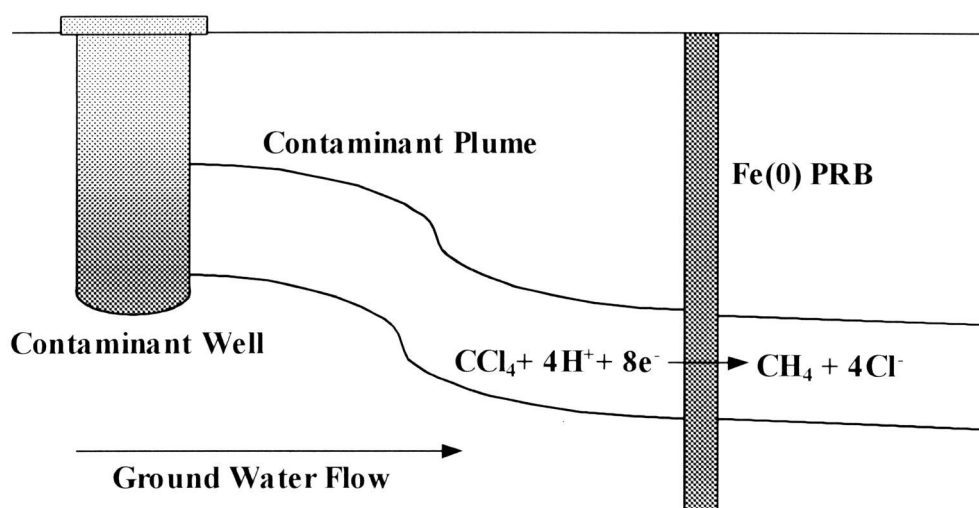
Figure 1.4. The reduction of CCl_4 by a zero-valent iron PRB.

The use of zero-valent iron as a medium for PRBs has produced encouraging results. Laboratory and field studies have been conducted to help understand the chemistry of the PRB system (Tratnyek, 1996), with the rate of contaminant degradation in these systems garnering the most focus (Johnson et al., 1996; Agrawal and Tratnyek, 1996; Sayles et al., 1997). Understanding what controls the rate of contaminant reduction is of considerable importance, because it has direct bearing on the choice of the medium and on the design of PRBs. Most investigators attempting to quantify the kinetics of contaminant degradation by zero-valent iron have used bulk techniques, such as column

or batch reaction systems, with no control over the formation of oxides (Sayles et al.,

1997; Johnson and Tratnyek, 1994; Agrawal and Tratnyek, 1996).

Because batch and column studies afford little control over some important

variables, a number of issues still limit progress toward a comprehensive understanding

of the factors affecting the degradation rate of contaminants in iron-bearing systems.

There is uncertainty as to how the growth of an oxide film affects the rate of degradation

of contaminants. Also, the relationship between the Fe(II) content of an oxide and the rate

of contaminant reduction is not well understood, even though work has been established

in this area (Stratmann and Müller, 1994; Klausen et al., 1995). There is also uncertainty

as to what fundamental factor is more important in the reduction of contaminant organics

at an iron-oxide surface: the transport of the contaminant to the site of the reaction or the

chemical reaction itself. Even more specifically, if the transport of a contaminant to a

reaction site is important, is transport through the pores of an oxide more important than

transport to the surface of an oxide. All of these issues are of great importance in

identifying promising enhancements to full-scale PRB remediation techniques.

The issues outlined above can be addressed by reducing the fairly complex system

of zero-valent iron, covered by an iron-oxide to two fairly simple systems: 1) a bare zero-

valent iron electrode with no oxide coating and 2) a noble metal electrode with an iron-

oxide film (Figure 1.5). Scherer et al. (1997) studied reduction of CT on a bare iron

electrode, concluding that the reaction was limited by electron transfer from the zero-

valent iron to the CT. We have focused on depositing iron-oxide films on a gold electrode

and studying the kinetics of organic contaminant reduction.
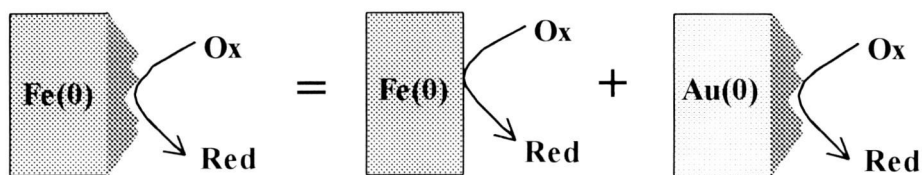
Figure 1.5. Reduction of the Fe(0)-contaminant-oxide system into two simpler systems: 1) oxide-free Fe(0) electrode and 2) noble metal electrode with iron-oxide film.

One issue that cannot be addressed by reducing the system to simpler components is the role of mass transport to the surface of the oxide. But, this can be addressed by creating a well-defined flow-through system that controls mass transport of organic contaminants in the aqueous phase. Control of mass transport allows for determination of its effects on reduction of organic contaminants. A system approximating a wall-jet configuration was used to accomplish this task.

Figure 1.6 shows the flow dynamics of the wall-jet electrode. A stagnant film model is used to describe the effect of mass transport on reduction rates. As the flow rate increases the thickness of the stagnant film (diffusion layer) is decreased. Therefore, controlling the flow rate allows for systematic control over the portion of the current that is limited by mass transport to the surface of the oxide.
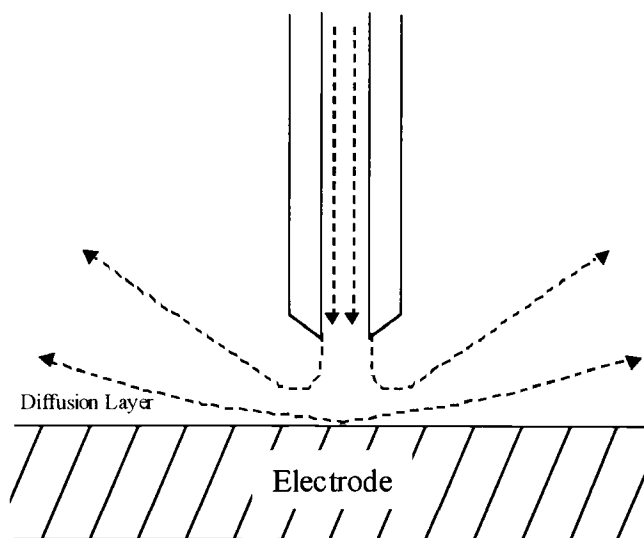
Figure 1.6. Schematic representation of flow in a wall jet electrode cell.

The combination of an Fe(III)-oxide coated gold electrode and a wall-jet electrode was used to address a number of issues outlined above. The fundamental mechanism of reduction and the factors affecting the overall reduction rate were investigated by varying the Fe(II) content in the iron-oxide (electrochemically), controlling the mass transport of chemicals to the oxide surface, and varying the thickness of the oxide film. In this study, transport of model contaminants (CT and NB) through the iron-oxide film was found to control the rate of reduction.

References

Agrawal A. and Tratnyek P. G. (1996) Reduction of Nitro Aromatic Compounds by Zero-Valent Iron Metal. *Environ. Sci. Technol.* **30**, 153-160.

Azizian M. F. and Nelson P. O. (1998) Lead Sorption, Chemically Enhanced Desorption, and Equilibrium Modeling in an Iron-Oxide-Coated Sand and Synthetic Groundwater System. In *Adsorption of Metals by Geomedia* (ed. E.A. Jenne), Chap. 6, pp. 165-180. Academic Press.

Cowan C. E., Zachara J. M., Smith S. C., and Resch C. T. (1992) Individual Sorbent Contributions to Cadmium Sorption on Ultisols of Mixed Mineralogy. *Soil Sci. Soc. Amer. J.* **56**, 1084-1094.

Davis J. A. and Kent D. B. (1990) Surface complexation modeling in aqueous geochemistry. In *Mineral-Water Interface Geochemistry* (ed. M.F. Hochella and A.F. White); *Rev. Mineral.* **23**, pp. 177-260. Mineralogical Society of America.

Elliott H. A. and Denney C. M. (1982) Surface Ionization and Complexation at the Oxide/Water Interface. 3. Adsorption of Anions. *J. Colloid Interface Sci.* **74**, 32-43.

Girvin D. C., Gassman P. L., and Bolton H. (1993) Adsorption of Aqueous Cobalt Ethylenediaminetetraacetate by δ–Al_2O_3. *Soil Sci. Soc. Am. J.* **57**, 47-57.

Grenthe I., Fuger J., Lemire R. J., Muller A. B., Nguyen-Trung C., and Wanner H. (1992) *Chemical Thermodynamics of Uranium.* Elsevier.

Holmen B. A. and Casey W. H. (1996) Hydroxamate Ligands, Surface Chemistry, and the Mechanism of Ligand-Promoted Dissolution of Goethite [α-FeOOH(s)]. *Geochim. Cosmochim. Acta* **60**, 4403-4416.

Hsi C. D. and Langmuir D. (1985) Adsorption of Uranyl onto Ferric Oxyhydroxides: Application of the surface complexation site-binding model. *Geochim. Cosmochim. Acta* **49**, 1931-1941.

Johnson T. L., Scherer M. M., and Tratnyek P. G. (1996) Kinetics of Halogenated Organic Compound Degradation by Iron Metal. *Environ. Sci. Technol.* **30**, 2634-2640.

Killey R.W., McHugh J. O., Champ D. R., Cooper E. L., and Young J. L. (1984) Subsurface Cobalt-60 Migration from a Low-level Waste Disposal Site. *Environ. Sci. Technol.* **18**, 148-157.

Klausen J., Tröber S. P., Haderlein S. B., and Schwarzenbach R. P. (1995) Reduction of Substituted Nitrobenzenes by Fe(II) in Aqueous Mineral Suspensions. *Environ. Sci. Technol.* **29**, 2396-2404.

Klewiki J. K. and Morgan J. J. (1999) Dissolution of β-MnOOH particles by ligands: Pyrophosphate, Ethylenediaminetetraacetate, and Citrate. *Geochim. Cosmochim. Acta* **63**, 3017-3024.

Kraemer S. M., Chiu V. Q., and Hering J. G. (1998) Influence of pH and Competitive Adsorption on the Kinetics of Ligand-Promoted Dissolution of Aluminum Oxide. *Environ. Sci. Technol.* **32**, 2876-2822.

Langmuir D. (1978) Uranium solution-mineral equilibria at low temperatures, with applications to sedimentary ore deposits. *Geochim. Cosmochim. Acta* **42**, 547-569.

Means J. L., Crerar D. A., and Duguid J. O. (1978) Migration of radionuclide wastes: Radionuclide Mobilization by Complexing Agents. *Science (Washington, DC)* **200**, 1477-1486.

Olsen C. R., Lowry P. D., Lee S. Y., Larsen I. L., and Cutshall N. H. (1986) Geochemical and Environmental Processes Affecting Radionuclide Migration from a Formerly Used Seepage Trench. *Geochim. Cosmochim. Acta* **50**, 593-607.

Payne T. E., Davis J. A. and Waite T. D. (1994) Uranium Retention by Weathered Schists: The role of Iron Minerals. *Radiochim. Acta* **66/67**, 297-303.

Price S. M. and Ames L. L. (1976) Transuranium Nuclides in the Environment. Publication SM-199/87, Int. Atomic Energy Agency.

Redden G., Li J., and Leckie J. (1998) Adsorption of Uranium (VI) and citric acid on Goethite, Gibbsite, and Kaolinite: Comparing Results for Binary and Ternary Systems. In *Adsorption of Metals by Geomedia* (ed. E.A. Jenne), Chap. 13, pp. 291-315. Academic Press.

Reyes I. and Torrent J. (1997) Citrate-Ascorbate as a Highly Selective Extractant for Poorly Crystalline Iron Oxides. *Soil Sci. Soc. Am. J.* **61**, 1647-1654.

Sayles G. D., You G., Wang M., and Kupferle M. J. (1997) DDT, DDD, and DDE Dechlorination by Zero-Valent Iron. *Environ. Sci. Technol.* **31**, 3448-3454.

Scherer M. M., Westall J. C., Ziomek-Moroz M., and Tratnyek P. G. (1997) Kinetics of Carbon Tetrachloride Reduction at an Oxide-Free Iron Electrode. *Environ. Sci. Technol.* **31**, 2385-2391.

Stratmann M. and Müller J. (1994) The Mechanism of the Oxygen Reduction on Rust-covered Metal Substrates. *Corr. Sci.* **36**, 327-359.

Tratnyek P. G. (1996) Putting Corrosion to Use: Remediating Contaminated Groundwater with Zero-Valent Metals. *Chem. Ind. (London)*, 499-503.

Waite T. D., Payne T. E., Davis J. A., and Sekine K. (1992) *Uranium Sorption: Alligator Rivers Analogue Proj., Final Rept., 13.* Australian Nuclear Science and Technology Organization.

Waite T. D., Davis J. A., Payne T. E., Waychunas G. A., and Xu N. (1994) Uranium (VI) adsorption to Ferrihydrite: Application of a surface complexation model. *Geochim. Cosmochim. Acta* **58**, 5465-5478.

Westall J. C., Černík M., and Borkovec M. (1998) Modeling Metal Speciation in Aquatic Systems. In *Metals in Surface Waters* (ed. H.E. Allen et. al), Chap. 10, pp. 191-216. Ann Arbor Press.

Zachara J. M., Gassman P. L., Smith S. C., and Tayler, D. (1995) Oxidation and adsorption of Co(II)EDTA^{2-} complexes in subsurface materials with iron and manganese oxide grain coatings. *Geochim. Cosmochim. Acta* **59**, 4449-4463.

Chapter 2: U(VI) Adsorption on Natural Iron-Coated Sands: Comparison of Surface Complexation Approaches to Modeling Adsorption on Heterogeneous Environmental Materials

Brian A. Logue[1], Robert W. Smith[2], and John C. Westall[1]*

[1]Department of Chemistry
Oregon State University
Corvallis, OR 97331

[2]Idaho National Engineering and Environmental Laboratory
Idaho Falls, ID 83415

*Corresponding Author, Email: westallj@chem.orst.edu

Abstract

Adsorption of U(VI) on natural iron-rich sands from Oyster, VA was studied over a range of U(VI) concentrations (0.1-100 µM), pH values (3-7.6), and dithionite-citrate-bicarbonate (DCB) extractable Fe (3.1-12.3 µmol/g). Four modeling approaches were applied to adsorption data gathered on six iron-coated sands. The ability of each model to interpolate the U(VI) adsorption data was evaluated. A two-site, laboratory-based, diffuse double layer, surface complexation model (SCM) was applied to the data (Model I). Model I was originally calibrated for synthetic ferrihydrite by Waite et al. (1994), yet Model I was surprisingly accurate considering the magnitude of approximations necessary for application of the laboratory based model natural sands. The surface and solution reactions used for Model I, along with the treatment of the electric double layer (EDL), were used in Model II. Model II was calibrated to a portion of U(VI) adsorption data for each sand, and then used to predict adsorption data for the same sand under different experimental conditions. Model II did not increase the accuracy of the predictions made with Model I. Two, four-site affinity spectrum SCMs, Models III and IV, were used to improve interpolation of the adsorption data with respect to Models I and II. Model III was based on a discrete log K spectrum approach, and Model IV was attained from adjusting all surface stability constants and site concentrations for all surface sites. Both affinity spectrum SCMs did not explicitly consider the EDL or surface hydrolysis reactions. Models III and IV interpolated the U(VI) adsorption data with great accuracy.

Model I provides evidence supporting the practice of using pure phase thermodynamic reaction constants for describing the adsorption characteristics of

environmentally important sorbents in certain simple cases. Yet, affinity spectrum

approaches (Models III and IV) become increasingly important as more accurate

interpolation of adsorption data is necessary, the sorbent becomes increasingly complex,

or the range of experimental conditions expands.

Introduction

Adsorption of uranyl ion (U(VI) or UO_2^{2+}) on iron minerals has been studied by

many workers (Hsi and Langmuir, 1985; Payne et al., 1994; Waite et al., 1994; Redden et

al., 1998). Most attempts to characterize adsorption of UO_2^{2+} have involved synthetic

minerals in laboratory environments. These studies on synthetic or pure minerals offer

insight about adsorption of UO_2^{2+} onto an iron-rich surface, but applicability of

laboratory based models for real, heterogeneous environmental sorbents remains open to

question.

Modeling adsorption of U(VI) on iron-rich surfaces is important for the

development of comprehensive transport codes that predict the fate of U(VI) in the

subsurface environment. Spatial variation of iron throughout the subsurface environment

can be included in a transport model. Therefore, the adsorption behavior of U(VI) on the

iron minerals of interest must be established to adequately model retention of U(VI) by

iron-rich subsurface minerals.

One commonly used approach for describing adsorption of a chemical species on

a mineral sorbent is a surface complexation model (SCM) (Davis and Kent, 1990). A

SCM is a mathematical model used to describe adsorption by a mineral sorbent as a

superposition of Langmuir type adsorption sites. The concentration and affinity of these

sites calculated for a specific SCM can be mathematically projected onto a mineral

surface to incorporate specific adsorption characteristics of the mineral sorbent in a transport model. Therefore, when describing the transport of U(VI) through iron-rich materials, the determination of the abundance and affinity of iron sites that adsorb U(VI) is an important component of a comprehensive transport model.

Generally, modeling adsorption of metals to heterogeneous environmental sorbents by SCMs has been approached in two ways (Westall et al., 1998). In the first approach, which will be termed the *classical* approach, adsorption isotherms of heterogeneous environmental sorbents are hypothesized to be some linear combination of isotherms of the components that make up the heterogeneous material (Cowan et al., 1992; Waite et al., 1992). Adsorption of metals on pristine reference materials, such as laboratory synthesized oxides, is then studied to determine adsorption behavior of the reference material in a laboratory environment. The individual isotherms of reference materials are weighted to form a model which may predict adsorption data gathered on the heterogeneous sorbent of interest. When this approach is used, adsorption on heterogeneous environmental material is not studied directly, except to verify model predictions. The classical approach is advantageous to control laboratory conditions, obtain detailed structural information of molecular interactions, and gather orderly data. There are also major difficulties in using reference materials to describe heterogeneous materials. First, natural heterogeneous materials are not easily approximated by laboratory synthesized minerals (Waite et al., 1992) and adequate reduction of a heterogeneous environmental sorbent into individual components may not be possible (e.g., humic acids). Also, relating constants used for a reference material to easily measurable characteristics of heterogeneous environmental sorbents is difficult. In

particular, concentrations of complexing surface sites may be difficult to estimate from measurable characteristics of the natural materials. Difficulties involved in the application of classical SCMs to data gathered on natural materials from the field have limited their use (Loux et al., 1989; Mueller and Sigg, 1990; Smith, 1991). Also, the classical approach to modeling is very time consuming and requires gathering large amounts of experimental data.

In a second approach, which will be termed the *affinity spectrum* approach, heterogeneous environmental sorbents of interest are themselves used in adsorption experiments. A semi-empirical model based on some distribution of complex properties is used to represent the data because the complexity of the environmental sorbent precludes detailed molecular-level structural information (Westall et al., 1995). Previous studies have used a discrete log K spectrum (DLKS) approach with no electric double layer (EDL) correction to describe adsorption to heterogeneous environmental materials (Černík et al., 1996). The affinity spectrum approach for modeling adsorption data systematically simplifies models and usually allows for better interpolation of adsorption data than the classical approach. The advantages of this approach are that the heterogeneous environmental sorbent is studied directly, so that no extrapolation from reference materials is necessary, and a relatively simple model can be used to describe adsorption. A disadvantage is that data gathered from experiments on heterogeneous materials may be difficult to interpret because of the inability to control natural phenomena during experiments, such as spatial pH variations and dissolution of the soluble materials from the sorbent. In this study, we attempt to evaluate both modeling approaches as applied to U(VI) adsorption on natural iron-coated sands.

A measure of the goodness of the fit known as the weighted sum of squares over the number of data points (χ^2/N) will be used to quantitate the accuracy of an individual model with specific error estimates (Herbelin and Westall, 1999).

Experimental

Materials and Characterization Methods

A primary U(VI) stock solution (10 mM UO_2^{2+}) was prepared from analytical grade uranyl nitrate solid ($^{238}UO_2(NO_3)_2 \cdot 6H_2O$) from Fluka (Ronkonkoma, NY) by diluting with 1% HNO_3. All secondary standards and aliquots to adsorption experiments were diluted from this primary stock solution.

Naturally coated hydrous metal oxide coated sands were collected from a sampling pit located on the southern tip of the Delmarva Peninsula in Virginia, near the village of Oyster. The borrow pit site that contains surface exposures of the lower portion of the Butlers Bluff Member of the Nassawadox Formation (Mixon, 1985). Exposed in the Oyster borrow pit are cross-stratified sands, horizontally-bedded sands, shelly gravelly sands (DeFlaun et al., 1997). The primary mineralogy consists of quartz with varying amounts of lithic fragments and shell (replaced by secondary hydrous iron oxide). In addition, minor amounts of feldspars and dark minerals (primarily hornblende and ilmenite) are present. Secondary minerals include extensive hydrous iron oxide (ranging from 2 to 100 mmol/g Fe) and very minor clay minerals (primarily kaolinite replacing feldspars with some smectites). The distribution of secondary hydrous iron oxide coatings are visibly striking and strongly correlated with sedentary depositional features including: 1) coarse poorly sorted lag deposits several cm thick, 2) thin (mm thick) erosion surfaces and tops of individual cross-beds, 3) replacing fossil surf clam

shells, and 4) cross-cutting primary sedimentary structures. Although at the time of deposition significant calcium carbonate (in the form of shell fragments) occurred in the sections, the calcium carbonate has been completely replace primarily by hydrous iron oxides.

Table 2.1. Characteristics of Oyster, VA sand samples.

Sample	Extractable Fe (μmol/g)[a]	Extractable Al (μmol/g)[a]	Surface Area (m^2/g)[b]	Cation Exchange Capacity (meq/g)[c]
BS-3	12.8	22.0	1.51	1.10
BS-4	3.1	7.2	0.50	0.74
BS-5	10.2	11.5	1.40	0.69
BS-6	4.8	6.8	0.44	0.32
BS-7	7.1	4.8	0.36	0.36
BS-8	4.1	3.7	0.25	0.26

[a] Sample extractable Fe and Al measured with dithionite-citrate-bicarbonate extraction (Jackson et al., 1986).
[b] Surface area determined by multi-point B.E.T. gas adsorption (Brunauer et al., 1938).
[c] Cation exchange capacity measured by sodium exchange (Hesse, 1971).

Total surface areas were determined by multi-point B.E.T. gas adsorption measurements (Brunauer et al., 1938) using a Gemini 2360 Rapid Surface Area Analyzer. Extractable iron and aluminum were determined by buffered dithionite-citrate-bicarbonate reductive extractions and acid ammonium oxalate in the dark extractions. Procedures for both of these methods are given by Jackson et al. (1986). Cation exchange capacity was determined by saturating the sediment exchange sites using 1.0 M sodium acetate and exchanging the sodium for ammonium with 1.0 M ammonium acetate followed by quantification of the exchanged sodium by ICP (Hesse, 1971). Table 2.1 presents the measured chemical and physical characteristics of the 6 Oyster borrow pit samples used for this study.

Adsorption Experiments

Experimental data were gathered in the form of pH adsorption edges (the portion of the pH range studied where adsorption of U(VI) increases from almost zero to 100%) at total UO_2^{2+} concentrations of 0.1, 1, 10, and 100 μM for two sand samples (BS-3 and BS-8). Adsorption experiments for the four remaining samples were performed at one total UO_2^{2+} concentration (1 μM). The pH range studied was 3.0 to 7.6.

Adsorption data were gathered from batch type experiments. A 20 g/L sand sample was added to a 50 mL polycarbonate centrifuge tube with 0.01 M $NaClO_4$ as the supporting electrolyte. Before addition of UO_2^{2+}, the sand slurry was shaken for 24 hours at 200 rpm and 25 °C to pre-equilibrate the sand with the aqueous phase. At the end of the 24 hour period, the UO_2^{2+} was added to the centrifuge tube along with NaOH and $HClO_4$ to adjust the pH to the desired value. The solution was shaken for 48 hours at 200 rpm and 25 °C to equilibrate the system (equilibration time determined by kinetics experiments, the results of which are not shown). The caps of the centrifuge tubes had 3 mm holes to promote equilibration with atmospheric CO_2. Adsorption equilibration time for CO_2 was determined independently to be less than the 48 hours necessary for UO_2^{2+} adsorption equilibrium. The samples were then centrifuged for 30 minutes at approximately 12000 rpm to separate the aqueous and the solid phases. Aliquots of the supernatant were transferred to sample tubes and diluted with 1% HNO_3 prior to determination of U(VI) by ICP-MS.

The supernatant was then transferred to a clean centrifuge tube leaving wet sand. The pH of the supernatant was measured and the wet sand was freeze dried to remove any residual water. The amount of water contained in the sand (and hence the amount of

aqueous U(VI) associated with the wet sand) was found by the difference of the masses of the original sample and the freeze dried sample. The dry sand was then transferred to a clean centrifuge tube. An aliquot of 1% HNO_3 was added to both the tube used for the adsorption experiment (to extract the UO_2^{2+} from the centrifuge tube) and the clean tube with the dried sand (to extract U(VI) adsorbed to the iron-rich sands). The tubes were shaken for 48 hours at 200 rpm and 25 °C to ensure complete extraction. Aliquots from both tubes were diluted for measurement by ICP-MS. UO_2^{2+} concentration was determined by mass for all adsorption experiments.

The total aqueous concentration of iron (dissolved or suspended in the aqueous phase during the adsorption experiment) in the supernatant after centrifugation was determined by the phenanthroline photometric method (Greenburg et al., 1992). It was determined that aqueous Fe colloids did not have a significant effect on the adsorption of U(VI) by the iron-rich sands studied.

Analysis of U(VI) by ICP-MS

The samples were analyzed for U(VI) with a Fisons VG PlasmaQuad II+ ICP-MS with a concentric nebulizer and a Gilson 221 auto-sampler for sample uptake. The mass scan was conducted in peak-jump mode with an acquisition time of 30 seconds per sample. Peak jumping (only the mass/charge ratios of interest are detected) was used for counting ions instead of mass scan (entire mass/charge range is detected) because only the ^{238}U peak and the internal standard peak were of interest. The internal standard used for all samples was 10 $\mu g/L$ Bi (Bailey et al., 1993). The internal standard was added directly to the samples before they were analyzed by ICP-MS. A practical detection limit

of approximately 1 nM was found for the sand/UO_2^{2+} system and a linear calibration

range of 1 nM to 100 nM was used for determination of U(VI) for all samples.

Goodness-of-Fit

The goodness-of-fit of a specific model is generally quantified by χ^2 (Cernik et

al., 1995). χ^2/N will be used as a numerical comparison of how well the different

modeling approaches describe the data, where N is the number of data points. Equations

4.1-4.3 define χ^2:

$$\chi^2 = \sum_{i=1}^{N} \left(\frac{q_i - q_{i,exp}}{s_i} \right)^2 \qquad (4.1)$$

where q_i is the adsorbed concentration of U(VI) (in mol/L) calculated for data point i by

the model, $q_{i,exp}$ is the adsorbed U(VI) found experimentally in mol/L, and s_i is the error

in data point i found from the propagation of errors in Equation 4.2 summed over the

components of interest with s_{Tj} calculated from Equation 4.3:

$$s_i^2 = \sum_j \left(\frac{\partial(q_i - q_{i,exp})}{\partial T_j} \right)^2 s_{T_j}^2 \qquad (4.2)$$

$$s_{T_j} = s_{T_j,abs} + s_{T_j,rel} T_j \qquad (4.3)$$

where T_j is the total analytical concentration of the component j. In this study, j is the

adsorbed and aqueous concentrations UO_2^{2+}. s_{Tj} is the total error in the concentration of

UO_2^{2+} measured, where $s_{Tj,abs}$, and $s_{Tj,rel}$ are the absolute error and the relative error

involved in the measurement of UO_2^{2+}, respectively. $s_{Tj,rel}$ was estimated to be 1%. $s_{Tj,abs}$

was estimated to be 1% of the total UO_2^{2+} added because the U(VI) was diluted to a

calibration range of 1-100 nM with an overall detection limit for the adsorption

experiment of 1 nM. All χ^2/N values were calculated with these error estimates. Because the total amount of U(VI) available for adsorption varies with each individual data point (described below), s_{Tj} for each individual data point was used to calculate χ^2/N (Herbelin and Westall, 1998).

The goodness-of-fit can also be expressed as the χ^2/DF, where the degrees of freedom (DF), in this study, is the difference between N and the number of adjustable parameters. Ideally, the value of χ^2/DF, which depends heavily on the experimental error estimates, should approach 1 for the model to be considered to be valid. In practice a value of 20-0.1 for this parameter indicates a good fit of the data, when realistic error estimates are used (Herbelin and Westall, 1996).

Minimization Algorithm

FITEQL4.0 was used to adjust parameters and calculate equilibrium conditions for Models I and II, but was not robust enough to handle the minimization problems presented by Models III and IV. Therefore, FITEQL was modified by insertion of a more robust nonlinear least squares minimization routine titled E04UPF, from the Numerical Algorithms Group (NAG Fortran Library, Mark 16, 1993). The details of the Models I-IV are discussed below.

Implementation of the NAG library routine was such that the first derivatives of the objective function could be calculated at every data point without changing calculation of the equilibrium speciation by FITEQL. The robustness and accuracy of the NAG minimization algorithm proved to be ample.

Results and Discussion

U(VI) Mass Balance

Two methods are commonly used for determining the amount of analyte adsorbed

on a sorbent of interest: the *direct method* in which the amount of analyte on the sorbent

is determined by direct analysis, and the *difference method* in which the amount of

analyte on the sorbent is determined as the difference between the amount that was added

initially and the amount found in the aqueous phase at equilibrium. If a significant

amount of analyte is lost to the container walls, the difference method can yield

significant errors. In most studies of U(VI) adsorption, the amount of UO_2^{2+} adsorbed to

the mineral sorbent has been found by difference (Hsi and Langmuir, 1985; Waite et al.,

1994; McKinley et al., 1995). This approach is simple and much less time consuming

than determining UO_2^{2+} concentration both on the sorbent and in the supernatant, but it

can produce erroneous results if some of the UO_2^{2+} added is taken up by some external

sink (e.g. container walls). Adsorption of UO_2^{2+} by the container was found to be

significant by Bertetti et al. (1995) during adsorption studies with quartz as the sorbent.

Therefore, these workers utilized the direct determination method for the quantification

of U(VI). Even though adsorption to the container occurred with quartz as the sorbent,

the adsorption of UO_2^{2+} to the container walls would presumably be decreased by a

sorbent with a much greater affinity for UO_2^{2+}, such as iron-rich minerals. If the sorbent

had a high enough affinity for U(VI), the direct determination and the difference methods

should result in effectively the same adsorbed U(VI) (within experimental error limits).

Also, Pabalan et al. (1994) found that adsorption of U(VI) to the container walls was

reduced by the use of polycarbonate vessels instead of polyethylene and, less

significantly, Teflon.

Figure 2.1 shows the distribution of 1 μM UO_2^{2+} among various components in a typical adsorption experiment: supernatant, sorbent, container, electrode for pH measurement, and transfer pipette tips. This figure illustrates that a substantial amount of UO_2^{2+} is adsorbed by the container in the presence of the iron-rich sands from Oyster, VA (especially at high pH values within the range studied). Over 50% of the 1 μM UO_2^{2+} was adsorbed by the centrifuge tube, and other external sinks at pH values of 5.43, 6.09, and 6.50. These results verify the need for a good experimental mass balance of strongly adsorbing metals before using the difference method. In this study, we utilized the direct determination method for quantifying UO_2^{2+}.
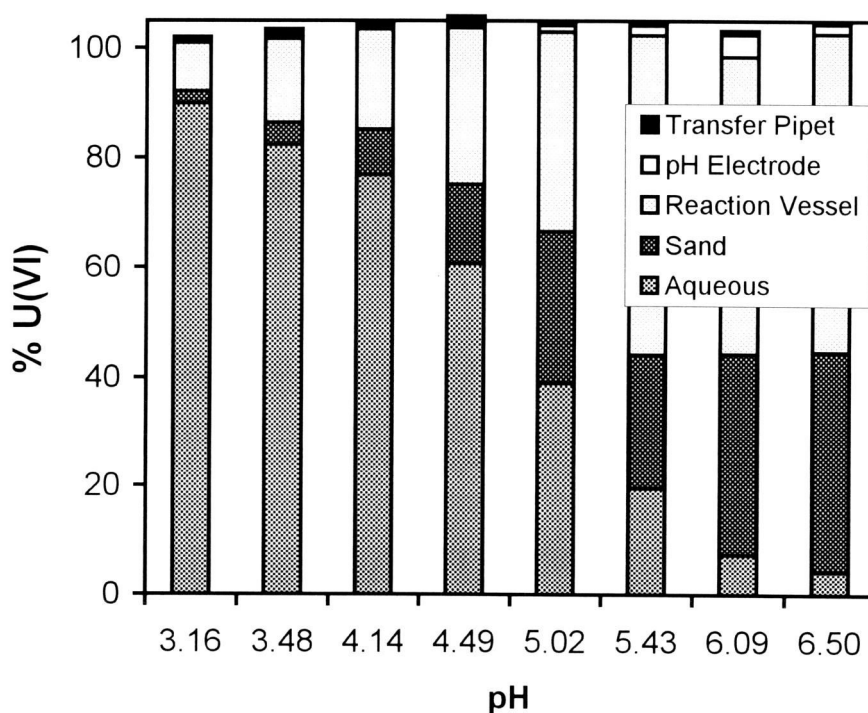
Figure 2.1. Mass balance of U(VI) in an adsorption experiment with natural sands. 20 g/L sand sample BS-4, 0.01 M $NaClO_4$, $p_{CO2} = 10^{-3.5}$ atm, and 1 μM U(VI).

The background U(VI) concentration measured by ICP-MS was always close to

1% of the total U(VI) added for the adsorption experiment (as described above).

Therefore, the total experimental error in the mass balance was estimated at 5% of the

total U(VI) added.

Experimental Adsorption Data

The adsorption data were obtained for six different sand samples from Oyster,

VA. A range of pH values from 3.0 to 7.6 were studied, at four total concentrations of

U(VI) (0.1, 1, 10, 100 µM), one ionic strength (0.01 M $NaClO_4$), and one solids

concentration (20 g/L). The samples were equilibrated with atmospheric CO_2. The

experimental data for two sand samples (BS-3 and BS-8) are shown in Fig. 2.2; data for

the other samples are presented in Fig. 2.3. The lines in Fig. 2.2 are drawn to guide the

eye and are not a model representation. Data presented in the form of Fig. 2.2 (pH

adsorption edges) often carry the implication that the total U(VI) is constant; however, in

this case, the total concentration of U(VI) available for adsorption changes with pH

(Fig. 2.1). Although isotherm data are included in Figs. 2.2 and 2.3 (total U(VI) available

for adsorption ranging from 48 nM to 100 µM), individual isotherms were not measured

because of the difficulty in ensuring a constant pH. Reference to the total concentration

of U(VI) in the figures, tables, or text should be interpreted as the total amount of U(VI)

added at the beginning of the adsorption experiment. Also, representation of Models I-IV

in the figures are at *one* total concentration of U(VI) (the total U(VI) added at the

beginning of the adsorption experiment), except for Fig. 2.4 where the true description of
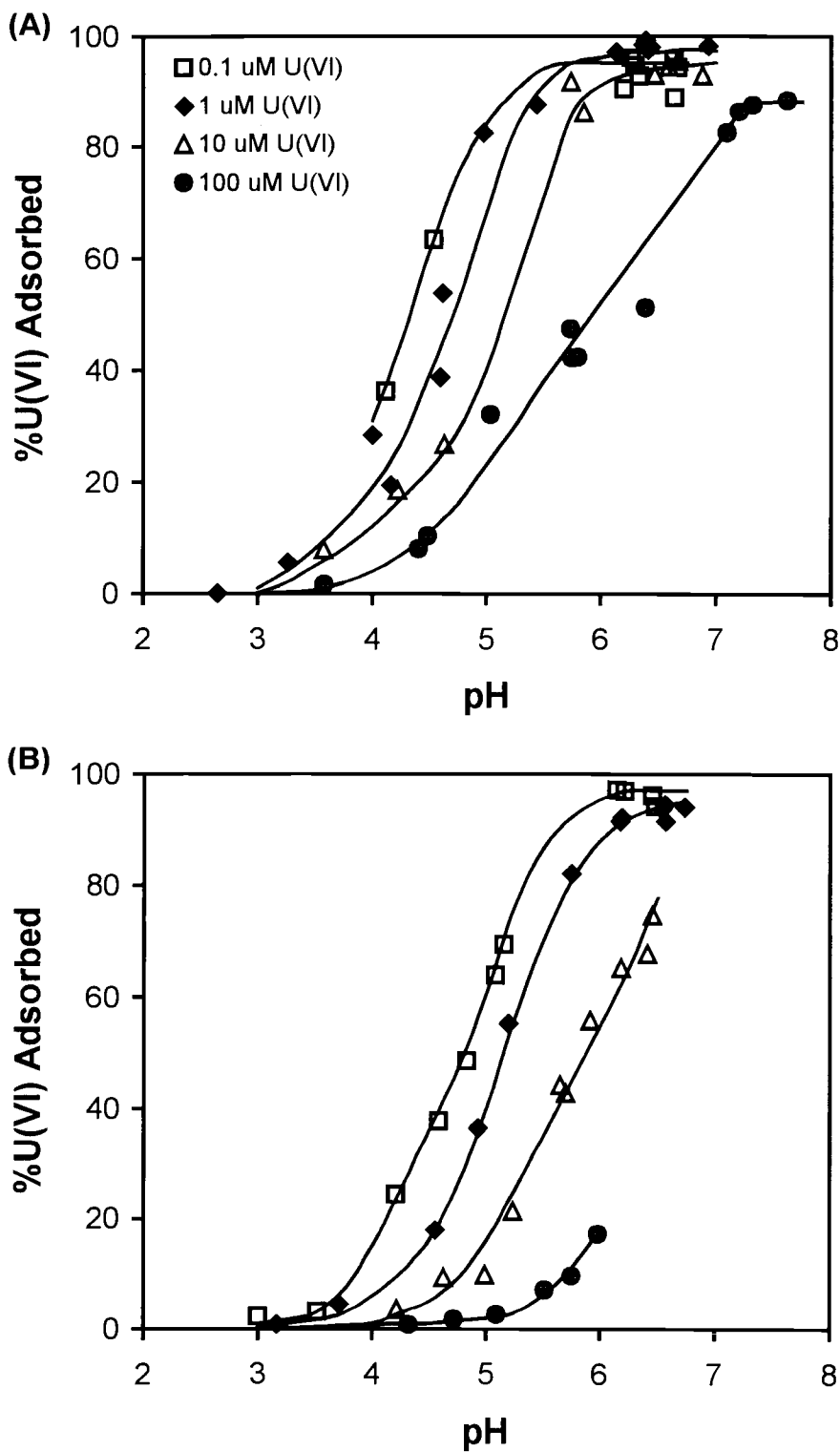
Figure 2.2. Adsorption data for four aqueous U(VI) concentrations and two sand samples. 20 g/L sand, 0.01 M $NaClO_4$, $p_{CO2} = 10^{-3.5}$ atm, and 0.1-100 μM U(VI). A) Sand sample BS-3. B) Sand sample BS-8.

(A)

(B)
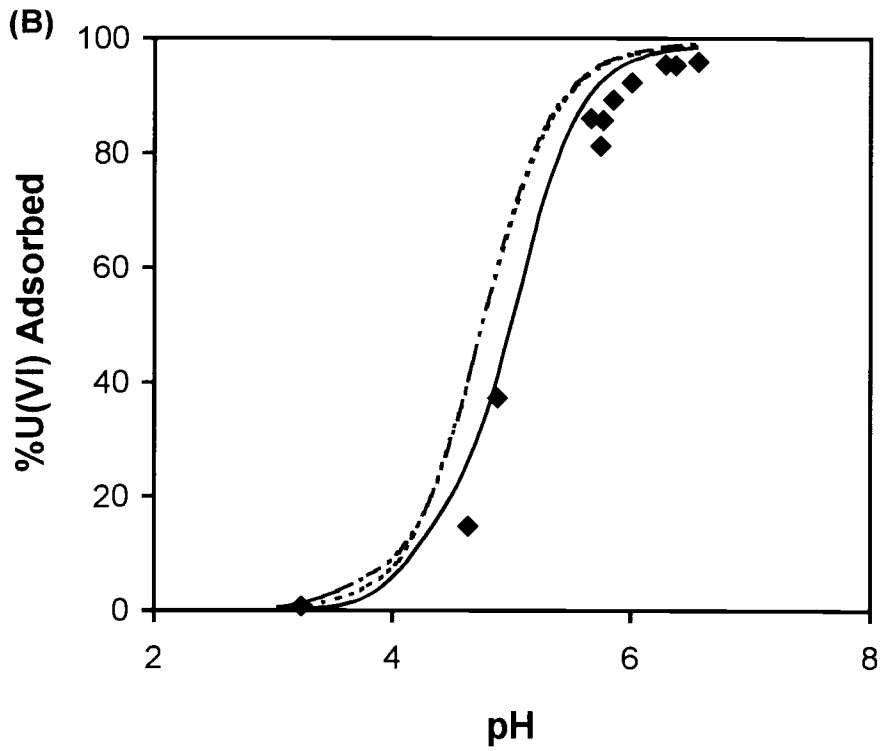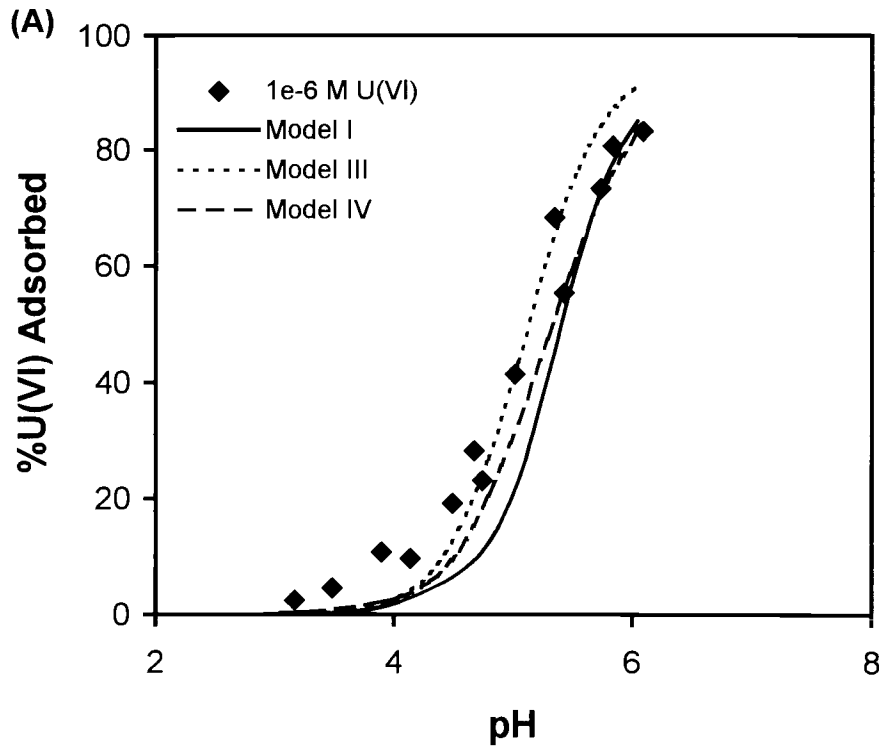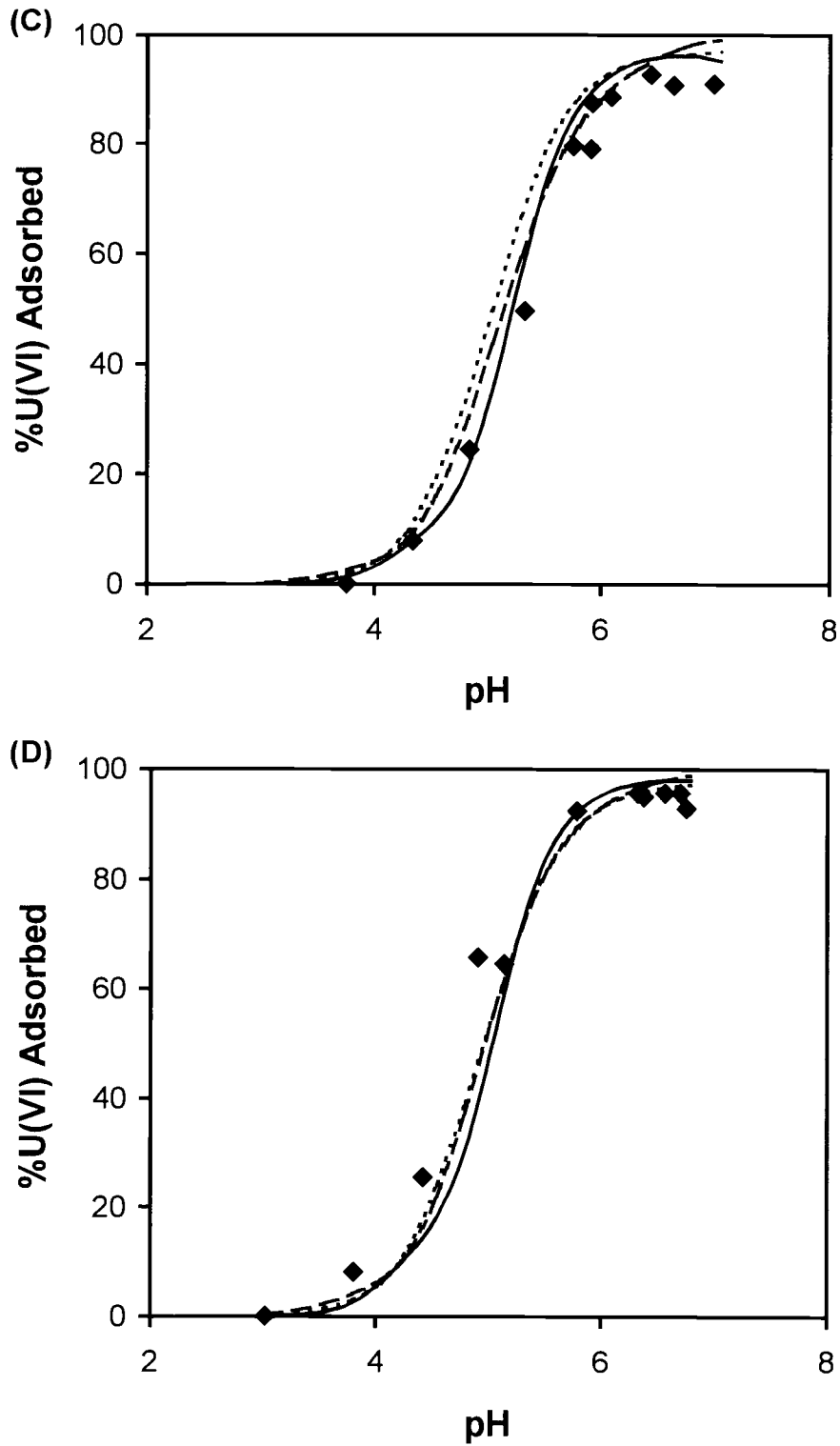
CONTINUED

Figure 2.3 (Continued). Predictions of pH adsorption edge data from natural sands at 1 μM U(VI). 20 g/L sand sample, 0.01 M NaClO₄, and $p_{CO_2} = 10^{-3.5}$ atm. A) Sand BS-4. B) Sand BS-5. C) Sand BS-6. D) Sand BS-7.

the adsorption data for Models I-IV is represented. Smooth line representations of the models at one total U(VI) concentration were found to adequately represent a specific model at variable total concentrations of U(VI).

The adsorption of U(VI) on the iron-rich sand samples has the same general characteristics as the adsorption data gathered by Waite et al. (1994) and others working with iron-rich minerals (Hsi and Langmuir, 1985; Payne et al., 1994; Redden et al., 1998). First, the pH adsorption edge occurs over one to two pH units and is relatively smooth (for sand BS-8). The slope of the pH adsorption edge may be influenced as much by the heterogeneity of the surface sites as by the proton stoichiometry of adsorption reactions. Yet, smooth adsorption data can be most easily modeled by assuming titration of one homogeneous site for each total concentration of U(VI), which generally produces a small number of homogeneous sites to describe adsorption. Second, as the aqueous U(VI) concentration increases the pH adsorption edge shifts to higher pH values. This shift indicates that the overall isotherms for U(VI) adsorption on the sands are nonlinear. Assuming Langmuir type sites are responsible for adsorption of U(VI), nonlinearity of the adsorption isotherms is due to saturation of one or more U(VI) adsorbing sites. Nonlinearity of overall adsorption isotherms is consistent with other studies of actinide adsorption on mineral surfaces (Davis and Kent, 1990; Waite et al., 1994; Kohler et al., 1996). Also, the shift in the pH adsorption edge with increasing U(VI) concentration is an indication that more than one adsorption site type may be involved in adsorption (Waite et al., 1992). Third, as shown by comparison of the pH adsorption edges at 100 μM U(VI) for sands BS-3 (Fig. 2.2a) and BS-8 (Fig. 2.2b), the fraction of U(VI) sorbed at a

Table 2.2. Summary of modeling approaches for Models I-IV with the calibration method, treatment of the electric double layer, adjustable parameters, and quantitative values for how well each model describes adsorption data.

	Calibration				Adjustable Parameters			χ^2/N[b]	
Model	Ferrihydrite	Sands	EDL	Sites[a]	T_i	$\log K_i$	Total	BS-3	BS-8
I	X		DLM	2			0	53.1	22.2
II	X[c]	X[c]	DLM	2	X[c]		1	42.4[d]	27.6[d]
III		X	Implicit	4	X	DLKS[e]	4	9.9	8.9
IV		X	Implicit	4	X	X	8	13.8	4.4

[a] The number of surface site types. The surface sites in all the models adsorb both UO_2^{2+} and UO_2CO_3.
[b] The values of χ^2/N were calculated using data from 0.1, 1, 10, and 100 μM U(VI) pH adsorption edges on natural sands.
[c] The total site concentration was only adjusted for the strong sites to best describe the 1 μM U(VI) adsorption data.
[d] The pH adsorption edge used to adjust the strong site concentration (1 μM UO_2^{2+}) is included in the χ^2/N value.
[e] The log K values were fixed according to a discrete log K spectrum.

Table 2.3. Types of data gathered for each individual sand and predictions or fits of the data for each model. E represents pH adsorption edge, I represents isotherm data, P is prediction by a specific model, and F is fitting of data by adjusting model parameters.

			Surface Complexation Model[c]			
Sand[a]	Data[b]	Figure	I	II	III	IV
BS-3	E/I	Not shown	P	F/P	F	F
BS-4	E	3a	P	F	P	P
BS-5	E	3b	P	F	P	P
BS-6	E	3c	P	F	P	P
BS-7	E	3d	P	F	P	P
BS-8	E/I	5 and 7[d]	P	F/P	F	F

[a] Sand samples from Oyster, VA. Characteristics presented in Table 2.1.
[b] Type of data available: pH adsorption edge data (E) or isotherm data (I).
[c] Data was fit (F) or predicted (P) with the designated model. The fit or prediction of the data is presented in the figure cited.
[d] Models I and II are shown in Figure 2.5. Models III and IV are shown in Figure 2.7.

given pH increased with sands that contain more DCB extractable Fe (Table 2.1). Payne et al. (1994) also found evidence supporting the importance of DCB extractable iron for adsorption of U(VI).

Overview of Models I-IV

Four modeling approaches were applied to U(VI) adsorption data gathered from six natural sand samples. Important characteristics of Models I-IV are reported in Table 2.2. Table 2.3 outlines the type of adsorption data available for a particular sand, the figure associated with the adsorption data, and whether the parameters within each model were adjusted to fit the adsorption data. The modeling approaches are described briefly below.

The first two models are classical models. Model I is a two-site SCM which explicitly models the charge characteristics of the electric double layer (EDL) with the diffuse layer model (DLM). This model was first reported by Waite et al. (1994) and was initially calibrated to model adsorption of U(VI) on ferrihydrite. In this study, Model I was used to predict natural sand adsorption data. Model I was applied directly to the natural sand data by approximating ferrihydrite iron with experimentally measurable DCB extractable Fe when determining the adsorption site concentration. Model II includes the same surface reactions, solution reactions, and treatment of the EDL as Model I. The strong site concentration of Model II was adjusted to minimize χ^2/N for adsorption data from the natural sands at 1 μM U(VI). Model II was then used to predict adsorption data for the same sand gathered under different concentrations of U(VI).

Two affinity spectrum models were also applied to the adsorption data. An affinity spectrum model was constructed from a two-dimensional DLKS (Model III). This model was based on an affinity spectrum of individual Langmuir type surface sites. Models III and IV were calibrated with the experimental adsorption data. Model III was calibrated by adjusting the concentrations of four U(VI) adsorbing sites with fixed reaction constants (4 adjustable parameters). Model IV was calibrated by adjusting all adsorption reaction constants along with the site concentrations for four U(VI) adsorbing sites (8 adjustable parameters).

Linear representations for each of the four models applied to the U(VI) adsorption data are presented in Fig. 2.4, with the solid line representing a perfect description of data for an individual model. For sand BS-3, Model I (Fig. 2.4a) suffers from a systematic underprediction of the fraction of U(VI) adsorbed and very poor predictions for some specific concentrations of total U(VI). Still, Model I predicted the adsorption data well, especially for sand BS-8, considering the approximations necessary to apply the model to the data. Model II (Fig. 2.4b) did not do a significantly better job at interpolating the data even though Model II was calibrated for each individual sand. Both affinity spectrum models (Model I-Fig. 2.4c and Model II-Fig. 2.4d) interpolated the data extremely well. Comparisons of each model are discussed below.
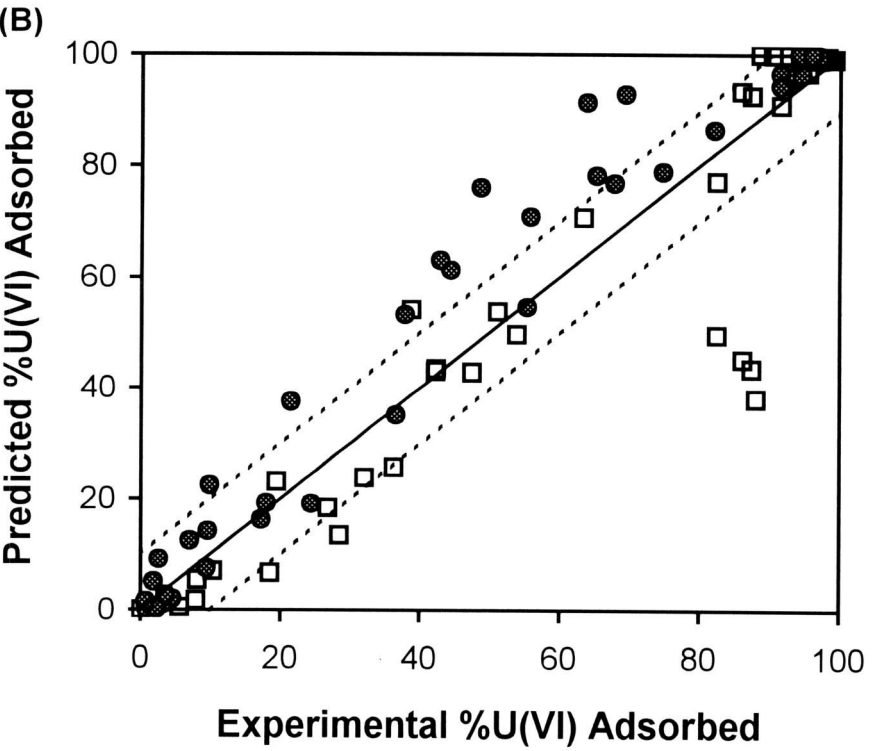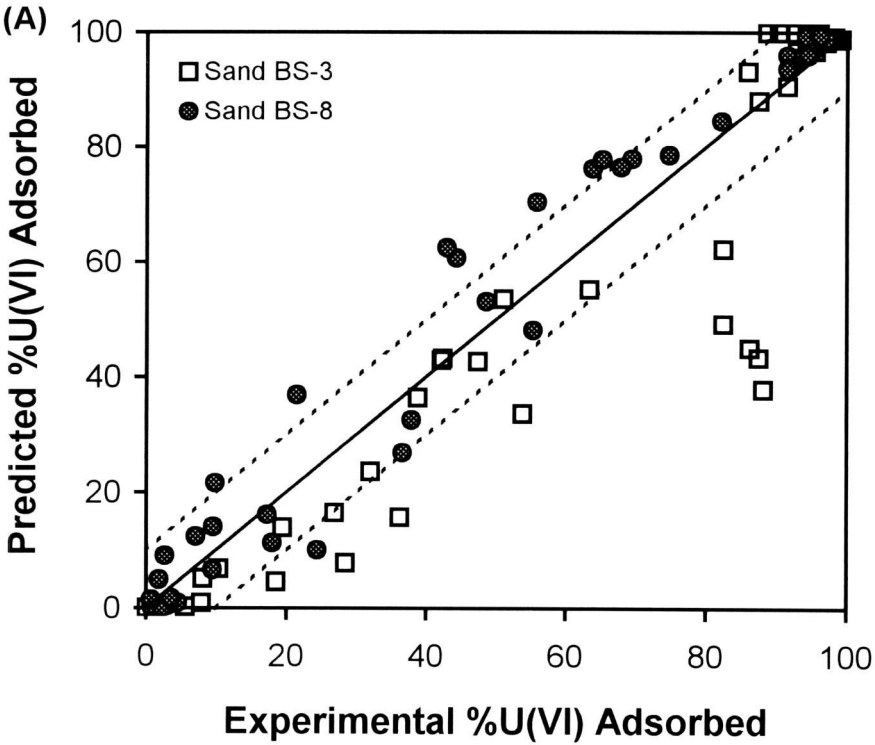
CONTINUED
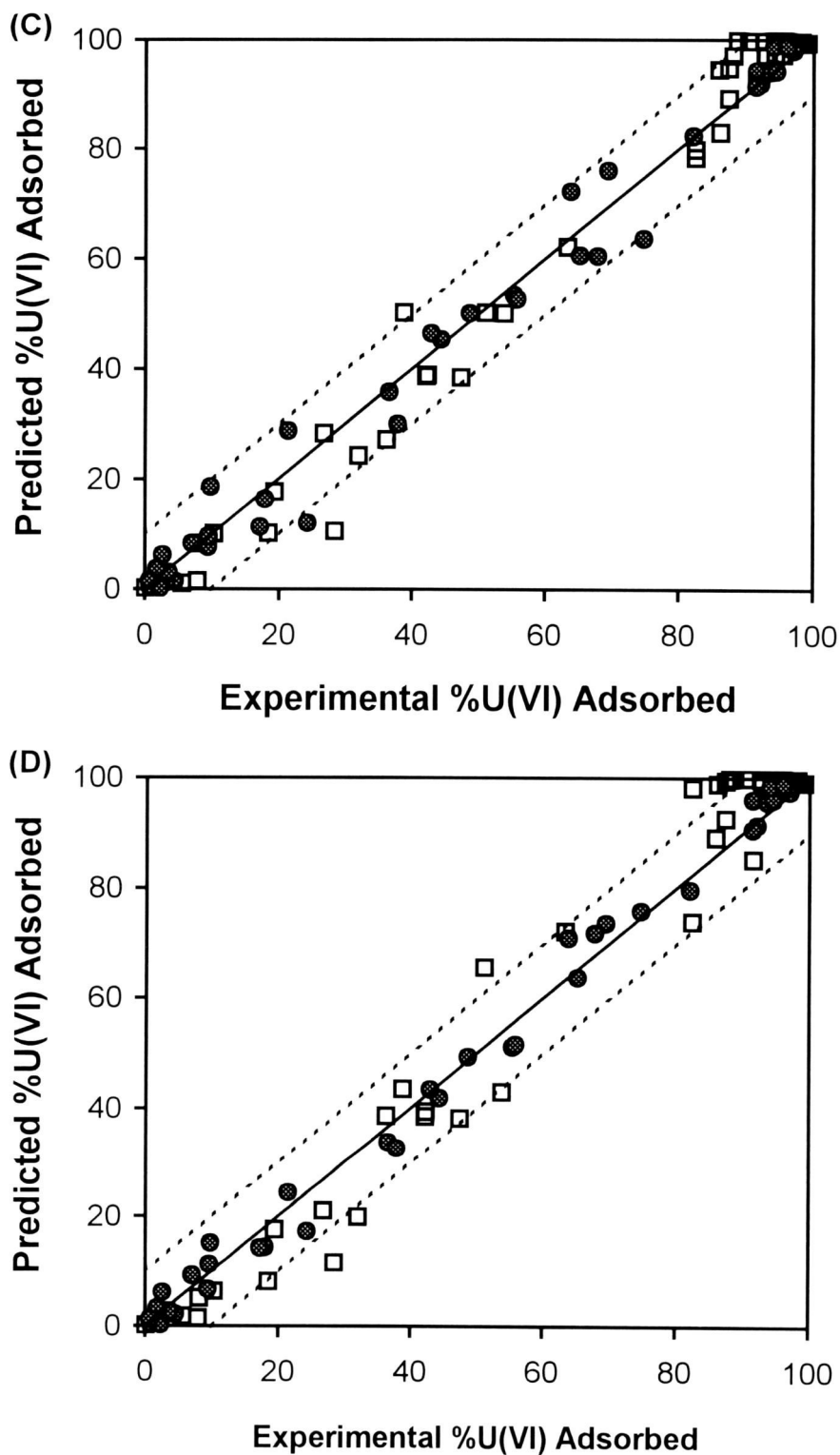
Figure 2.4 (Continued). Linear representations of the goodness of the fit for the Models I-IV on Sand BS-8 and BS-3. 20 g/L sand, 0.1-100 μM U(VI), 0.01 M $NaClO_4$ with system open to atmospheric CO_2. A) Model I; B) Model II; C) Model III; D) Model IV. The dashed lines represent ±10% of the fraction adsorbed.

Model I – Classical SCM; Fixed Site Concentration

Waite et al. (1994) suggested a comprehensive diffuse double layer SCM to describe U(VI) adsorption on ferrihydrite with variations in pH, total UO_2^{2+} concentration, p_{CO_2}, ionic strength, and total ferrihydrite Fe. These workers used extended X-ray absorption fine structure (EXAFS) to characterize the U(VI) species adsorbing on ferrihydrite and found evidence for bidentate mononuclear uranyl complexes adsorbed to the ferrihydrite surface. Also, a poor fit of the U(VI) adsorption data on ferrihydrite with a single-site model led these workers to use two types of ferrihydrite sites (strong and weak) to better describe the adsorption of U(VI). Two site types have also been used by other workers when describing adsorption by ferrihydrite (Dzombak and Morel, 1990). The adsorption reaction of U(VI) to ferrihydrite postulated by Waite et al. (1994) is reported below (Equation 2.4) with reaction constants of log K (I = 0.1, 25 °C) = -2.57 and log K (I = 0.1, 25 °C) = -6.28 for strong and weak ferrihydrite sites, respectively.

$$Fe(OH)_2 + UO_2^{2+} = FeO_2UO_2 + 2H^+ \qquad (2.4)$$
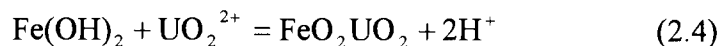
Carbonate has a well-known influence on the adsorption of UO_2^{2+} on oxides causing desorption at pH values above approximately 7 (depending on ionic strength and p_{CO2}) (Hsi and Langmuir, 1985; Lieser et al., 1992). A carbonato surface species was postulated by Waite et al. (1994) to explain the adsorption behavior of UO_2^{2+} at relatively high pH values. The stoichiometry of the carbonato species is reported Equation 2.5 with reaction constants of log K (I=0.1, 25 °C) = 3.67 and log K (I=0.1, 25 °C) = -0.42 for strong and weak ferrihydrite sites, respectively.

$$Fe(OH)_2 + UO_2^{2+} + CO_3^{2-} = FeO_2UO_2CO_3^{2-} + 2H^+ \qquad (2.5)$$

Table 2.4. Solution speciation reactions of UO_2^{2+} with most stability constants from Grenthe et al. (1992).

Reaction	log K (I=0, 25 °C)
$UO_2^{2+} + H_2O = UO_2OH^+ + H^+$	-5.20
$UO_2^{2+} + 2H_2O = UO_2(OH)_2 + 2H^+$	-12.0
$UO_2^{2+} + 3H_2O = UO_2(OH)_3^- + 3H^+$	-20.0
$UO_2^{2+} + 4H_2O = UO_2(OH)_4^{2-} + 4H^+$	-33.0
$2UO_2^{2+} + H_2O = (UO_2)_2OH^{3+} + H^+$	-2.80
$2UO_2^{2+} + 2H_2O = (UO_2)_2(OH)_2^{2+} + 2H^+$	-5.63
$3UO_2^{2+} + 4H_2O = (UO_2)_3(OH)_4^{2+} + 4H^+$	-11.90
$3UO_2^{2+} + 5H_2O = (UO_2)_3(OH)_5^+ + 5H^+$	-15.56
$3UO_2^{2+} + 7H_2O = (UO_2)_3(OH)_7^- + 7H^+$	-31.0
$4UO_2^{2+} + 7H_2O = (UO_2)_4(OH)_7^+ + 7H^+$	-21.9
$UO_2^{2+} + CO_3^{2-} = UO_2CO_3$	-8.30
$UO_2^{2+} + 2CO_3^{2-} = UO_2(CO_3)_2^{2-}$	-19.0
$UO_2^{2+} + 3CO_3^{2-} = UO_2(CO_3)_3^{4-}$	-32.37
$2UO_2^{2+} + CO_3^{2-} + 3H_2O = (UO_2)_2 CO_3(OH)_3^- + 3H^+$	-19.18[a]

[a] Stability constant from Tripathi (1983). Other aqueous reaction constants from Grenthe et al. (1992)

It should be noted that protonation/deprotonation reactions and adsorption of HCO_3^- and CO_3^{2-} to the iron surface were also considered by Waite et al. (1994) but are not reported here.

Reactions of UO_2^{2+} in solution and corresponding equilibrium constants (Tripathi, 1983; Grenthe et al., 1992) are reported in Table 2.4. The large number of solution reactions of U(VI) give an indication of the complex nature of U(VI) solution reactions.

Waite et al. (1994) used the two-site model described above to characterize the adsorption of UO_2^{2+} on synthesized ferrihydrite. The two-site model produced an excellent fit of ferrihydrite adsorption data gathered by Waite et al. (1994). The model predicted adsorption of U(VI) at 10 nM and 1 μM extremely well with a slightly worse fit

at higher concentrations of U(VI). Experimental error estimates for U(VI) adsorption on the natural sands for the current study where used to calculate a χ^2/N value of 0.0085 for U(VI) adsorption on ferrihydrite (Waite et al., 1994). This value of χ^2/N can be used for comparison to the other models presented.

The two-site classical SCM described above (Model I) was applied directly to the natural sand data by approximating total *ferrihydrite iron* with experimentally measurable *DCB extractable iron* when determining the individual site concentrations for U(VI) adsorbing sites. Waite et al. (1994) suggested a weak site/ferrihydrite Fe ratio of 873 mmol weak sites/mol Fe with the number of available sites determined directly from the total iron added to the adsorption experiment. Therefore, in this study, the weak site concentrations for Model I were fixed at 873 mmol weak sites/mol DCB extractable Fe. The strong site concentrations were fixed in a similar manner at 1.8 mmol strong sites/mol DCB extractable Fe for Model I.

This approximation can be justified by assuming the DCB extractable iron contained in the natural sands acts primarily as ferrihydrite, even though the bulk of the iron in the sorbent may be best described as goethite. Also, the DCB extractable iron is assumed to be responsible for most of the U(VI) adsorption. Evidence supporting this approximation was found by Payne et al. (1994). These workers showed that adsorption of U(VI) decreased greatly when weathered schists were extracted with DCB reagent. Reported in Table 2.5 are the strong and weak site concentrations using this estimation of total "ferrihydrite" iron. The surface area of the natural sands, which is necessary for application of the diffuse layer model (DLM) of the electric double layer, was measured

Table 2.5. Extractable iron and surface site concentrations for six natural sands.

Sample	Iron (μmol/g)[a]	Model[b,c]	Weak Sites (μmol/g)[d]	Strong Sites (nmol/g)[e]	Strong Sites (mmol sites /mol Fe)[f]
BS-3	12.8	I	11.2	23.0	1.80
		II	11.2	44.1	3.45
BS-4	3.1	I	2.7	5.58	1.80
		II	2.7	18.8	6.06
BS-5	10.2	I	8.9	18.4	1.80
		II	8.9	5.93	0.58
BS-6	4.8	I	4.2	8.64	1.80
		II	4.2	6.51	1.36
BS-7	7.1	I	6.2	12.8	1.80
		II	6.2	30.8	4.34
BS-8	4.1	I	3.6	7.38	1.80
		II	3.6	16.2	3.95

[a] DCB extractable iron for sand samples. Sample characteristics reported in Table 2.1.
[b] Model I created directly from Waite et al. (1994) model.
[c] Model II site concentration determined from FITEQL optimization of the strong site concentration for 1 μM U(VI) adsorption data.
[d] Waite et al. (1994) utilized a weak site concentration of 873 mmol weak sites/mol ferrihydrite Fe. In this work a ratio of 873 mmol weak sites/mol DCB extractable Fe was used for both Models I and II.
[e] Determined directly from 1.8 mmol strong sites/mol DCB extractable iron for Model I and determined by FITEQL optimization of the strong site concentration for Model II.
[f] Where mol Fe = mol DCB extractable Fe from Table 2.1.

directly and is reported in Table 2.1. The CEC and the DCB extractable Al were not used to parameterize Model I.

Figures 2.3 and 2.5 show the predictions of Model I when applied to the data from natural sands. The solid lines denote model predictions while the symbols are experimental adsorption data. Figure 2.5 shows the prediction by Model I of the experimental data gathered with a range of U(VI) concentrations on sand sample BS-8. Predictions of adsorption data on samples BS-4, BS-5, BS-6, and BS-7 gathered at 1 μM U(VI) are shown in Figs. 2.3a, 2.3b, 2.3c, and 2.3d, respectively. χ^2/N values for prediction of adsorption behavior range from 36-5.1 for 1 μM U(VI). χ^2/N values for the

prediction of all four concentrations of U(VI), are 53 and 22, for sands BS-3 and BS-8, respectively (Table 2.2).
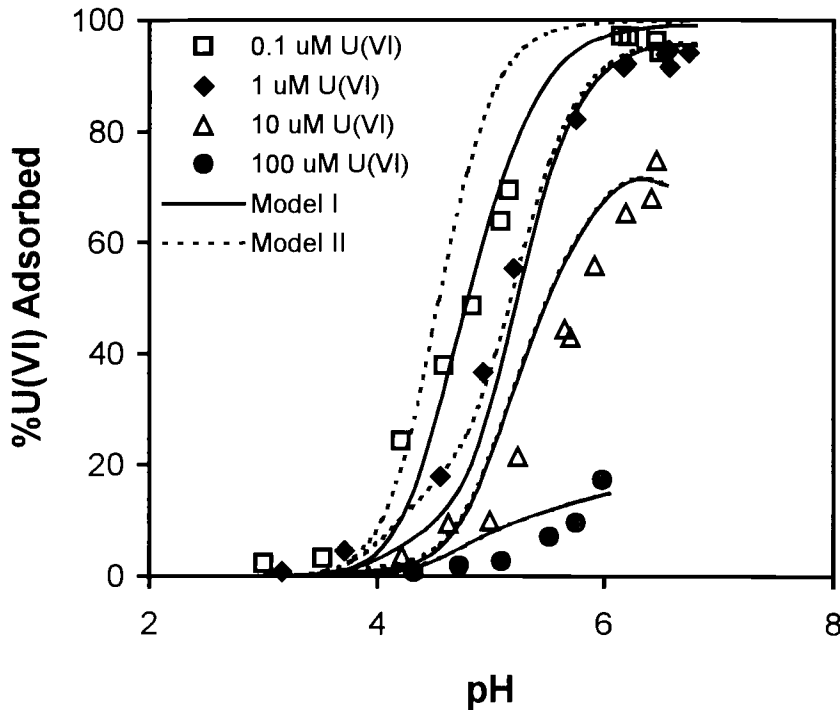
Figure 2.5. Model I and II predictions of pH adsorption edge data. 20 g/L sand sample BS-8, 0.01 M NaClO$_4$, p$_{CO2}$ = 10$^{-3.5}$ atm, and 0.1-100 μM U(VI).

Model I predicts the adsorption data quite well considering the assumptions made to apply the model to the data and the inherent oversimplification of describing heterogeneous natural materials with a model designed for one pure, laboratory synthesized material. Model I predicts the adsorption data particularly well for sand BS-8 (Fig. 2.5), BS-5 (Fig. 2.3b), and BS-6 (Fig. 2.3c). Only for sands BS-3 (not shown) and BS-4 (Fig. 2.3a) did the model fail to fit the data adequately, as illustrated by the large value of χ^2/N for sand BS-3 (χ^2/N = 53), and BS-4 (χ^2/N = 36). Also, it should be noted that for sand BS-3 the model "severely" fails to predict adsorption of U(VI) at 100 μM

U(VI) and pH values greater than 6. The model predicted much lower adsorption than was experimentally observed.

The excellent description of experimental adsorption data by Model I for 0.1 and 1 μM U(VI) may occur because the original two-site model used to describe U(VI) adsorption on ferrihydrite was calibrated at low U(VI) concentrations. For pH values ranging from 3-6, the Waite et al. (1994) model described U(VI) adsorption on ferrihydrite at 10 nM and 1 μM U(VI) better than it described adsorption of 10 and 100 μM U(VI). Therefore, the extrapolation of the laboratory based model to natural sands may have exaggerated the discrepancy between the model and the adsorption data at higher concentrations of U(VI). Also, other constituents in the natural sands (e.g., Al-oxide) may become dominant sorbents at higher concentrations of U(VI), as the "ferrihydrite" type sites become saturated with respect to U(VI). Incorporation of surface reactions for these different constituents may have provided a better description of the adsorption data.

The excellent prediction of adsorption data at low concentrations by Model I provides evidence to the validity of gathering thermodynamic reaction constants for application to environmental adsorption.

Model II – Classical SCM; Fit Site Concentration

Model II includes the same surface reactions, solution reactions, and treatment of the EDL as Model I. The strong site concentration of Model II was adjusted to best describe the 1 μM U(VI) adsorption data for each individual sand sample. This approach was used to test the suggestion that if a model is applied to data gathered in "foreign"

systems (materials not used in the original development of the model), calibration of the model may be necessary for accurate predictions of the data (Bose and Reckhow, 1997). Calibration is achieved by using one set of conditions that are considered to be representative of the entire data set and fitting the model to the data under this set of conditions. Then prediction of data gathered under a different (but similar) set of conditions is attempted.

The strong site concentration was adjusted to best describe the adsorption data at 1 μM U(VI). The weak site concentration was set at 873 mmol weak sites/mol DCB extractable Fe (as in Model I). Adjusting only the strong site concentration was the technique employed by Waite et al. (1994) when fitting adsorption of UO_2^{2+} to ferrihydrite. FITEQL4.0 (Herbelin and Westall, 1999) was used to fit the adsorption data by minimizing χ^2/N.

Excellent agreement between the model and the data was achieved for 1 μM U(VI) when the strong site concentration was adjusted (χ^2/N ranging from 13-1.3). The strong and weak site concentrations for Model II are reported in Table 2.5. Figure 2.6 illustrates the correlation of the strong site/extractable Fe ratio for the natural sands in this study and the ratio suggested by Waite et al. (1994). There appears to be some general correlation between an increase in DCB extractable Fe and the strong site concentration found to best describe the data, but no specific correlation between the adjusted strong site concentration and the DCB extractable Fe could be found.
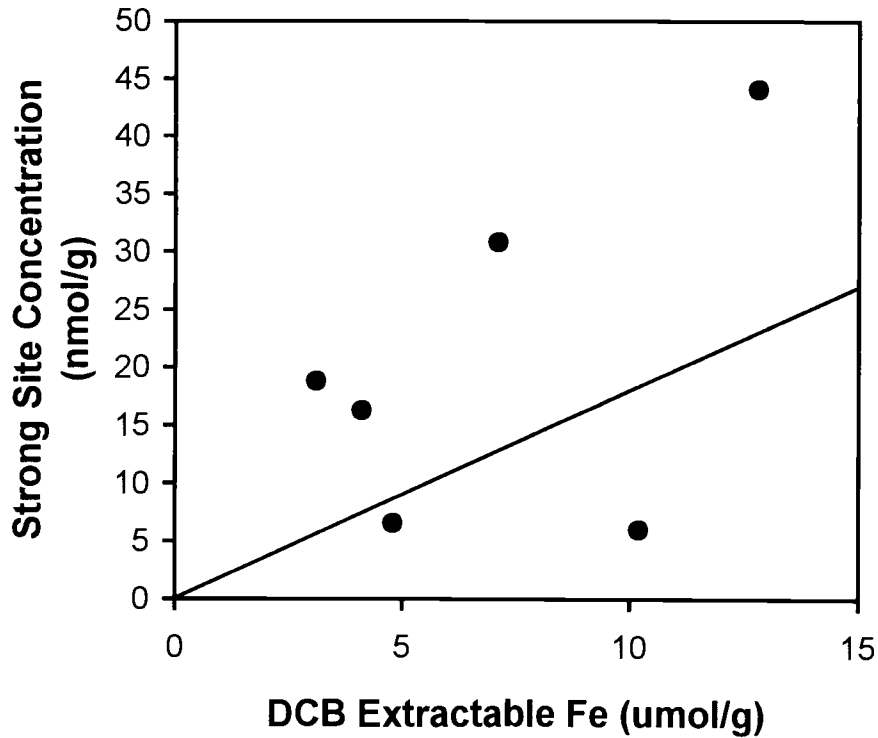
Figure 2.6. Comparison of the strong site concentration/ferrihydrite Fe ratio of 1.8 mmol strong sites/mol Fe (line) suggested by Waite et al. (1994) to the strong site concentration/DCB extractable Fe ratio for Model II found from fitting U(VI) adsorption data at 1 μM U(VI) (solid circles).

The deviation of the suggested ratio and the ratio found for the natural sands can be used as a measure of the predictive capability of the two-site model. As shown by Fig. 2.3a, the experimental adsorption data for sand BS-4 (1 μM UO_2^{2+}) were not predicted very well by Model I ($\chi^2/N = 36$). The fit of the adsorption data for this sand also produced the largest deviation of strong site/DCB extractable Fe from 1.8 mmol strong sites/mol DCB extractable Fe (Table 2.5).

Adsorption data gathered with a range of pH values (3.0-7.6) and total concentrations of UO_2^{2+} (0.1, 10, and 100 μM) were predicted with Model II for two sand samples (BS-3 and BS-8). The application of Model II to pH adsorption edge data

gathered for sample BS-8 is shown in Fig. 2.5. χ^2/N values for sand samples BS-3 and BS-8 are reported in Table 2.2.

The predictions of Model II for sand BS-3 did not appreciably change except for 0.1 µM U(VI) (not shown). The fit of the adsorption data at this concentration did improve, yet with so few data points on the actual pH adsorption edge (Fig. 2.2a), the improvement of the prediction is hard to verify. For sand BS-3, the improved interpolation at 0.1 and 1 µM U(VI) decreased χ^2/N from 53 for Model I to 42 for Model II. For sand BS-8, the predictions of Model II were not as accurate as Model I for data collected at 0.1 µM U(VI) (Fig. 2.5), and were approximately the same for the other concentrations of U(VI). The χ^2/N value actually increased from 22 to 28 with calibration of the model, which is mainly due to the poor description of 0.1 µM U(VI) adsorption data for Model II and only slight improvement in the interpolation of 1 µM U(VI) adsorption (χ^2/N decreased from 7.5 to 1.3).

As with Model I, the two-site model fails to predict the data from the natural sands for certain concentrations of UO_2^{2+}. There is a pronounced underprediction of the U(VI) adsorbed at 100 µM total UO_2^{2+} for sand BS-3 (not shown) for both applications of the model, indicating that the "ferrihydrite" type sites associated with the natural sands may be saturated with respect to UO_2^{2+}, and other types of sites may be dominant at these higher total UO_2^{2+} concentrations. Also, when Model II is applied to adsorption data for sample BS-8 at 0.1 µM UO_2^{2+}, it overpredicts the U(VI) sorbed (Fig. 2.5).

Model II does not offer a significant improvement over Model I. First, Model II does not significantly improve the interpolation of the U(VI) adsorption data when compared to Model I (except for the data used in the calibration of Model II). Second,

Model II is less portable than Model I. Calibration of the strong site concentration for each individual sand must be accomplished before application of Model II, whereas Model I can be applied to an individual sand as long as the DCB extractable Fe is known. Third, the calibration of Model II is a tedious extra step that produces inconsistent results.

Model III - Affinity spectrum SCM; Fit Site Concentrations; Fixed Reaction Constants

Clearly, Models I and II generally predict adsorption of U(VI) to the iron-coated silica sands for which they were not explicitly intended to be applied. Yet, the inability of Models I and II to interpolate data at certain concentrations of U(VI) may limit the use of these models for accurate predictions of U(VI) transport through iron-coated silica sands, especially at higher concentrations of U(VI). If a more accurate interpolation of data is necessary, an affinity spectrum approach can be applied, in which the experimental data gathered on the sorbent of interest are fit as accurately as possible. One affinity spectrum approach which has been used extensively is the DLKS (Černík et al., 1995). When adsorption to a heterogeneous environmental sorbent is considered, a DLKS approach can be used to simplify adsorption reactions into a fixed grid of stability constants (Westall et al., 1998). This approach has been used to model adsorption to heterogeneous sorbents such as Co adsorption on humic substances (Westall et al., 1995) and sorption of Sr^{2+} and H^+ on ferrihydrite (Černík et al., 1996).

The DLKS approach is a means of simplifying the "ill-posed" numerical problem of decomposing the overall adsorption characteristics of a heterogeneous sorbent into sorption of individual sites (Westall et al., 1995). When using the DLKS approach, a range of log K values called a spectral window and a constant Δlog K are chosen for

parameterization of surface affinity. If these values are chosen correctly, the data can be

adequately fit with a small and orderly set of log K values within the spectral window.

The site concentrations of the individual sites are used as fitting parameters to generate

the best description of the data. Some sites within the window may not contribute to the

overall fit of the data and are removed from the model until an appropriate combination

of log K values and site concentrations is found. Also, sites contributing to adsorption

may be totally saturated or unsaturated over the concentration range of interest. These

sites lie outside the spectral window, but contribute to adsorption. In Equation 2.6, these

sites occur when either $K_n \rightarrow 0$, corresponding to a simple linear isotherm (K_{lin}), or $K_n \rightarrow \infty$

corresponding to a constant (T_o) (Černík et al., 1995). Equation 2.6 represents the

individual site contribution to the adsorbed concentration at a single data point (q_i).

$$q_i = T_o + \sum_{n=1}^{M} \frac{K_n c_i}{1 + K_n c_i} T_n + K_{lin} c_i \qquad (2.6)$$

where c_i is the aqueous U(VI) concentration at data point i, T_n is the total site

concentration of an individual site n, and M is the total number of sites in a spectral

window.

The solution reactions used for the classical models (Models I and II) were also

used for Model III and are presented in Table 2.4. The general adsorption reactions in

Model III are described in Equations 2.7 and 2.8.

$$X_j(OH)_2 + UO_2^{2+} = X_jO_2UO_2 + 2H^+ \qquad (2.7)$$

$$X_j(OH)_2 + UO_2^{2+} + CO_3^{2-} = X_jO_2UO_2CO_3^{2-} + 2H^+ \qquad (2.8)$$
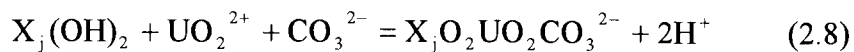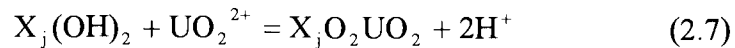
The adsorption reactions in Equations 2.7 and 2.8 have the same stoichiometry as

those used in Models I and II (Equations 2.4 and 2.5). Stability constants for Model III

are reported in Table 2.6 along with the site concentrations of the individual sites in mol

sites/mol DCB extractable Fe (or Al). A Δlog K of 2 was chosen to fit the pH adsorption

edge data gathered for the natural sands with a log K window of -1 to -7 for UO_2^{2+}

adsorption (Equation 2.7) and -11 to -17 for UO_2CO_3 (Equation 2.8). Also, electrostatics

of the sand surface, protonation/deprotonation reactions, HCO_3^- adsorption, and CO_3^{2-}

adsorption were not explicitly considered in the model, rather they are inclusively

modeled as contributors to site heterogeneity when fitting the pH adsorption edge data for

the natural sands. This may be considered to be an oversimplification of the model, but

others working with pure materials have found that an adequate representation of the data

can be achieved without explicit consideration of the EDL (Kohler et al., 1996). Also,

when explicitly considering the EDL one must make approximations about the geometry

of the surface which are generally not good assumptions when the sorbent is not well

characterized.

It should be noted that surface area data are not essential when modeling the EDL

implicitly. Also, the cation exchange capacity was not necessary to parameterize

Model III. This reduces the amount of data necessary to apply the model. In addition,

because of the pH dependent dissolution of the natural sands, titration data could not be

easily gathered with the necessary certainty to be included in the model. This precluded

the use of protonation reactions of the iron-coated sands explicitly.

Only adsorption data from sand BS-3 and sand BS-8 were used when compiling a

comprehensive DLKS surface complexation model (Model III). Two separate models for

each sorbent were produced and then integrated into one model. Individual sites that were

not important for both sands were deleted and the data were refit using only sites with

appreciable concentrations (relative to the lowest U(VI) concentration studied). This was a necessary step to ensure portability of the final model and generally led to a loss in accuracy for each individual sand. To assure portability of the model to similar sands the site concentrations were related to the DCB extractable Fe or Al. Relating the site concentrations of the sands to the extractable Fe (Al) was accomplished through plotting the relationship between the site concentrations of each individual site and DCB extractable Fe or Al for two sand samples (BS-3 and BS-8). A linear relationship with an intercept of zero were prerequisites, such that a simple correlation could be made between DCB extractable Fe and individual site concentrations.

Table 2.6. Parameters for Model III and Model IV describing UO_2^{2+} adsorption on natural sands.

Model	Site	Surface Sites (mmol sites/mol Fe)[c]	Surface Sites (mmol sites/mol Al)[c]	log K (UO_2^{2+})	log K (UO_2CO_3)
III[a]	1	0.135	-	-1	-17
	2	3.19	-	-3	-17
	3	-	22.7	-5	-17
	4	$K_{lin}*(UO_2^{2+})$: -6.74[d] $K_{lin}*(UO_2CO_3)$: -16.74[d]	-	-7	-17
IV[b]	1	0.30	-	-1.012	-12.897
	2	5.08	-	-3.412	NA
	3	-	66.3	-5.944	NA
	4	$K_{lin}*(UO_2^{2+})$: -6.60[d] $K_{lin}*(UO_2CO_3)$: -15.91[d]	-	-7.168	-16.475

[a] Stability constants determined from a Δlog K value of -2 and a grid from -1 to -7 for UO_2^{2+} adsorption and -11 to -17 for UO_2CO_3 adsorption. Site concentrations determined from FITEQL optimization for sand samples BS-3 and BS-8 with four total U(VI) concentrations and a range of pH values (3-7.6).
[b] Stability constants and site concentrations determined from FITEQL optimization for sand samples BS-3 and BS-8 with four total U(VI) concentrations and a range of pH values (3-7.6).
[c] The measure of mol Fe (Al) is DCB extractable Fe (Al).
[d] $K_{lin}*$ was calculated by multiplying the site concentration (in mol sites/mol Fe) by the stability constant for the adsorption of UO_2^{2+} or UO_2CO_3.

The ratios of site concentration/DCB extractable Fe (Al) used for the Model III are reported in Table 2.6. The fit of these concentrations to the data for BS-3 and BS-8

gave a χ^2/N of 9.9 and 8.9, respectively. The fit of the adsorption data for sand sample

BS-8 is shown in Fig. 2.7. Model III described the data very well. The large deviation of

Model I and Model II at 100 μM U(VI) for sand BS-3 is decreased when Model III is

applied (Fig. 2.4). Also, Model III describes adsorption of sand BS-8 at 0.1 μM U(VI)

better than Models I and II (Figures 2.5 and 2.7).
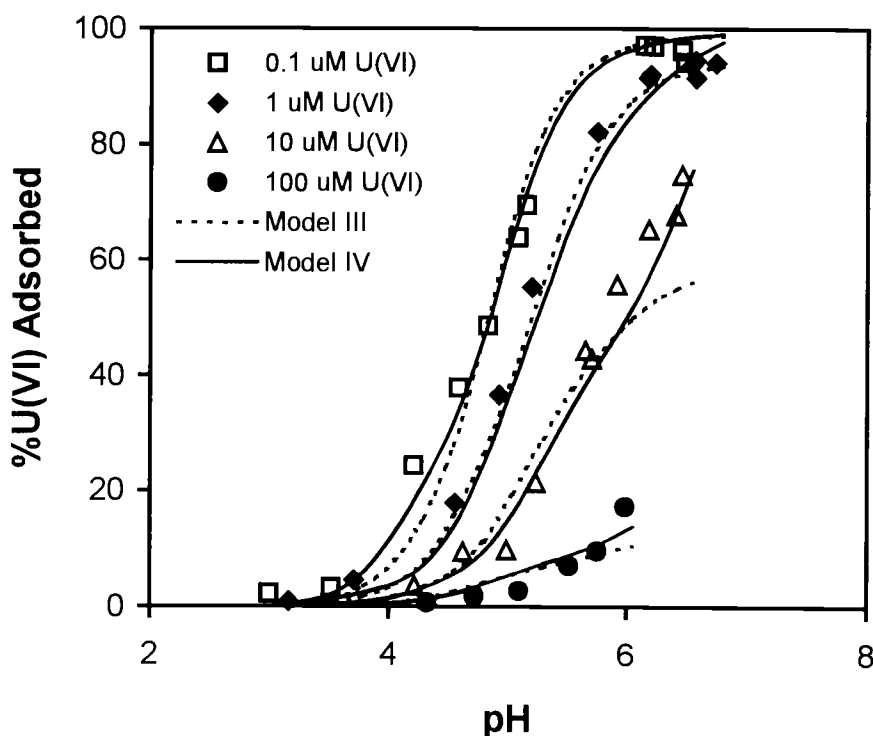
Figure 2.7. Description of U(VI) adsorption data by Models III and IV.
20 g/L sand sample BS-8, 0.01 M NaClO$_4$, p$_{CO2}$ = 10$^{-3.5}$ atm, and
0.1-100 μM U(VI).

Overall, the description of the data is better for Model III than for Models I or II,

as illustrated by comparison of χ^2/N the both models (Table 2.2). This result would be

expected from fitting, instead of predicting, the adsorption data. The description of sand

BS-3 improves from a χ^2/N of 53 for Model I to 9.9 for Model III and for sand BS-8 the

χ^2/N improves from 22 for Model I to 8.9 for Model III. Overall, predictions of Model III are very good, with only sand BS-5 and BS-6 not as accurately predicted as Model I (Fig. 2.3). Overall, Model III is more accurate than any of the previously discussed modeling approaches.

Model IV - Affinity Spectrum SCM; Fit Site Concentrations; Fit Reaction Constants

Another affinity spectrum approach to modeling adsorption data is to simply fit the site reaction constants as well as the site concentrations for each individual adsorbing site (Model IV). This approach can be thought of as using an infinitely small $\Delta\log K$ and an infinitely large spectral window for Model III. Model IV is used to obtain the most accurate interpolation of the data possible. This approach is a global minimization of both total site concentrations and the stability constants for UO_2^{2+} and UO_2CO_3 adsorption.

A comprehensive model was constructed and the site concentration/DCB extractable Fe (Al) ratios were found as described above for Model III. These site concentrations are reported in Table 2.6. The stability constants for Model IV are relatively similar to those found for Model III (Table 2.6). Also, K_{lin} is almost the same for both modeling approaches. Comparison of Model III to Model IV indicates that similar affinity spectrums can be reached from both approaches. It also shows that careful selection of $\Delta\log K$ and a log K window can produce models that are very accurate with a limited number of adjustable parameters.

The fit of the pH adsorption edges for the sand samples produced a χ^2/N for BS-3 and BS-8 of 14 and 4, respectively (Table 2.2). The fit of the adsorption data for sand BS-8 is shown in Fig. 2.7. The data are fit extremely well by Model IV, which is illustrated

by the comparison of Fig. 2.5 to Fig. 2.7. Any systematic deviation between Model I and the data is not apparent when applying Models III and IV for sand BS-8. For sand BS-3, there is only a slight deviation of Model IV from the data at 100 μM U(VI) (not shown).

Predictions of U(VI) adsorption by Model IV are also quite accurate (Fig. 2.3), with sand BS-5 and BS-6 not as accurately predicted as with Model I. Comparison of χ^2/N values for Models I-IV (Table 2.2) and the linear representations of Models I-IV (Fig. 2.4) indicates that Model IV interpolates the data more accurately than Models I and II, but the interpolation is approximately the same as Model III.

It should be noted that because Site 4 in Models III and IV does not approach saturation, extrapolation of these two models to higher pH values may result in large deviations of the models from the true adsorption characteristics of the sands. If Models III and IV are applied to adsorption data at higher pH values, the site concentrations of Sites 3 and 4 should be reevaluated for Models III and IV along with the reaction constants for Model IV.

Conclusions

Table 2.2 provides a summary of the models evaluated in this study. As may be seen in the table, the level of complexity (i.e., number of estimated parameters) of the model increase as one moves down the table from Model I to IV. Examination of the last column (χ^2/N) of the table allows striking conclusions to be reached regarding the application and suitability of the modeling approach for real material. First, the DLKS models (III and IV) are more effective at representing real material over a range of uranium concentrations than are the simpler two-site pure phase models (I and II).

Second, it appears that the differences between parameterization approaches for specific models (I and II or III and IV) have much less effect on χ^2/N and the predictive accuracy of the models than the differences between calibration approaches (ferrihydrite vs. natural sands). Third, at least for Oyster Sands, a classical DLM using published parameters derived for pure phases and simple characterization measurements predicts adsorption to natural materials remarkable well.

Often, the characterization of adsorption behavior of sediments supports goals related to evaluating transport at a physically and chemically heterogeneous site. Site characterization has two (sometime conflicting) goals, these being understanding the spatial distribution of characteristics import to transport and understanding in detail the interfacial processes retarding migrating solutes. Results from this study provide insight into experimental design and trade-offs associated with characterization of adsorption behavior.

Results indicate that preliminary modeling can be conducted with literature derived DLM coefficients for hydrous ferric oxide and the assumption that DCB extractable iron is an adequate representation of the sediment reactivity. Although, a few site specific adsorption experiments should be conducted to evaluate the validity of these assumptions, determining single concentration adsorption edges for multiple site samples provide very little additional practical information because site specific calibration of the DLM does not significantly improve its predictive capabilities. Furthermore, single concentration pH edges are inadequate to parameterize and allow the use of the more accurate DLKS models. As a result, site characterization should focus on the

determination of the spatial distribution of characteristics that control adsorption such as DCB extractable iron.

Detailed modeling that considers wide ranges of concentration require that enough adsorption experiments be conducted to parameterize a DLKS model. This parameterization relies upon adsorption edges at multiple concentrations or isotherms at several pH values. However, it appears that the reaction constants for each site can be fixed (Model III) and that only the concentrations of reactive site need to be adjusted. Given fixed resources to characterize the adsorption properties of site materials, collecting pH edges at multiple concentrations on fewer samples is more advantageous than collecting single concentration pH edges on many samples. An intriguing characterization design not explored here is the collection of single pH edges on multiple samples with the uranium concentration being different for each sample coupled with a global (all samples simultaneously) regression analysis to provide DLKS parameters consistent with multiple samples and locations. Such global optimization requires reevaluation of the current approaches to fitting constants that are currently embodied in FITEQL.

Acknowledgments

References

Bailey E. H., Kemp A. J., and Ragnarsdottir K. V. (1993) Determination of Uranium and Thorium in Basalts and Uranium in Aqueous Solution by Inductively Coupled Plasma Mass Spectrometry. *J. Anal. At. Spectrom.* **8**, 551-556.

Bertetti, F. P., Pabalan R. T., Turner D. T., and Almendarez M. (1995) Experimental and Modeling Study of Uranium(6+) Sorption on Quartz. Draft manuscript, Center for Nuclear Waste Regulatory Analyses, San Antonio, TX.

Bose P. and Reckow D. A. (1997) Modeling pH and Ionic Strength Effects on Proton and Calcium Complexation of Fulvic Acid: A Tool for Drinking Water-NOM Studies. *Environ. Sci. Tech.* **31**, 765-770.

Brunauer S., Emmett P. H., and Teller E. (1938) Adsorption of Gases in Multimolecular Layers. *J. Am. Chem. Soc.* **60**, 309-319.

Černík M., Borkovec M., and Westall J. C. (1995) Regularized Least-Squares Methods for the Calculation of Discrete and Continuous Affinity Distributions for Heterogeneous Sorbents. *Environ. Sci. Tech.* **29**, 413-425.

Černík M., Borkovec M., and Westall J. C. (1996) Affinity distribution Description of Competitive Ion Binding to Heterogeneous Materials. *Langmuir* **12**, 6127-6137.

Cowan C. E., Zachara J. M., Smith S. C., and Resch C. T. (1992) Individual Sorbent Contributions to Cadmium Sorption on Ultisols of Mixed Mineralogy. *Soil Sci. Soc. Amer. J.* **56**, 1084-1094.

Davis J. A. and Kent D. B. (1990) Surface complexation modelling in aqueous geochemistry. In *Mineral-Water Interface Geochemistry* (ed. M.F. Hochella and A.F. White); *Rev. Mineral.* **23**, pp. 177-260.

DeFlaun M. F., Murray C. J., Holben W., Scheibe T., Mills A., Griffin T., Majer E., and Wilson, J. L. (1997) Preliminary observation on bacterial transport in a coastal plain aquifer. FEMS *Microbiol. Review* **20**, 473-487.

Dzombak A. D. and Morel F. M. M. (1990) *Surface Complexation Modeling: Hydrous Ferric Oxide.* John Wiley and Sons.

Greenberg A. E., Clesceri L. S., and Eaton A. D. (1992) *Standard Methods for the Examination of Water and Waste Water.* American Public Health Association.

Grenthe I., Fuger J., Lemire R. J., Muller A. B., Nguyen-Trung C., and Wanner H. (1992) *Chemical Thermodynamics of Uranium.* Elsevier.

Herbelin A. L. and Westall J. C. (1999) *FITEQL: A Computer Program for Determination of Chemical Equilibrium Constants from Experimental Data, Version 4.0.* Chemistry Department, Oregon State Univ.

Hesse P.R. (1971) *A Textbook of Soil Chemical Analysis*. Chemical Publishing Company.

Hsi C. D. and Langmuir D. (1985) Adsorption of Uranyl onto Ferric Oxyhydroxides: Application of the surface complexation site-binding model. *Geochim. Cosmochim. Acta* **49**, 1931-1941.

Jackson M. L., Chin H. L., and Zelazny L. W. (1986) Oxides, Hydroxides, and Aluminosilicates. In *Methods of Soil Analysis* (ed. A. Klute) Vol. 1, Chap. 6, pp. 101-150. Soil Science Society of America.

Kohler M., Curtis G. P., Kent D. B., and Davis J. A. (1996) Experimental Investigation and Modeling of Uranium(VI) Transport under Variable Chemical Conditions. *Water Resour. Res.* **32**, 3539-3551.

Lieser K. H., Quandt-Klenk S., and Thybusch B. (1992) Sorption of Uranyl Ions on Hydrous Silicon Dioxide. *Radiochim. Acta* **57**, 45-50.

Loux N. T., Brown D. S., Chafin C. R., Allison J. D., and Hassan S. M. (1989) Chemical Speciation and Competitive Cationic Partitioning on a Sandy Aquifer Material. *Chem. Speciation Bioavailability* **1**, 111-125.

McKinley J. P., Zachara J. M., Smith S. C., and Turner G. D. (1995) The influence of uranyl hydrolysis and multiple site binding reactions on adsorption of U(VI) to montmorillonite. *Clays Clay Mineral.* **43**, 586-598.

Mixon R. B. (1985) Stratigraphic and geographic framework of uppermost Cenozoic deposits in the southern Delmarva Peninsula, Virginia and Maryland. *USGS Profess. Pap.* 1067-J.

Mueller B. and Sigg L. (1990) Interaction of Trace Metals with Natural Particle Surfaces: Comparison between adsorption experiments and field measurements. *Aquatic Sci.* **52**, 75-92.

NAG Fortran Library, Mark 16 (1993), Numerical Algorithm Group Ltd., Wilkinson House, Jordan Hill Road, Oxford, UK OX2 8DR.

Pabalan R. T., Turner D. R., and Bertetti F. P. (1994) *Sorption Modeling for High Level Waste Performance Assessment; NRC High-Level Radioactive Waste Research at CNWRA January-June, 1994*. Center for Nuclear Waste Regulatory Analyses, San Antonio.

Payne T. E., Davis J. A. and Waite T. D. (1994) Uranium Retention by Weathered Schists: The role of Iron Minerals. *Radiochim. Acta* **66/67**, 297-303.

Redden G., Li J., and Leckie J. (1998) Adsorption of Uranium (VI) and citric acid on Goethite, Gibbsite, and Kaolinite: Comparing Results for Binary and Ternary Systems. In *Adsorption of Metals by Geomedia* (ed. E.A. Jenne), Chap. 13, pp. 291-315. Academic Press.

Schwetmann U. (1964) Differenzierung der Eisenoxide des Bodens durch photochemische Extraktion mit saurer Ammoniumoxalate-Losung. *Z. Pflansenenahr. Dueng. Bodenk.* **105**, 194-202.

Smith K. S. (1991) Factors Influencing Metal Sorption onto Iron-Rich Sediments in Acid-Mine Drainage. Ph.D. dissertation, Colorado School of Mines.

Tripathi V. S. (1983) Uranium Transport Modeling: Geochemical data and submodels. Ph.D. dissertation, Stanford University.

Waite T. D., Payne T. E., Davis J. A., and Sekine K. (1992) *Uranium Sorption: Alligator Rivers Analogue Proj., Final Rept., 13.* Australian Nuclear Science and Technology Organization.

Waite T. D., Davis J. A., Payne T. E., Waychunas G. A., and Xu N. (1994) Uranium (VI) adsorption to Ferrihydrite: Application of a surface complexation model. *Geochim. Cosmochim. Acta* **58**, 5465-5478.

Westall J. C., Jones J. D., Turner G. D., and Zachara J. M. (1995) Models for Association of Metal Ions with Heterogeneous Environmental Sorbents. 1. Complexation of Co(II) by Leonardite Humic Acid as a Function of pH and $NaClO_4$ Concentration. *Environ. Sci. Technol.* **29**, 951-959.

Westall J. C., Černík M., and Borkovec M. (1998) Modeling Metal Speciation in Aquatic Systems. In *Metals in Surface Waters* (ed. H.E. Allen et. al), Chap. 10, pp. 191-216. Ann Arbor Press.

Chapter 3: U(VI) Adsorption on Natural Iron-coated Silica Sands in the Presence of Citrate: The Role of Surface Alteration

Brian A. Logue[1], Robert W. Smith[2], and John C. Westall[1]*

[1]Department of Chemistry
Oregon State University
Corvallis, OR 97331

[2]Idaho National Engineering and Environmental Laboratory
Idaho Falls, ID 83415

*Corresponding Author, Email: westallj@chem.orst.edu

Abstract

Metal complexing organic ligands can alter the adsorption and transport properties of radionuclide contaminants in the environment. These ligands are components of some radioactive wastes and can also naturally occur in the subsurface environment in appreciable concentrations. In the present study, the adsorption of U(VI) in the presence of citrate was studied over a range of citrate concentrations and pH values. The solid sorbent was a natural iron-rich sand.

Adsorption of U(VI) on the iron-rich sand generally decreased in the presence of increasing concentrations of citrate. Adsorption of citrate to the sand also decreased with the introduction of U(VI). Because the sand had a low affinity for citrate, the large free citrate concentration could presumably complex the U(VI) in solution causing an increase in the aqueous conentration of U(VI). Yet, the adsorption behavior of U(VI) in the presence of citrate could not be explained solely by this argument.

Because citrate promoted the dissolution of Fe and Al from the sand, surface alteration was studied as a possible explaination of the U(VI) adsorption behavior in the presence of citrate. Surface alteration was found to be both physical (i.e., loss of surface area) and chemical (i.e., change in the chemical composition of the sand surface), with *chemical* surface alteration being the more important process for the iron-rich sand. Removal of highly reactive Fe and Al phases from the surface was found to play a determining role in the adsorption of U(VI) to the iron-rich sand in the presence of citrate.

Introduction

Heavy metal contaminants in the subsurface are often associated with low molecular weight organic complexing agents. Because of their ability to form stable aqueous complexes, organic complexing agents have been used to decontaminate nuclear reactors and nuclear facilities (Girvin et al., 1993). Therefore, some aqueous radioactive wastes contain these organic constituents along with transuranic elements (Riley and Zachara, 1992). Also, appreciable concentrations of organic complexing agents can be native to the subsurface environment (Morel and Hering, 1993).

Adsorption of heavy metals to a soil sorbent can be enhanced or reduced in the presence of organic complexing agents. Several reactions involving complexing agents can affect the adsorption of a heavy metal. These reactions include, but are not limited to, ternary complexes between the surface and a metal-ligand complex, redox phenomena, strong solution complexes between a complexing agent and a heavy metal, and surface alteration of a sorbent.

Several studies have found enhanced migration of heavy metal contaminants away from disposal facilities in the presence of complexing agents (Means et al., 1978; Olsen et al., 1986; Price and Ames, 1976; Killey et al., 1984). A number of laboratory studies have also produced similar results. Elliott and Denneny (1982) observed enhanced mobility of Co in soil columns. Azizian (1998) found a decrease in lead adsorption on a synthetic iron-coated sand with the addition of NTA. Most explanations of enhanced migration of radionuclides invoke a solution complex between heavy metals and organic complexing agents that increases the aqueous solubility of the heavy metal and alters its participation in other geochemical processes, such as adsorption or redox reactions (Brooks et al., 1996; Girvin et al., 1993).

By contrast, enhanced adsorption has also been observed. Redden et al. (1998) found almost complete adsorption of U(VI) to goethite over the entire pH range studied (3-11.5) when a large excess of citrate was present. Others have also found enhanced adsorption of heavy metals over a limited pH range (Zachara et al., 1995; Girvin et al., 1993). Preferential adsorption of a heavy metal-complexing agent species (ternary surface complex) is sometimes sited to explain enhanced adsorption.

In this study, the affect of citrate on the adsorption of U(VI) on a natural (non-synthesized) iron-rich silica sand was investigated. The sand was similar to the sand studied by Rosentreter et al. (1998). Both U(VI) and citrate are components of radioactive waste (Riley and Zachara, 1992). Measurable concentrations of citrate can be found occurring naturally in soils and appreciable concentrations of U(VI) can be found in mine drainage (Geipel et al., 1996). Understanding the affect of citrate on the adsorption of U(VI) to iron-rich materials is an important step in understanding and modeling the subsurface transport of U(VI).

As with other organic complexing agents, citrate can complicate U(VI) adsorption phenomena by increasing, decreasing, or not appreciably influencing adsorption depending on the sorbent of interest, the concentration of citrate, and the aqueous pH (Redden et al., 1998). Therefore, the affect of citrate on the adsorption of U(VI) must be known to describe transport of U(VI) when appreciable concentrations of citrate are present. If the interaction of citrate with a sorbent surface is minimal, appreciable levels of citrate can facilitate transport of metal contaminants by increasing their aqueous solubility. Citrate can also decrease transport of metals through the soil by forming metal-ligand complexes that sorb to a solid phase more strongly than non-complexed metals.

Citrate can also alter the surface of sorbent physically (e.g., loss of surface area) or chemically (e.g., change in the chemical composition of adsorbing oxide phases). This surface alteration could enhance or reduce the transport of U(VI), depending on the composition and amount of adsorbing oxide phases. The affect of surface alteration on the adsorption behavior of metals in the presence of citrate has been sparsely studied. Yet, citrate has been found to effectively extract amorphous Fe when used with ascorbate (Reyes and Torrent, 1997), and citrate promoted dissolution has been found to alter mineral surfaces by many workers (Kraemer et al., 1998; Holmen and Casey, 1996; Klewicki and Morgan, 1999).

In the present study, it was observed that the determining factor in the adsorption behavior of U(VI) on an iron-rich sand in the presence of citrate was chemical alteration of the sand surface (the extraction of the high-affinity amorphous phases Fe and Al from the sand).

Experimental

Materials

Two primary U(VI) stock solutions were prepared. A low-activity U(VI) standard (10 mM UO_2^{2+}) was prepared from analytical grade uranyl nitrate solid ($^{238}UO_2(NO_3)_2 \cdot 6H_2O$) from Fluka (Ronkonkoma, NY) by diluting with 1% HNO_3. A high-activity stock solution of 1 mM UO_2^{2+} in 1% HNO_3, with an activity of 1 mCi/mL $^{233}UO_2^{2+}$, was made from the low-activity U(VI) standard and 100 μCi $^{233}UO_2^{2+}$ (Isotope Products Laboratories, Burbank, CA). All secondary standards were diluted from the low or high-activity stock solutions depending on the method of U(VI) and citrate determination (liquid scintillation counting or ICP-MS).

A 1 µCi/mL stock solution of (1,5-^{14}C)-citrate was prepared by adding 50 µCi of (1,5-^{14}C)-citrate solution (Amersham, Arlington Hts., IL) to a 50 mL volumetric flask and diluting with distilled de-ionized water. An appropriate non-labeled citrate standard was made immediately before each adsorption experiment from 99+% pure citric acid solid (Aldrich, Milwaukee, WI). Aliquots of the (1,5-^{14}C)-citrate stock solution and the citric acid standard were added separately to the adsorption experiments. To ensure stability, citrate standards were not kept more than 1 month.

Natural sands coated with iron and aluminum oxides were collected from a location on the southern tip of the Delmarva Peninsula in Virginia, near the village of Oyster (sample BS-8). Exposed in the Oyster borrow pit are cross-stratified sands, horizontally-bedded sands, and shelly gravelly sands (DeFlaun et al. 1997). The primary mineralogy consists of quartz with varying amounts of lithic fragments and shell (replaced by secondary hydrous iron oxide). In addition, minor amounts of feldspars and dark minerals (primarily hornblende and ilmenite) are present. Secondary minerals include extensive hydrous iron oxide (ranging from 2 to 100 mmol/g Fe) and very minor clay minerals (primarily kaolinite replacing feldspars with some smectites). These sands also contained appreciable amounts of aluminum-oxide minerals. Some bulk characteristics of the iron-rich sand sample used for this study (BS-8) were determined, such as: dithionite-citrate-bicarbonate (DCB) extractable iron (4.1 µmol/g), DCB extractable Al (3.7 µmol/g), BET surface area (0.25 m^2/g) and cation exchange capacity (0.26 meq/g).

Adsorption Experiments

Experimental data were gathered in the form of pH adsorption data (represented by the fraction of analyte adsorbed as a function of the free hydrogen ion concentration) in batch. The total citrate concentrations ranged from 1-100 μM and the pH values studied ranged from 3.1 to 7.4. The concentration of U(VI) was 10 μM for all experiments.

The sand sorbent was added to a polycarbonate centrifuge tube (Tube A) along with enough 0.01 M $NaClO_4$ to produce the desired 20 g/L solids concentration. Before addition of U(VI) and citric acid, the slurry was shaken for 24 hours at 200 rpm and 25 °C, to pre-equilibrate the sand with the aqueous phase. Because oxidation of citrate has been found to occur in similar systems when exposed to visible light (Dodge and Francis, 1994), the centrifuge tubes were wrapped in dark paper and the adsorption experiment was performed in the dark (until the sand samples were freeze dried). At the end of the 24 hour period, an aliquot of a premixed U(VI)-citrate standard was added to the aqueous phase. NaOH and $HClO_4$ were used to adjust the pH to the desired value. The sample solution was shaken for 48 hours at 200 rpm and 25 °C to equilibrate the system (equilibration time was determined from U(VI)-citrate kinetics experiments; the order of addition of U(VI) or citrate did not seem to affect the adsorption kinetics). The samples were then centrifuged for 30 minutes at 10000 rpm to separate the aqueous and the solid phases. The supernatant was sampled for determination of U(VI) and/or citrate concentrations.

The supernatant was then transferred to a clean centrifuge tube so that only the wet sand remained in Tube A. The final pH of the supernatant was measured and the wet

sand was then freeze dried. The sand and Tube A were weighed before and after freeze drying to obtain the amount of water contained in the wet sand. The dry sand was then transferred to a clean, centrifuge tube (Tube B). A 20 mL aliquot of 1% HNO_3 was added to Tubes A and B to extract U(VI) from the centrifuge tube and the iron rich sands, respectively. The tubes were shaken for 48 hours at 200 rpm and 25 ^{o}C. The supernatant in tubes A and B was sampled.

If citrate was present in the adsorption experiment, a 10 mL aliquot of 0.35 M NaOH was added to Tubes A and B to extract the citric acid (pH > 11). The tubes were again shaken for 48 hours at 200 rpm and 25 ^{o}C and the supernatant was again sampled for both tubes. U(VI) and citrate concentrations were determined by mass for all adsorption experiments. At least 95% of the citrate and U(VI) added to adsorption experiments were recovered, indicating that microbial degradation is controlled in the adsorption experiment and all sources of U(VI) adsorption have been identified.

Extraction of Fe and Al from Iron-rich Sand

Four separate methods of extraction were used to alter the surface of the iron-rich sands. Dithionite-citrate-bicarbonate (DCB), Tamm's organic acid (TOA), citrate (CIT), and an aqueous solution of 0.1 M $NaClO_4$ (AQ) were used to extract the sand.

The DCB solution was prepared with 0.26 M sodium citrate, 0.11 M $NaHCO_3$, with 3.9 g dithionite added at the beginning of each extraction. TOA consisted of 0.175 M ammonium oxalate and 0.1 M oxalic acid. The CIT extractant consisted of 1 mM citrate in 0.01 M $NaClO_4$ and 0.02 M 3-[N-Morpholino]propanesulfonic acid (MOPS) zwitterionic buffer at pH 7.2. The composition of AQ was 0.01 M $NaClO_4$ and 0.02 M MOPS buffered at pH 7.2.

The extractant solution (20 mL) was added to a polycarbonate centrifuge tube along with 5.0 g sand. The sand slurry was shaken on an orbit shaker for 24 hours at 200 rpm and 25 °C for each extraction. All extractions were performed in the dark. The slurry was centrifuged at 10000 rpm for 10 minutes. The supernatant was sampled and decanted from the reaction vessel. More extractant was added to the sand and the extraction was repeated. No less than 5 extractions were completed for each extractant. After the extractions were completed the sand was washed and centrifuged five times. After washing was complete, the sand was freeze-dried in preparation for adsorption experiments on the extracted sands.

Dissolution of Fe and Al

Measurement of Fe and Al dissolution was conducted in the same manner as the adsorption experiments. The sand sorbent was added to a polycarbonate centrifuge tube along with enough 0.01 M $NaClO_4$ to produce the desired 20 g/L solids concentration. The centrifuge tubes were wrapped in dark paper and the slurry was shaken for 24 hours at 200 rpm and 25 °C. At the end of the 24 hour period, an aliquot of a citrate standard was added to the centrifuge tube for a final citrate concentration of 1, 10, or 100 μM. The pH was adjusted to the desired value. The sample solution was shaken for 48 hours at 200 rpm and 25 °C. The samples were then centrifuged for 30 minutes at approximately 10000 rpm to separate the aqueous and the solid phases. Three aliquots of the supernatant were diluted with 1% HNO_3 for simultaneous determination of Fe and Al by ICP-OES.

Analytical Methods

When citrate was present in the adsorption experiment dual liquid scintillation counting (LSC) was used to determine citrate and/or U(VI) concentrations. LSC was performed on a Beckmann LS 7800 to determine the amount of $(1,5-^{14}C)$ citrate and $^{233}UO_2^{2+}$ in aqueous samples. An aqueous 1 mL sample from the adsorption experiment was added to 10 mL of liquid scintillation fluid (LSF). The LSF used was Optifluor (Packard), with a maximum water loading of approximately 20%. A time limit of 10 minutes or a 2σ error of less than 2 was considered to be adequate for gathering a sufficient number of counts while constrained by the large number of samples to be counted. Changes in ionic strength, pH, and dissolution from the sand sorbent were found not to influence the response of LSC for $(1,5-^{14}C)$ citrate. U(VI) determination was affected by the ionic strength of the aqueous sample. Therefore, external standards were used to help correct for the response of U(VI).

Samples containing only ^{238}U(VI) were analyzed with a Fisons VG PlasmaQuad II+ ICP-MS with a concentric nebulizer, and a Gilson 221 auto-sampler for sample uptake. The mass scan was conducted in peak-jump mode with an acquisition time of 30 seconds per sample. An internal standard of 10 μg/L Bi (Bailey et al., 1993) was added directly to the samples before they were analyzed by ICP-MS. A practical detection limit of approximately 1 nM U(VI) was found for the sand/UO_2^{2+} system.

A Jovin-Yvon JY2000 ULTRATRACE inductively coupled plasma-optical emission spectrometer was used to quantify the aqueous concentrations of Fe and Al. The emission wavelengths used were 259.94 nm for Fe and 396.15 nm for Al, with practical limits of detection of approximately 6.2 μg/L (0.1 μM) and 28 μg/L (1 μM), respectively.

Results

Adsorption on Iron-rich Sand

The simultaneous adsorption of U(VI) and citrate as a function of pH is shown in Fig. 3.1. Figure 3.1a illustrates the affect of increasing concentrations of citrate on the adsorption behavior of U(VI). The adsorption of U(VI) is generally decreased with increasing concentrations of aqueous citrate. U(VI) adsorption is only slightly decreased with 1 μM citrate, while no appreciable adsorption of U(VI) occurs in the presence of 100 μM citrate. At 0-10 μM citrate, citrate seems to have no effect on the adsorption behavior of U(VI) below a pH of 5.5, but decreases U(VI) adsorption at pH 5.5-7. Also, at equimolar concentrations of U(VI) and citrate (10 μM), the concentration of U(VI) adsorbed is generally unaffected by hydrogen ion concentration from pH 6-7.

Very little citrate adsorption was observed in the presence of U(VI), with the greatest fraction adsorbed at 1 μM citrate and no adsorption at 100 μM citrate (Fig. 3.1b). The adsorption of citrate seems to be relatively unaffected by change of solution pH.

Figure 3.2 shows citrate adsorption on the iron-rich sand over a range of pH values and citrate concentrations. Little adsorption of citrate was observed at 10 and 100 μM. At 1 μM citrate, the percent adsorbed does reach 85-90%. As with citrate adsorption in the presence of U(VI), the aqueous pH had little effect on the adsorption of citrate at 10 and 100 μM.
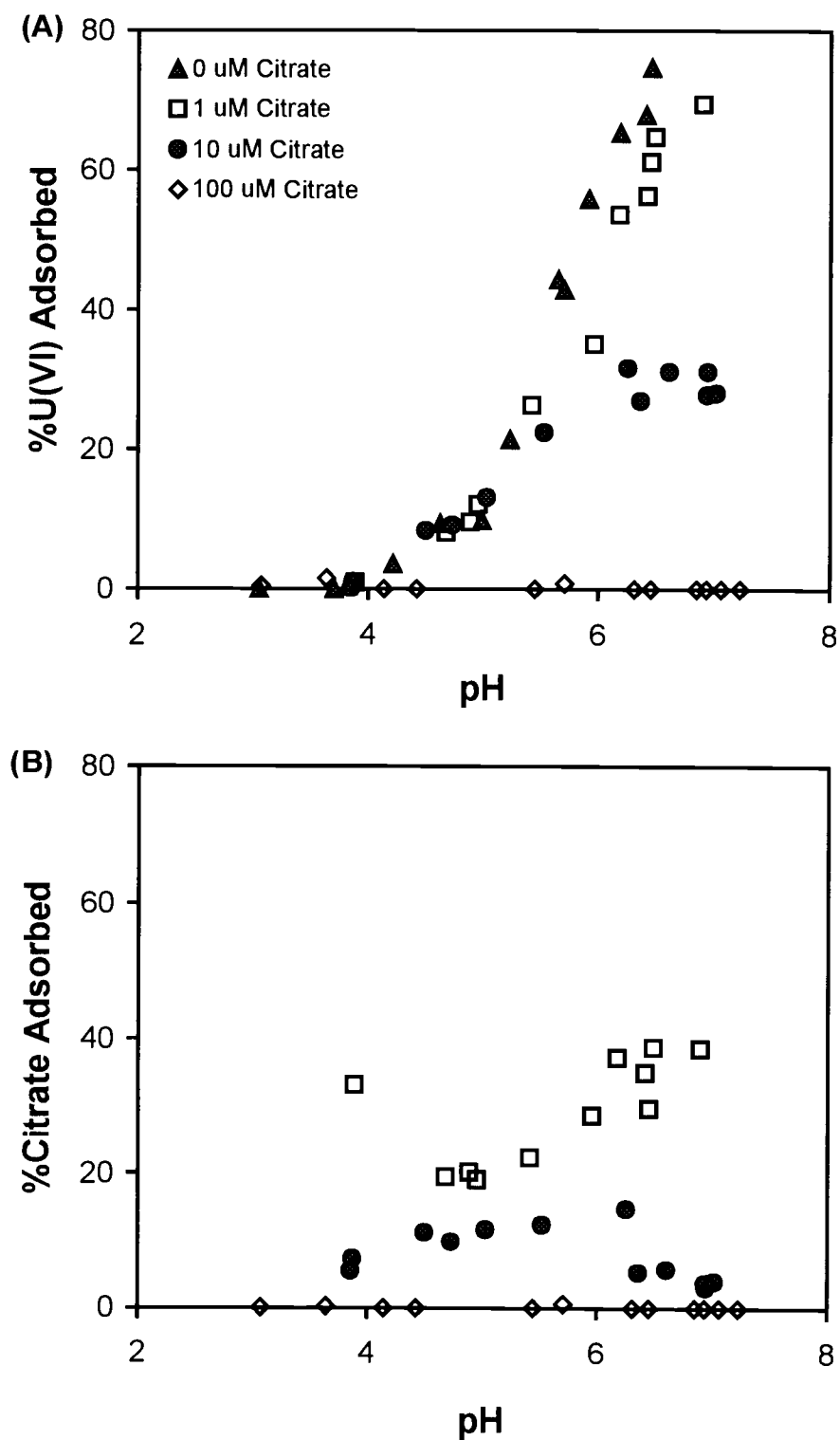
Figure 3.1. Adsorption data for the U(VI)/citrate/iron-rich sand system. 20 g/L sand BS-8, 0.01 M $NaClO_4$, open to atmospheric CO_2, and 10 μM U(VI). A) U(VI) adsorption in the presence of citrate. B) Citrate adsorption in the presence of U(VI).
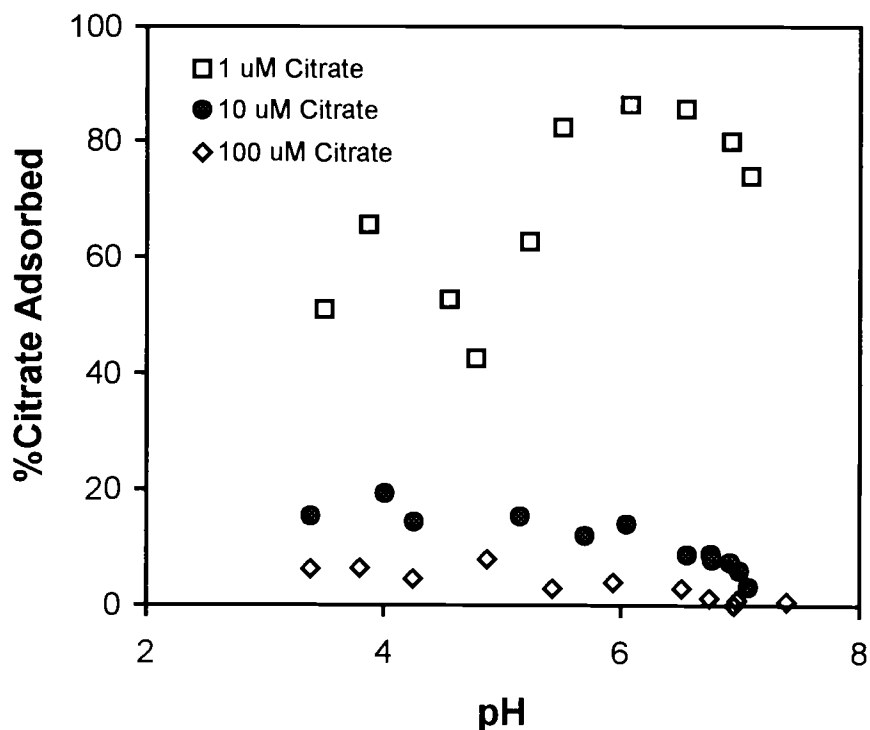
Figure 3.2. The fraction of citrate adsorbed on natural iron-rich sand. 20 g/L sand sample BS-8, 0.01 M $NaClO_4$, open to atmospheric CO_2.

Fe and Al Dissolution

The aqueous concentration of Fe at 0-100 μM citrate was determined as a function of pH (Fig. 3.3a). At 0 and 1 μM citrate the aqueous iron concentration decreased to pH 4.5 where the approximate detection limit of the ICP-OES is reached. At 10 and 100 μM citrate, the dissolution behavior of iron at low pH is similar to the dissolution behavior at 0 and 1 μM citrate. Above a particular pH value, the aqueous concentration of Fe increases with increasing pH values (pH 5 for 10 μM citrate and pH 4 for 100 μM citrate). At 100 μM citrate, the aqueous Fe concentration levels off at approximately 1 μM. This behavior may be caused by solubilization of all of the readily
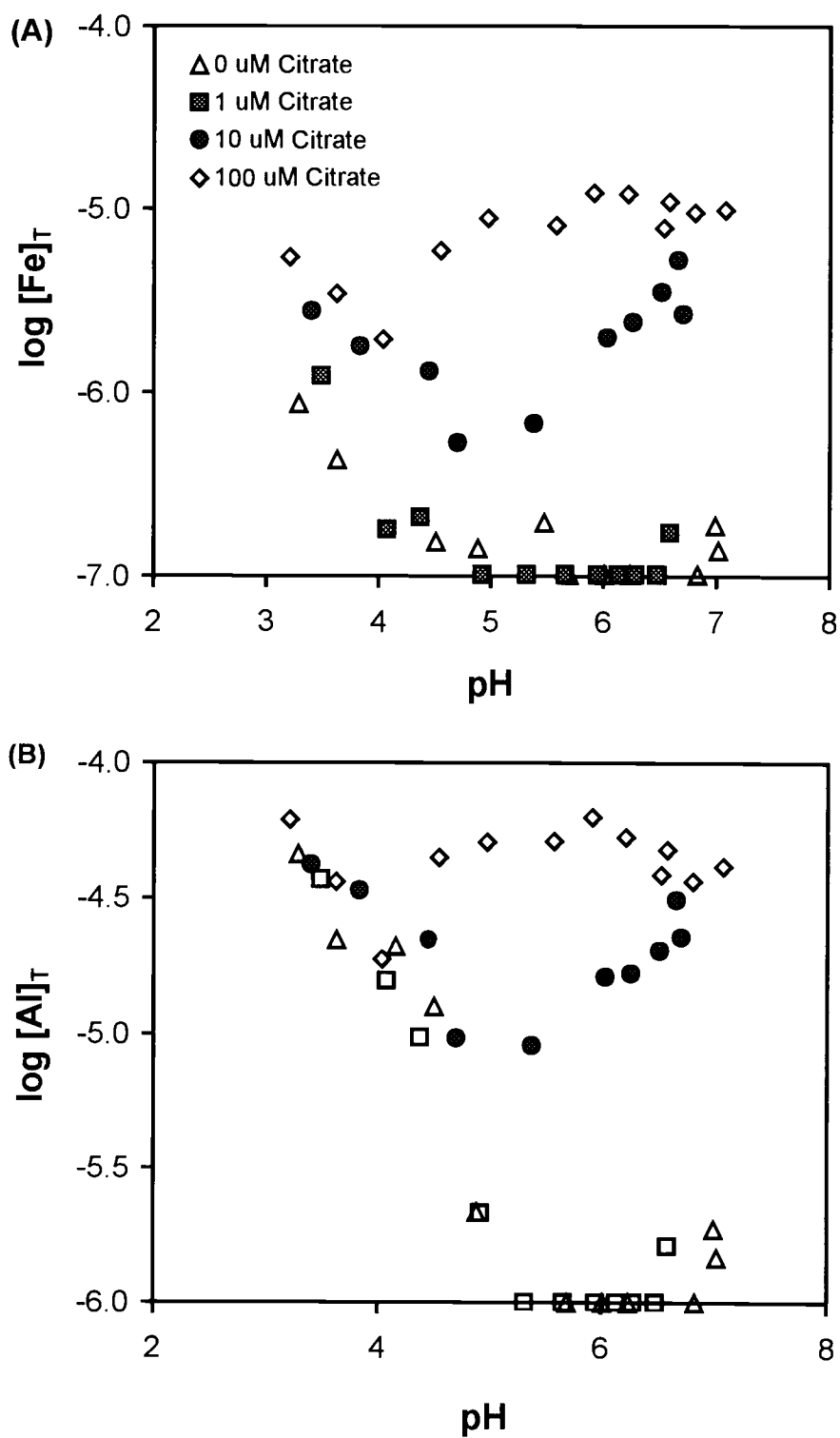
Figure 3.3. Concentration of dissolved of Fe and Al from an iron-rich sand as a function of pH. 20 g/L sand sample BS-8, 0.01 M $NaClO_4$, open to atmospheric CO_2. A) Dissolution of Fe in the presence of 0-100 μM citrate. B) Dissolution of Al in the presence of 0-100 μM citrate.

available (amorphous) Fe. The largest amount of Fe released from the sand was approximately 89 nmol/g which was 2.2% of the DCB extractable iron.

The qualitative behavior of the Al with increasing concentrations of citrate is the same as Fe (Fig. 3.3b) with the total aqueous concentration of Al being approximately an order of magnitude higher than the aqueous concentration of Fe at the same pH value. The largest amount of Al released from the sand was approximately 280 nmol/g which was approximately 7% of the DCB extractable aluminum.

Surface Alteration

Alteration of the iron-rich sand was probed in three ways: 1) determination of extractable concentrations of iron and aluminum by a number of extraction techniques, 2) determination of the surface area of the extracted sands, and 3) adsorption of U(VI) to the extracted sands. Figure 3.4 shows the amount of iron and aluminum extracted from the iron-rich sand, and the correlation of extractable iron and aluminum with the surface area of the sand. As shown in Fig. 3.4a, the DCB extractable iron and aluminum concentrations, which represent the total extractable iron and aluminum in the sand, were almost 4 μmol/g. The extraction of the sand with TOA, which represents the amorphous iron and aluminum phases, extracted approximately 10% of the DCB extractable iron and aluminum. CIT extraction was comparable to TOA for aluminum, but less iron was extracted with CIT than with TOA.

Figure 3.4a also illustrates a strong correlation between the extracted iron and aluminum and the percent decrease in surface area (ρ) from the sand extracted with AQ. Figure 3.4b illustrates the correlation between the surface area and the extractable iron
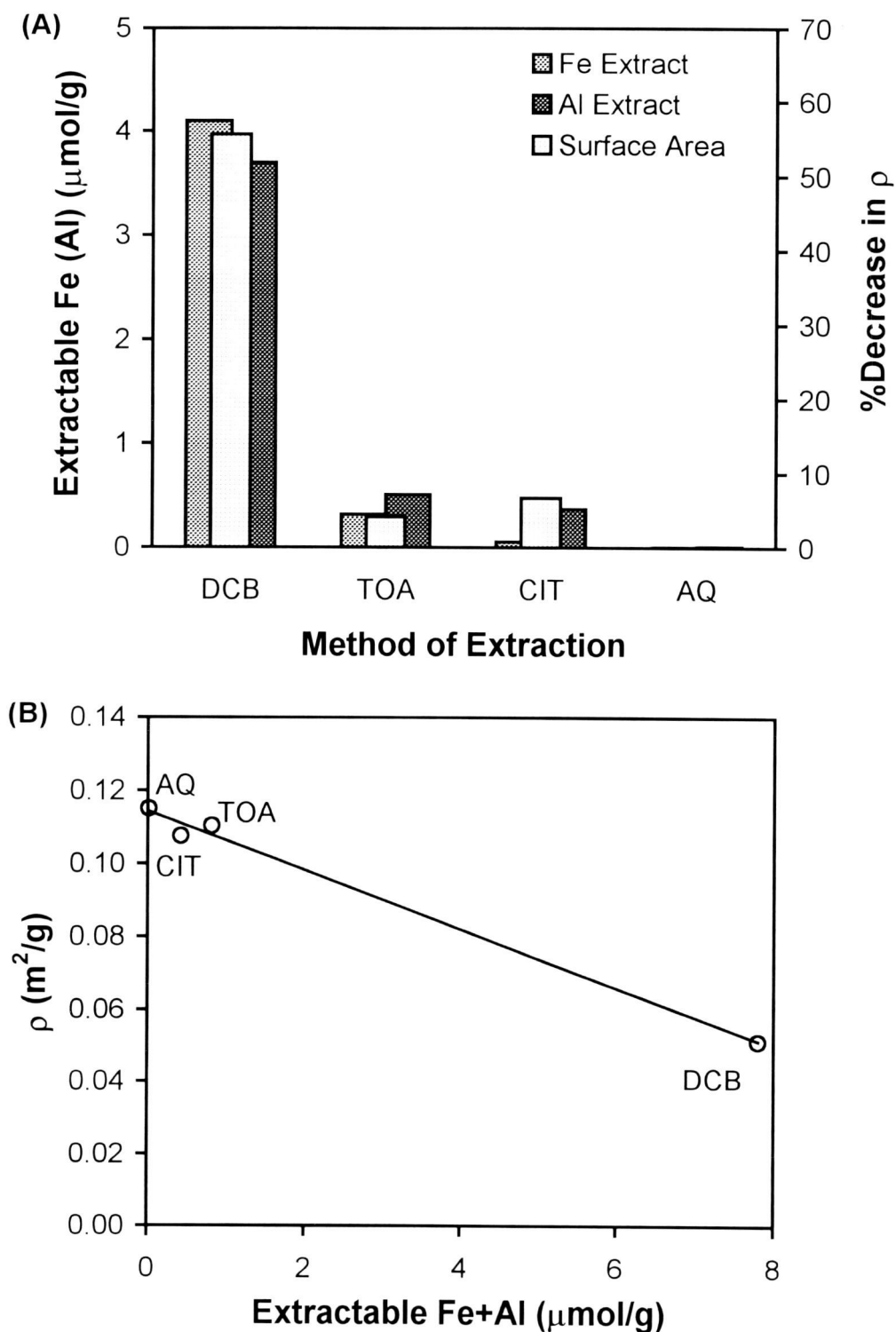
Figure 3.4. Physical and chemical properties of sand extracted with a variety of techniques. A) Concentration of Fe and Al extracted from the iron-rich sands by each extraction technique and the correlation with a decrease in the bulk surface area (ρ). B) Linear correlation of the sum of the extractable Fe and Al and the surface area of the extracted sand.

and aluminum is linear. The surface area of the sand decreases linearly as the extraction technique removes more iron and aluminum from the sand. Linear regressions that included either iron or aluminum as independent variables resulted in fairly linear but poorer fits than the one in Fig. 3.4b.

Figure 3.5 represents the adsorption of U(VI) on iron-rich sand which was previously treated with the three extractants: CIT, TOA, and DCB. No U(VI) adsorption was observed on the sand which was extracted with DCB solution. The sand extracted with TOA exhibited little affinity for the U(VI) at pH values below 5.5. Above this pH, the percent U(VI) adsorbed increased to 12%. The absolute affinity of CIT extracted sand for U(VI) was comparable to the TOA extracted sand. The percent U(VI) adsorbed increased from pH 4.5-5.25, and then remained constant from pH 5.25-6.5.

Data from Figs. 3.1a and 3.5a were used to compare the adsorption of U(VI) when it was added simultaneously with citrate and when the sand was previously extracted with CIT solution. The adsorption behavior (i.e. qualitative shapes of the adsorption edges) of U(VI) for both cases is very similar, with the maximum amount of U(VI) adsorbed being greater for simultaneous adsorption of 10 μM citrate and U(VI).
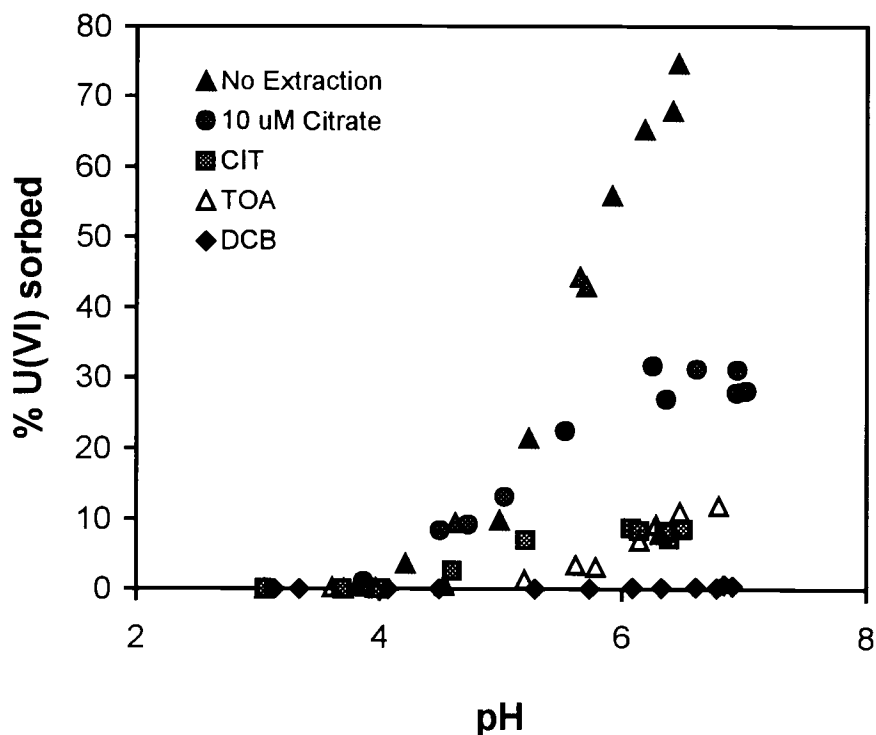
Figure 3.5. U(VI) adsorption on sands extracted with a variety of extraction solutions. 20 g/L sand sample BS-8, 0.01 M $NaClO_4$, open to atmospheric CO_2. Comparison of U(VI) adsorption on sand extracted with DCB, TOA, CIT and a sand that was not previously extracted.

Discussion

Adsorption on Iron-rich Sand

U(VI) adsorption data obtained for the natural sand sample had the same general characteristics as the adsorption data gathered by others working with iron-rich minerals (Hsi and Langmuir, 1985; Payne et al., 1996; Waite et al., 1994; Redden et al., 1998). Only one adsorption edge is shown in Fig. 3.1a at 10 μM U(VI). Other adsorption data were gathered but are not show. First, the pH adsorption edges occurred over one to two pH units and were relatively smooth. Second, as the aqueous U(VI) concentration increased the fraction of U(VI) adsorbed decreased at a particular aqueous pH. Third, the

fraction of U(VI) sorbed at a given pH increased with sands that contained more DCB extractable Fe. This observation is in agreement with the findings of Rosentretter et al. (1998), who found a positive linear correlation between K_D and the sum of the DCB extractable iron and aluminum when studying U(VI) adsorption on similar iron-rich sands.

The adsorption of citrate on the iron-rich sand samples (Fig. 3.2) seems to be inconsistent with adsorption of anions by synthetic iron oxides (Redden et al., 1998; Raven et al. 1998; Geelhoed et al., 1997). First, over the pH range where anionic ligands should be most strongly associated with a sorbent, the citrate has a very low adsorption density. The citrate concentration has to be below 10 μM before the fraction of citrate adsorbed is above 20%. Second, the adsorption of anions on sorbent surfaces as a function of pH does not usually contain adsorption maxima (1 μM citrate). The presence of two adsorption maxima at 1 μM citrate could be an experimental artifact, stemming from the low concentration of citrate used and the difficulty in quantifying citrate at low concentrations. We feel that this is not likely because of the non-erratic nature of the data and because quantification of citrate by LSC was studied under a variety of conditions to ensure accurate determination of low concentrations of aqueous citrate. A more likely explanation is that a dissolution-adsorption equilibrium exists, in which the adsorption of citrate corresponds to iron and aluminum dissolution. This explanation is supported by comparison of Fig. 3.2 (1 μM citrate) to Fig. 3.3a (10 and 100 μM citrate). Note that at pH 5 the aqueous concentration of citrate is at its highest (1 μM citrate, Fig. 3.2) and the dissolved concentration of iron is at its lowest (10 μM citrate, Fig. 3.3a). This qualitatively agrees with the simple model of ligand-promoted dissolution, in which the

dissolution rate of a mineral due to a specific ligand is proportional to the adsorbed

concentration of that ligand (Kraemer et al., 1998). The adsorption maxima in Fig. 3.2

may be also be present for 10 and 100 μM citrate, the presence of these maxima cannot

be confirmed because of the small fraction of citrate adsorbed on the sand at these citrate

concentrations.

At pH values greater than 5.5 the adsorption of U(VI) decreases with increasing

aqueous citrate concentrations (Fig. 3.1a). Comparison of Fig. 3.1b to Fig. 3.2 shows that

the adsorbed concentration of citrate at a particular pH value also decreases when U(VI)

is present in solution. This adsorption behavior could be explained by competition of

citrate and U(VI) adsorption sites on the iron-rich sand or a strong aqueous complex

between U(VI) and citrate in this pH range. The adsorption behavior of U(VI) and citrate

at 100 μM citrate indicates that U(VI) and citrate are not competing for adsorption sites

on the surface of the sand. If competition of U(VI) and citrate for adsorption sites were

very important, either U(VI) or citrate would be adsorbed in some appreciable amount,

thereby covering the active adsorption sites. Yet, no adsorption occurs for either citrate of

U(VI) over the entire pH range. Therefore, the adsorption behavior of citrate in the

presence of U(VI) is not consistent with competition by U(VI) and citrate for adsorption

sites.

With no evidence for competition, the adsorption behavior of U(VI) and citrate

suggest a strong U(VI)-citrate solution complex may be integral in decreasing the

adsorption of U(VI) in the presence of citrate. Yet, the known aqueous complexes of

citrate with U(VI) tend to be strongest at pH values below 6 and the concentration of

these complexes rapidly decreases in solution as the aqueous pH increases (under these

conditions). This may suggest surface alteration is the mechanism responsible for the adsorption behavior of U(VI) (discussed below).

Fe and Al Dissolution

The dissolution of iron and aluminum from the sand is an important process that is promoted by complexing agents. This dissolution can alter the solution *and* surface chemistry of the system. As seen in Fig. 3.3, the dissolution behavior of iron and aluminum in the presence of citrate is very similar. The dissolution behavior of iron and aluminum at 0-1 μM citrate is indicative of a solution saturated with a solid. Thermodynamic calculations for a variety of pure crystalline iron and aluminum phases were completed, with ferrihydrite most closely resembling the experimental iron dissolution from the sand at without citrate. The dissolution behavior of the sand is consistent with a previous modeling study of iron-rich sand by Logue et al. (2000), in which adsorption of U(VI) to the iron-rich sand was predicted reasonably well by a surface complexation model calibrated for a synthetic ferrihydrite (Waite et al., 1994). A number of thermodynamic calculations of dissolution of pure phase aluminum minerals failed to adequately describe the dissolution of Al from the sand (without citrate).

At higher concentrations of citrate, the dissolution of iron and aluminum increases at the higher pH values. The increased concentration at high pH indicates that iron and aluminum are strongly interacting with the citrate in solution or on the surface. At 100 μM citrate, the aqueous iron and aluminum concentrations become fairly constant above pH 5. This behavior may be caused by solubilization of all of the readily available iron and aluminum. If some readily available amorphous phases of iron and aluminum are

present in the sand, the citrate may be able to dissolve only amorphous phases and not more crystalline phases. The higher aqueous concentration of aluminum at a particular pH indicates that the mixed phases of aluminum are much more vulnerable to leaching by the citrate than solid iron phases.

Because the iron and aluminum concentrations extracted with citrate were appreciable (Fig. 3.3), dissolution of the sand surface (surface alteration) must be considered when explaining U(VI) adsorption behavior in the presence of citrate.

Surface Alteration

Figure 3.4 supports the strong correlation between extractable iron and aluminum and the surface area of iron-rich sands found by Rosentretter et al. (1998). The correlation between extracted concentrations of iron and aluminum and the surface area of the sand proves that physical surface alteration by citrate does occur, but doesn't give strong support to physical surface alteration as a means to justify the large decrease in U(VI) adsorption seen in Fig. 3.1a. The slight decrease in surface area for the sand extracted with CIT (Fig. 3.4a) does not account for the decrease in U(VI) adsorption, considering that at 100 μM citrate no U(VI) adsorbed to the sand over the entire pH range (Fig. 4.1a). Yet, comparison of CIT and TOA extracted Fe and Al (Fig. 4.4a) demonstrates that CIT is an effective extractant of the amorphous phases of aluminum and to a lesser degree iron. If the interaction of U(VI) with amorphous phases of iron and aluminum is responsible for its adsorption behavior, the extraction of these small amounts of iron and aluminum could still have a great affect on the adsorption properties of U(VI).

Figure 3.5 conclusively shows that surface alteration is a major factor affecting the adsorption behavior of U(VI) on the iron-rich sand in the presence of citrate. Figure 3.5 illustrates that a sand previously extracted with CIT has little affinity for U(VI). This suggests that CIT extracts the majority of the reactive surface sites of iron and aluminum, which decreases the affinity of the sand for U(VI). The difference in the U(VI) adsorption behavior between TOA and CIT at pH 4.5-6 can be explained by the difference in the amount of iron that TOA and CIT extracted (Fig 3.4a). TOA extracts more of the iron from the surface of the sand, causing less U(VI) to adsorb in this pH range. Because the Al extracted by TOA and CIT is comparable, the aluminum on the surface should be approximately the same. Therefore, if aluminum where the important solid phase in this pH range, the adsorption behavior of U(VI) on TOA and CIT extracted sands would be expected to be similar. This is not the case, which would suggest that at lower pH values the iron on the surface is much more important to the adsorption of U(VI) than other components of the sand. Also, at pH 6-7 the amount of U(VI) adsorbed on TOA and CIT extracted sands is approximately the same. Similar adsorption of U(VI) for these two sands suggests that Al may be the reactive surface phase at these higher pH values.

When evaluating Fig. 3.4a and 3.5 together, it appears that there are different levels of reactivity for the active iron phases. Little iron is extracted by CIT (Fig. 3.4a), yet the decrease in U(VI) adsorption is dramatic for CIT extracted sand as compared with adsorption of U(VI) by non-extracted iron-rich sand. Because of the dramatic decrease in U(VI) adsorption with CIT extracted sand, it can be inferred that the most readily extractable iron has the highest affinity for U(VI). TOA extracts only 10% of the total

DCB extractable iron, yet there is no adsorption of U(VI) below an aqueous pH of 5.25 and only 12% of the U(VI) adsorbs at the highest pH studied. The difference between the adsorption of U(VI) on CIT and TOA extracted sands may indicate that there is another level of reactivity for surface Fe that is extracted by TOA but not extracted by CIT. Looking even further, a third level of reactive surface can be inferred when comparing U(VI) adsorption on TOA and DCB extracted sand. Some adsorption of U(VI) is apparent on TOA extracted sands, but no U(VI) adsorption occurs after extraction with DCB. Because the TOA solution extracts only 10% of the DCB extracted Fe and Al, it was found that most of the iron and aluminum phases (90% of the DCB extractable Fe and Al) show little affinity for U(VI), and a very small amount of these phases are responsible for the majority of the U(VI) adsorption. These observations support at least three levels of reactivity for the iron-rich sand, which would have important implications to surface complexation modeling of heterogeneous environmental sorbents. Differential levels of reactivity for the iron-rich sand for U(VI) lends support to the argument that the surface of heterogeneous materials cannot be represented accurately with only one surface site and must be viewed as having multiple surface sites with variable reactivity.

In Figure 3.5, the qualitative adsorption behavior of U(VI) on the iron-rich sand after extraction of the sand with CIT solution and in the presence of citrate (10 μM) are similar. The adsorption of U(VI) increases with increasing pH up to a certain pH value and then becomes constant over the rest of the pH range. Also, the pH range where the maximum U(VI) adsorption occurs is approximately the same for both adsorption edges. If a less concentrated CIT solution was used to extract the sand, the absolute adsorption of U(VI) on the extracted sand may have been much closer to the adsorption of U(VI) in

the presence of citrate. The qualitatively similar adsorption behavior for these two edges supports the conclusion that surface alteration can be used to explain the adsorption behavior of U(VI) on iron-rich sand in the presence of citrate.

Quantitative Model

We have attempted to quantitatively model this system by building on the initial model for U(VI) adsorption on these sands from Logue et al. (2000). Attempts to quantitatively model the data presented in this study have failed to adequately describe the adsorption behavior of U(VI) in the presence of citrate. It is not surprising that current methods of modeling, embodied by FITEQL 4.0 (Herbelin and Westall, 1999), where not adequate to model the experimental data. A non-static adsorbing surface, the presence of three levels of reactivity, changing physical characteristics of the sand, and adsorption of U(VI) to a surface with simultaneous dissolution of the surface, all lend to the complexity of this system and the difficulty in describing experimental data.

Conclusions

Surface alteration of natural iron-rich sands was studied as a possible explaination for the adsorption behavior of U(VI) on natural iron-rich sands. Surface alteration by citrate extraction changes the chemical reactivity and the bulk physical properties of the sorbent. Alteration of the chemical composition of the surface was found to be the determining factor in the adsorption of U(VI). As more iron and aluminum were extracted from the sand, the U(VI) adsorption capacity of the sand decreased.

Soil washing remediation schemes (i.e., "pump and treat" methods) could be greatly affected if surface alteration was the important mode affecting contaminant

adsorption. It has been suggested that complexing agents be used to enhance the solubility of metals, therefore decreasing the time necessary to "treat" a soil. If surface alteration were a major mechanism in release of contaminant metals, instead of using a complexing agent with high affinity for the target contaminant, one would use the complexing agents with the best ability to remove the reactive surface. Also, the amount of reactive surface (e.g., iron and aluminum oxides in the soil) would determine the concentration of organic complexing agent and the length of treatment necessary to extract contaminants from a soil.

Another important finding of this study was experimental evidence for at least three levels of reactivity of the sorbent for U(VI). Evidence for an extremely reactive phase of iron that can be extracted by citrate was found. Without this reactive surface phase the adsorption of U(VI) dramatically decreases. Two other levels of reactivity of the sand were indicated by different U(VI) adsorption affinities when the sand was extracted with different solutions (DCB and TOA). These observations support the use of multiple reactivity sites for surface complexation modeling of heavy metal adsorption (e.g. strong and weak site types).

Acknowledgments

References

Azizian M. F. and Nelson P. O. (1998) Lead Sorption, Chemically Enhanced Desorption, and Equilibrium Modeling in an Iron-Oxide-Coated Sand and Synthetic Groundwater System. In *Adsorption of Metals by Geomedia* (ed. E.A. Jenne), Chap. 6, pp. 165-180. Academic Press.

Bailey E. H., Kemp A. J., and Ragnarsdottir K. V. (1993) Determination of Uranium and Thorium in Basalts and Uranium in Aqueous Solution by Inductively Coupled Plasma Mass Spectrometry. *J. Anal. At. Spectrom.* **8**, 551-556.

Brooks S. C., Taylor D. L., and Jardine P. M. (1996) Reactive Transport of EDTA-Complexed Cobalt in the Presence of Ferrihydrite. *Geochim. Cosmochim. Acta* **60**, 1899-1908.

Brunauer S., Emmett P. H., and Teller E. (1938) Adsorption of Gases in Multimolecular Layers. *J. Am. Chem. Soc.* **60**, 309-319.

DeFlaun M. F., Murray C. J., Holben W., Scheibe T., Mills A., Griffin T., Majer E., Wilson, J. L. (1997) Preliminary observation on bacterial transport in a coastal plain aquifer. FEMS *Microbiol. Review* **20**, 473-487.

Elliott H. A. and Denney C. M. (1982) Surface Ionization and Complexation at the Oxide/Water Interface. 3. Adsorption of Anions. *J. Colloid Interface Sci.* **74**, 32-43.

Geelhoed J. S., Hiemstra T., and Van Riemsdijk W. H. (1997) Phosphate and Sulfate Adsorption on Goethite: Single anion and Competitive Adsorption. *Geochim. Cosmochim. Acta* **61**, 2389-2396.

Geipel G., Bernhard G., Brendler V., and Nitsche H. (1996) Sorption of Uranium(VI) on Rock Material of a Mine Tailing Pile: Solution Speciation by Fluorescence Spectroscopy. *Radiochim. Acta* **74**, 235-238.

Girvin D. C., Gassman P. L., and Bolton H. (1993) Adsorption of Aqueous Cobalt Ethylenediaminetetraacetate by δ–Al_2O_3. *Soil Sci. Soc. Am. J.* **57**, 47-57.

Herbelin A. L. and Westall J. C. (1999) *FITEQL: A Computer Program for Determination of Chemical Equilibrium Constants from Experimental Data, Version 4.0.* Chemistry Department, Oregon State Univ.

Holmen B. A. and Casey W. H. (1996) Hydroxamate Ligands, Surface Chemistry, and the Mechanism of Ligand-Promoted Dissolution of Goethite [α-FeOOH(s)]. *Geochim. Cosmochim. Acta* **60**, 4403-4416.

Hsi C. D. and Langmuir D. (1985) Adsorption of Uranyl onto Ferric Oxyhydroxides: Application of the Surface Complexation Site-binding Model. *Geochim. Cosmochim. Acta* **49**, 1931-1941.

Killey R.W., McHugh J. O., Champ D. R., Cooper E. L., and Young J. L. (1984) Subsurface Cobalt-60 Migration from a Low-level Waste Disposal Site. *Environ. Sci. Technol.* **18**, 148-157.

Klewiki J. K. and Morgan J. J. (1999) Dissolution of β-MnOOH particles by ligands: Pyrophosphate, Ethylenediaminetetraacetate, and Citrate. *Geochim. Cosmochim. Acta* **63**, 3017-3024.

Kraemer S. M., Chiu V. Q., and Hering J. G. (1998) Influence of pH and Competitive Adsorption on the Kinetics of Ligand-Promoted Dissolution of Aluminum Oxide. *Environ. Sci. Technol.* **32**, 2876-2822.

Logue B. A., Westall J. C., and Smith R. W. (2000) U(VI) Adsorption on Natural Iron Coated Sands: Comparison of Surface Complexation Approaches to Modeling Adsorption on Heterogeneous Environmental Materials. In preparation.

Means J. L., Crerar D. A., and Duguid J. O. (1978) Migration of radionuclide wastes: Radionuclide Mobilization by Complexing Agents. *Science (Washington, DC)* **200**, 1477-1486.

Morel, F. M. M. and Hering, J. G. (1993) *Principles and Applications of Aquatic Chemistry.* John Wiley.

Olsen C. R., Lowry P. D., Lee S. Y., Larsen I. L., and Cutshall N. H. (1986) Geochemical and Environmental Processes Affecting Radionuclide Migration from a Formerly Used Seepage Trench. *Geochim. Cosmochim. Acta* **50**, 593-607.

Payne T. E., Davis J. A., and Waite T. D. (1996) Uranium Adsorption on Ferrihydrite – Effects of Phosphate and Humic Acid. *Radiochim. Acta* **74**, 239-243.

Price S. M. and Ames L. L. (1976) Transuranium Nuclides in the Environment. Publication SM-199/87, Int. Atomic Energy Agency.

Raven K. P., Jain A., and Loeppert R. H. (1998) Arsenite and Arsenate Adsorption on Ferrihydrite: Kinetics, Equilibrium, and Adsorption Envelopes. *Environ. Sci. Technol.* **32**, 344-349.

Redden G., Li J., and Leckie J. (1998) Adsorption of Uranium (VI) and citric acid on Goethite, Gibbsite, and Kaolinite: Comparing Results for Binary and Ternary Systems. In *Adsorption of Metals by Geomedia* (ed. E.A. Jenne), Chap. 13, pp. 291-315. Academic Press.

Reyes I. and Torrent J. (1997) Citrate-Ascorbate as a Highly Selective Extractant for Poorly Crystalline Iron Oxides. *Soil Sci. Soc. Am. J.* **61**, 1647-1654.

Riley R. G. and Zachara J. M. (1992) Chemical Contaminants on DOE lands and Selection of Contaminant Mixturesfor Subsurface Science Research. U.S. Department of Energy, Washington DC.

Rosentretter J. R., Quarder H. S., Smith R. W., and McLing T. (1998) Uranium Sorption onto Natural Sands as a Function of Sediment Characteristics and Solution pH. In *Adsorption of Metals by Geomedia* (ed. E.A. Jenne), Chap. 7, pp. 181-192. Academic Press.

Waite T. D., Davis J. A., Payne T. E., Waychunas G. A., and Xu N. (1994) Uranium(VI) Adsorption to Ferrihydrite: Application of a Surface Complexation Model. *Geochim. Cosmochim. Acta* **58**, 5465-5478.

Zachara J. M., Gassman P. L., Smith S. C., and Tayler, D. (1995) Oxidation and adsorption of $Co(II)EDTA^{2-}$ complexes in subsurface materials with iron and manganese oxide grain coatings. *Geochim. Cosmochim. Acta* **59**, 4449-4463.

Chapter 4: Kinetics of Reduction of Nitrobenzene and Carbon Tetrachloride at an Iron-Oxide Coated Gold Electrode

Brian A. Logue[1], Paul G. Tratnyek[2], and John C. Westall[1]*

[1]Department of Chemistry
Oregon State University
Corvallis, OR 97331-4003

[2]Department of Environmental Science and Engineering
Oregon Graduate Institute of Science and Technology
P.O. Box 91000, Portland, OR 97291-1000

*Corresponding Author, Email: westallj@chem.orst.edu

Abstract

The rates of reduction of carbon tetrachloride (CT) and nitrobenzene (NB) by iron-oxide coated gold electrodes were studied to gain insight into the processes that control reduction of groundwater contaminants by zero-valent iron permeable reactive barriers. Fe(III)-oxide films were deposited on gold electrodes, and Fe(II) sites were introduced into the films by controlled electrochemical reduction of a small fraction of the Fe(III) in the oxide film. Mass transport kinetics were controlled through use of a well-defined flow-through system similar to a wall-jet electrode. The factors affecting the overall reduction rate were investigated by varying the Fe(II) content in the iron-oxide, controlling the mass transport of electroactive species to the oxide surface, and varying the thickness of the oxide film.

The rates of reduction of CT and NB were found to be independent of Fe(II) content in the iron-oxide and were only slightly dependent on the rate of transport to the surface of the oxide under a few sets of reaction conditions. Conversely, the rates of reduction were greatly dependent on the thickness of the oxide film, with the reduction rate decreasing as the oxide thickness increased. Evidence also suggests that the location of the reduction reaction for CT and NB is at the gold surface. The results from this study support the view that the oxide film acts as a barrier, inhibiting direct contact between the gold electrode and the electroactive species, increasing the diffusion path length, and creating sites for adsorption of electroactive species.

Introduction

The use of zero-valent metals as a medium for permeable reactive barriers (PRB) for *in-situ* remediation of aquifers has produced encouraging results. Laboratory and field

studies have been conducted to help understand the chemistry of the PRB system

(Tratnyek, 1996), with the rate of electroactive contaminant degradation on zero-valent

iron garnering the most focus (Johnson et al., 1996; Agrawal and Tratnyek, 1996; Sayles

et al., 1997). Understanding what controls the rate of reduction of electroactive species in

PRBs is of considerable importance, because it has direct bearing on the design and

implementation of PRBs. When attempting to quantify the kinetics of reduction by zero-

valent iron, most workers have used bulk techniques, such as column or batch reaction

systems, with no control over the formation of oxide coatings on the zero-valent iron

(Sayles et al., 1997; Johnson and Tratnyek, 1994; Agrawal and Tratnyek, 1996). An

important next step in understanding the factors affecting rates of reduction is to separate

the underlying processes of reduction by zero-valent iron and quantify them (i.e.

adsorption of the electroactive species, mass transport limited degradation, growth of an

oxide-film). Some studies have been conducted to further this understanding. Scherer et

al. (1997) found the rate of carbon tetrachloride (CT) reduction on an oxide-free iron

electrode was limited by the transfer of electrons from the zero-valent iron to the CT, and

that the transport of CT to the surface of a rotating disk electrode did not significantly

affect the overall rate of reduction (pH 8.4 borate buffer, rotation rate: 100-3600 rpm,

$k_{obs} = 2.3x10^{-5}$ cm s^{-1}). Li and Farrell's (2000) findings also support direct electron

transfer as the mechanism of CT reduction on iron and iron-Pd electrodes. Klausen et al.

(1995) found that the rate of reduction for a host nitro-aromatic compounds was

catalyzed by the interaction between Fe(II) and iron-oxide surfaces. Others have also

found that iron oxides catalyze reduction by Fe(II) (Seaman et al., 1999; Sørenson and

Thorling, 1991; Liger et al., 1999). Stratmann and Müller (1994) determined that the rate

of molecular oxygen reduction was almost linearly dependent on the fraction of Fe(II) in an Fe(III)-oxide.

Even with the large body of recent research, there are still issues that limit progress toward a comprehensive understanding of the factors affecting the degradation rate of contaminants in zero-valent iron PRBs. There is uncertainty as to how the presence of an oxide film affects the reduction rate of electroactive species. The relationship between the Fe(II) content of an oxide and the reduction rate is not well understood, even though work has been initiated in this area (Stratmann and Müller, 1994, Klausen et al., 1995). There is also uncertainty as to what fundamental factor is more important in reduction at an iron-oxide surface: the transport of the electroactive species to the site of the reaction or the chemical reaction itself. Even more specifically, if the transport of an electroactive species to a reaction site is important, is transport through the pores of an oxide more important than transport to the surface of an oxide. All of these issues are of great importance in identifying promising enhancements to full-scale PRB remediation techniques.

In the current study, we have attempted to address two fundamental questions: where is the location of the reduction reaction (i.e., at the surface of the oxide film, within the oxide, or at the surface of the gold electrode) and what limits the rates of reduction of CT and NB (i.e., transport to the surface of the oxide, transport through the oxide film, or the rate of electron transfer to CT and NB). These questions were addressed by studying the reduction of NB and CT in a well-defined flow-through system approximating a wall-jet electrode configuration, which employed an iron-oxide coated gold electrode. The factors affecting the overall reduction rate were investigated by varying the Fe(II) content

in the iron-oxide, controlling the mass transport of chemicals to the oxide surface, and

varying the thickness of the oxide film. The results from this study indicate that the

location of reduction is at the surface of the gold electrode, and that transport of NB and

CT through the oxide film controls the observed rates of reduction. The effect of the

oxide on the rate of CT and NB reduction, can best be described with a physical barrier

model, where the iron-oxide decreases the rate of transport of CT and NB to the electrode

surface and reduces the reactive area of the electrode.

Experimental

Because of the extreme redox sensitivity of Fe(II) to oxygen at the elevated

aqueous pH values that were used in this study, all work with Fe(II) was done inside an

anaerobic glove box with a 5% H_2/95% N_2 atmosphere circulated over a palladium

catalyst. A methylene blue indicator was used to monitor O_2 concentrations inside the

glove box. All aqueous solvents (e.g., borate buffer solutions) were scrubbed for residual

O_2 by bubbling with N_2, which was initially passed through a high capacity oxygen trap

and an indicating oxygen trap.

Oxide Synthesis and Characterization

An Fe(III)-oxide was synthesized on a gold electrode by modifying the method

outlined by Stratmann and Müller (1994). Iron was electrodeposited from 0.2 M ferrous

ammonium sulfate (FAS) which had been previously purged with N_2. The pH was

elevated by slowly adding ammonium hydroxide to the FAS solution until an aqueous pH

of 7.5 was reached. The iron was potentiostatically electrodeposited at a potential of −140

mV (vs. SHE) and increased to +200 mV (vs. SHE) as necessary for thicker oxides. The

charge passed through the FAS solution was monitored until the desired amount of Fe was electrodeposited on the Au electrode. The oxide-coated electrode was then washed and placed immediately in a 0.1 M Na_2SO_4 solution. Oxygen was bubbled through the solution and the open circuit potential (V_{oc}) was monitored until it remained constant (< 0.5 mV/min). The oxide-coated electrode was then added to N_2 purged borate buffer (0.07 M $Na_2B_4O_7$, 0.15 M H_3BO_4, and 0.2 M Na_2SO_4, pH 8.7) in preparation for reduction rate experiments.

Others have characterized the iron-oxides produced by similar methods (Stratmann and Müller, 1994; Ernst, 1984). These studies indicate that the oxide is made primarily of γ-FeOOH (lepidocrocite).

Electrochemical Experiments

Two types of electrochemical experiments were conducted: small-amplitude current-potential (SAIE) curves and current transient experiments. The SAIE experiments were conducted to determine charge transfer kinetics (polarization resistance) of the iron-oxide electrode itself, with various levels of Fe(II) added. The oxide-coated electrode was immersed in borate buffer in a three-electrode configuration with a Ag/AgCl reference electrode and a Pt^0 counter electrode. When Fe(II) sites within the Fe(III)-oxide were desired, Fe(II) was added to the oxide electrochemically by holding the electrode at a constant negative potential (usually −350 mV vs. SHE) to reduce Fe(III) to Fe(II) within the oxide. The charge passed through the iron-oxide was monitored until the desired amount of Fe(II) had been doped into the oxide. Potential sweeps of ±100 mV were applied to the electrode around the open circuit potential (V_{oc}) with a sweep rate of 250 mV/min.
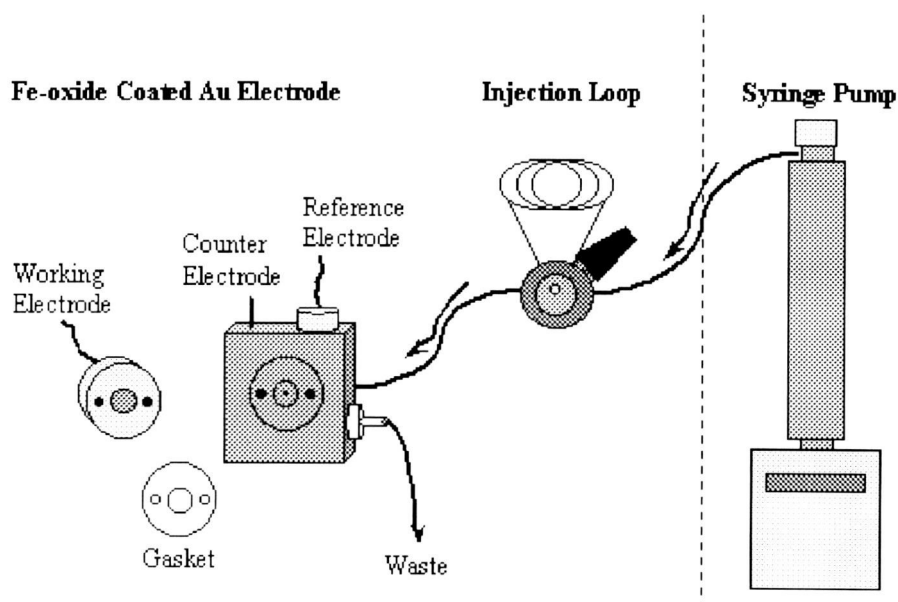
Figure 4.1. Experimental setup for current transient experiments with the wall-jet electrode. Items on the left of the dashed line were stored in an anaerobic glove box.

The second type of experiment conducted was a current transient experiment. In these experiments, the rate of reduction of CT and NB was deduced from the increase in current when a pulse of CT or NB was passed over the electrode in a flowing stream. A well-defined flow-through system similar to a wall-jet electrode was used in these experiments (Figure 4.1). A thin layer cell from Bioanalytical Systems was constructed from three electrodes: a counter electrode (the stainless steel back block), an oxide-coated gold electrode with a diameter of 1.5 mm, and a Ag/AgCl reference electrode. Gaskets were placed between the stainless counter electrode and the oxide-coated gold electrode to create a space of approximately 160 μm. The reference electrode was placed within the counter electrode block, downstream from the working electrode. A large capacity syringe pump was used to create continuous flow in the cell.

When conducting potentiostatic experiments on oxide-coated gold electrodes, a background current was always present. At potentials necessary to reduce CT and NB, the Fe(III) in the iron-oxide is also reduced. Therefore, the background current corresponds to electrochemical generation of Fe(II). Determination of this background current was necessary for all transient experiments; therefore, CT and NB could not be added as components of the mobile phase. The CT and NB were introduced into the flow cell through an injection loop of approximately 10 mL. After injection of NB or CT, a sharp rise in current follows, with the current due to reduction of the organic being the difference between the final current (due to organic reduction and Fe(III) reduction) and the baseline current (due to Fe(III) reduction).

Some experiments were conducted to determine the dependence of organic reduction on mass transport to the surface of the oxide film from the bulk of solution. For these experiments, the flow rate was systematically increased after the current had become constant.

Results and Discussion

All current densities (j) are reported using the macroscopic surface area of the gold electrode (7.07 mm^2), without determining the surface area of the oxide or the microscopic surface area of the gold electrode.

Current-Flow Behavior in a Wall Jet Electrode

A model system was studied to verify that the electrochemical behavior of the flow cell (Figure 4.1) obeyed by the standard equations used to model mass transport limited current. Oxygen was chosen as the model electroactive species. Figure 4.2 shows
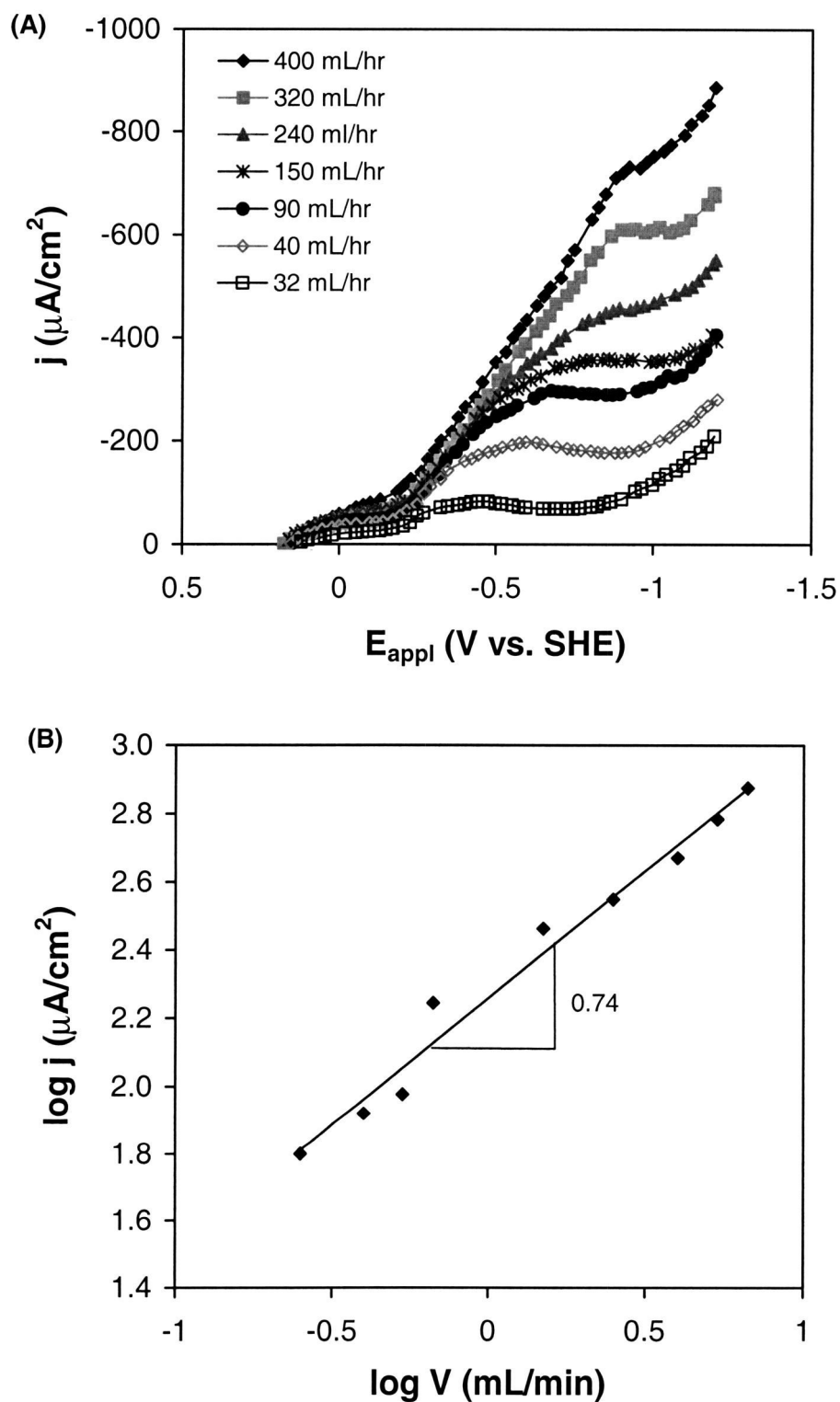
Figure 4.2. Behavior of oxygen on a bare Au electrode in a wall-jet cell. 273 μM O_2 in borate buffer. A) Current-voltage curves of O_2 on Au for a range of flow rates. B) Dependence (log-log) of the limiting current (j) on the flow rate (V).

the dependence of the reduction of O_2 at the gold electrode on the flow rate and the applied potential.

A stagnant film model can be used to quantify the relationship between mass transport of the oxygen to the electrode and the rate of reduction for the wall-jet flow cell. Equations 4.1 and 4.2 describe the limiting current-flow relationship of a wall-jet electrode where the diameter of the inlet port is much smaller than the diameter of the working electrode (Yamada and Matsuda, 1973).

$$j = -nF \frac{D}{\delta} \left(C^o - C^s \right) \qquad (4.1)$$

$$\delta = 0.87 \pi D^{1/3} \nu^{5/12} V^{-3/4} a^{1/2} r^{5/4} \qquad (4.2)$$

where j (A cm^{-2}) is the limiting current density, F is the Faraday constant, C^o is the concentration of an electroactive species in the bulk solution, C^s is the concentration of the electroactive species at the surface, δ (cm) is the characteristic thickness of a stagnant boundary layer, ν is the kinematic viscosity of the electrolyte, a is the diameter of the inlet port, and r is the radius of the working electrode, and V is the flow rate. The limiting current density is the potential region where the current becomes constant as the potential is increasing. The current becomes constant when the concentration of electroactive species at the surface (C^s) becomes negligible when compared to the bulk concentration (C^o). When this occurs the current is said to be the mass transport limited current.

In Figure 4.2a, the potential region where mass transport is limiting is from about -0.9 to -1.1 V. Assuming the bulk concentration is constant, the current is dependent only on the size of the diffusion layer (δ) when the applied potential is in the limiting region. As seen from Equation 4.2, δ is controlled by the flow rate ($V^{-3/4}$). Therefore when Equations 4.1 and 4.2 are combined, j is proportional to $V^{3/4}$. If the rate of reduction were

solely limited by transport of the electroactive species to the surface of the electrode from the bulk of solution, a log-log plot of j as a function of V would give a straight line with a slope of 0.75. As shown in Figure 4.2b, the slope of the log-log relationship is approximately 0.75, which indicates that the mass transport limited rate of O_2 reduction on the gold electrode is adequately described by Equations 4.1 and 4.2. The limiting current density (j) can be calculated directly from Equations 4.1 and 4.2). Although the experimentally determined current densities are higher than the calculated current densities, these values are of the correct order of magnitude.

Electrochemical Characterization of Fe(III)-oxide Films

To ensure Fe(II) addition to the iron-oxide was reversible over the course of the electrochemical experiments, the V_{oc} as a function of %Fe(II) was monitored before and after complete oxidation of the iron-oxide (results shown in Figure 4.3). Initially, increasing fractions of Fe(II) were added to the Fe(III)-oxide film electrochemically. The V_{oc} of the iron-oxide was measured (solid circles) with increasing fractions of Fe(II). Next, the iron-oxide was potentiostatically reoxidized to eliminate any Fe(II) in the oxide film. The experiment was then repeated by doping Fe(II) sites into the Fe(III)-oxide and measuring the V_{oc} at increasing fractions of Fe(II) (open squares).

The V_{oc} of the iron-oxide rapidly decreases as small fractions of Fe(II) are added to the oxide. As more Fe(II) is added, the absolute rate of change of the V_{oc} decreases. This behavior occurs both before and after reoxidation of the iron-oxide film. Also, the absolute values of V_{oc} are approximately equal both before and after reoxidation of the oxide film. Therefore, it appears that Fe(II) sites can be generated without irreversible electrochemical or structural changes to the oxide. Stratmann and Müller (1994) also

found that addition and removal of Fe(II) in a similar oxide in borate buffer is reversible. Although when removed from the borate buffer solution the oxide irreversibly changes morphology at fractions of Fe(II) > 2%.
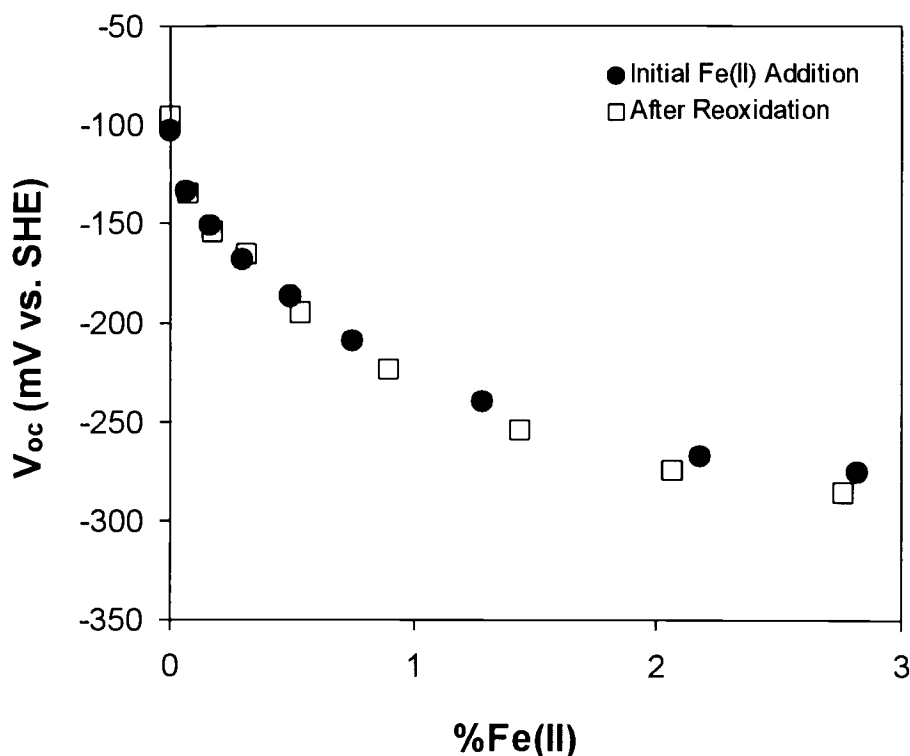
Figure 4.3. Reversibility of the addition and removal of Fe(II) sites in a 23.6 μm Fe(III)-oxide film. The potential was –350 mV (vs. SHE) for the addition of Fe(II) sites. The re-oxidation potential was +200 mV (vs. SHE).

It has been found that the ferrous ion-ferric oxide reaction is important in determining the redox potential of natural fresh waters by Pt electrodes. Doyle (1968) found a Nernstian relationship between the activity of ferrous iron and the redox potential of natural waters as measured with a platinum electrode. A simple Nernstian model was applied to the data in Figure 4.3. A log-linear relationship between the fraction of Fe(II) and V_{oc} was evident, but the slope of this relationship was –106 mV. The large value of

the slope is inconsistent with the Nernst equation because it indicates that only a fraction

of an electron is involved in Fe(III) reduction. Therefore, treating the iron-oxide as an

ideal solid solution and modeling the behavior in Figure 4.3 as simple Nernstian behavior

led to an inadequate description of the data.

SAIE curves were also obtained for the iron-oxide at increasing fractions of Fe(II)

(Figure 4.4). As the Fe(II) increases within the oxide, the absolute value of the current

increases at a particular potential. Also, for small fractions of Fe(II) ($< 0.5\%$), the effect

of Fe(II) addition on the current is pronounced. Yet, at fractions of Fe(II) greater than or

equal to 0.5%, the measured current becomes relatively independent of increases in the

fraction of Fe(II).
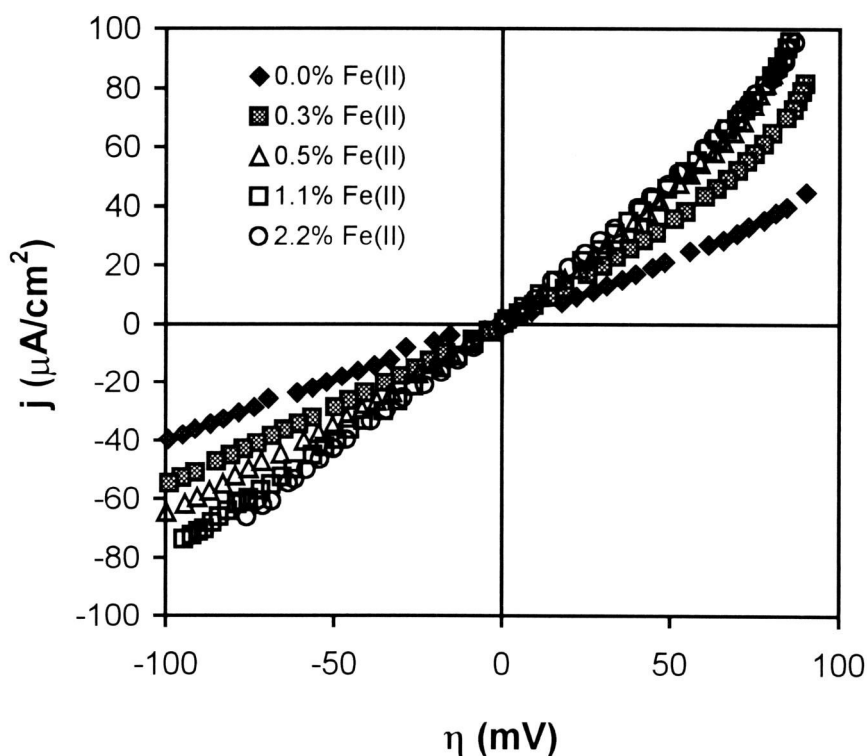
Figure 4.4. SAIE curves for a 23.6 μm Fe(III)-oxide film in borate buffer with various fractions of Fe(II).

Although the Butler-Volmer equation (Equation 4.3) is typically meant for use under the following conditions: no mass transport limitation on current, a one step electron transfer mechanism, and a heterogeneous reaction of an aqueous electroactive species on a bare electrode (Bard and Falkner, 1980), it did a good job of modeling SSIE curves for this more complex system. Equation 4.3 was used to model the SSIE curves in Figure 4.4,

$$j = j_o \left[e^{-\alpha_c n f \eta} - e^{(1-\alpha_a) n f \eta} \right]$$

(4.3)

where j is the net current density, j_o is the exchange current density, α_a is the anodic transfer coefficient, α_c is the cathodic transfer coefficient, n is the number of electrons involved in the reaction, $f = F/RT$, and η is the overpotential ($V-V_{oc}$). The exchange current density (j_o) is the magnitude of the cathodic or anodic currents when the net current density (j) is zero (at V_{oc}). The transfer coefficients (α_a and α_c) are dependent on the shape of the potential energy curve for the anodic and cathodic electron transfer reactions.

Table 4.1 reports the values of j_o, $1-\alpha_a$, and α_c for a non-linear least squares fit of the SSIE data in Figure 4.4 according to Equation 4.3. The values of j_o confirm the trend in Figure 4.4, where j_o increases rapidly for small fractions of Fe(II) and levels off at about 44 $\mu A/cm^2$ as the %Fe(II) within the oxide increases. Similar values of $1-\alpha_a$ and α_c indicate that the shape of the potential energy curve for removal and addition of Fe(II) sites is fairly symmetrical. The addition and removal of Fe(II) over the course of the SSIE experiments seemed to be reversible as evidenced by reproducible SSIE curves for multiple potential sweeps (not shown). Note that the behavior of V_{oc} as a function of the fraction of Fe(II) in the oxide-film is similar to the behavior of the exchange current,

where the V_{oc} changes rapidly for small fractions of Fe(II) and changes less rapidly as the fraction of Fe(II) in the film increases.

Table 4.1. Comparison of α and j_o of a 23.6 μm iron-oxide with variable amounts of Fe(II).

%Fe(II)[a]	j_o (μA/cm^2)	1-α_a	α_c
0	21.2	0.27	0.21
0.3	31.1	0.30	0.20
0.5	38.2	0.31	0.19
1.1	43.8	0.28	0.21
2.2	45.3	0.27	0.22

[a] Calculated by dividing the measured amount of Fe(III) by the calculated amount of Fe(II).

[b] j_o, α_a, and α_c were adjusted to fit the SAIE data in Figure 4.4 by a nonlinear least squares optimization routine.

Mass Transport of Electroactive Species

Figure 4.5 shows the data from a typical transient experiment, in which the current density tracks the concentration as a pulse of NB passes the electrode surface. The electroactive species was then injected into the flow cell. A sharp rise in the current density above the baseline (27 μA/cm^2) follows, with the difference between the measured current density and the baseline current density attributable to the reduction of NB or CT. In Figure 4.5, NB was injected at a flow rate of 40 mL/hr. The flow rate was increased twice while NB was passing through the flow cell (40 mL/hr initial, 150 mL/hr at 260 s, and 400 mL/hr at 310 s). Slight increases in current can be observed shortly after these increases in flow rate. As the NB leaves the flow cell a sharp drop in current follows, and the current returns to the baseline value. The behavior of the current in

Figure 4.5, when increasing the flow rate, was observed in almost all current transient experiments to various degrees.
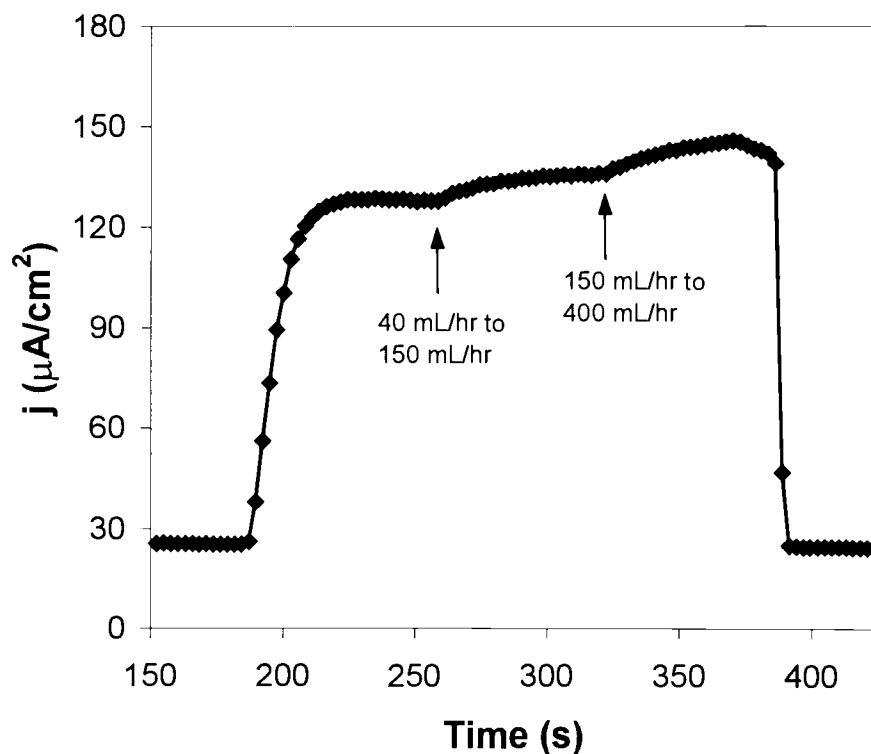
Figure 4.5. Injection of NB from a 10 mL injection loop into the wall jet flow cell: 310 μM NB in borate buffer, -350 mV (vs. SHE), 1.1% Fe(II), and 0.92 μm oxide-film. The flow rate ranged from 40 mL/hr to 400 mL/hr.

The question arises whether the maximum current (in Figure 4.5) is due to an exhaustion of the available electroactive species, mass transport of the electroactive species to the surface of the oxide film, or some other process. The first possibility can be addressed by calculating the amount of NB and CT actually reduced at the electrode. Calculations for 310 μM NB (at 40 mL/hr) indicate that approximately 3.44 nmol NB are passed over the working electrode every second. Using the *highest* experimental reduction rate found for NB of 110 μA/cm^2 and a two electron reduction reaction, NB is

reduced at a rate of 40 pmol s^{-1}. Therefore, only about 1% of the NB passing through the flow cell is reduced. Similar calculations for CT indicate that only 0.1% is reduced (at the highest experimental reduction rate found for CT).

We can determine the effect of mass transport to the surface of the oxide film on the reduction rate by studying the rise in current density as the flow rate over the oxide film is varied (Figure 4.5). If the increase in current in the transient experiment were attributable to the increase in flow (i.e. the rises in current are exclusively due to changes in mass transport), we can quantify the relationship between mass transport of the electroactive species to the surface of the oxide and the rates of reduction by using a stagnant film model for the wall-jet flow cell (Equations 4.1 and 4.2). As stated above, the important feature of this model is that j is proportional to $V^{3/4}$. Therefore, if the rate of reduction were solely limited by transport of the organic to the surface of the oxide film from the bulk of solution, a log-log plot of j as a function of V would give a straight line with a slope of 0.75. Reported in Table 4.2 are the slopes of a log-log plot of reduction current as a function of flow rate for various iron-oxides. The slopes are much smaller than 0.75, which indicates that mass transport of NB and CT to the surface of the oxide has little control over the observed rates of reduction.

These calculations along with Table 4.2, provide strong evidence that exhaustion of the electroactive species and mass transport of NB and CT to the surface of the oxide-film are not limiting the overall rate of reduction and that the maximum current density in Figure 4.5 must be due to some other process.

Table 4.2. Effect of flow rate to the surface of the iron-oxide on the reduction rate of NB and CT.

| Slope of log j vs log V | | Oxide Thickness |
CT	NB	$(\mu m)^a$
0.098	0.060	0.92
0.049	0.018	2.06
0.013	0.001	8.10
0.037	0.009	11.2
0.170	0.098	23.7

[a] Calculated by assuming a density for γ-FeOOH and using the measured concentration of Fe(III) for each oxide.

Concentration of NB and CT

The concentrations of CT and NB were varied to determine if the rate of reduction is first order in concentration. Figure 4.6 illustrates the concentration dependence of the current density for 310-77.5 µM NB and 631-158 µM CT. As shown by Figure 4.6, the concentration dependence of current is first order (linear) and can be easily explained by Equation 4.4.

$$j = nFk_{obs}C^{\circ}$$ (4.4)

where k_{obs} (µm s^{-1}) is the rate constant of the reduction reaction.
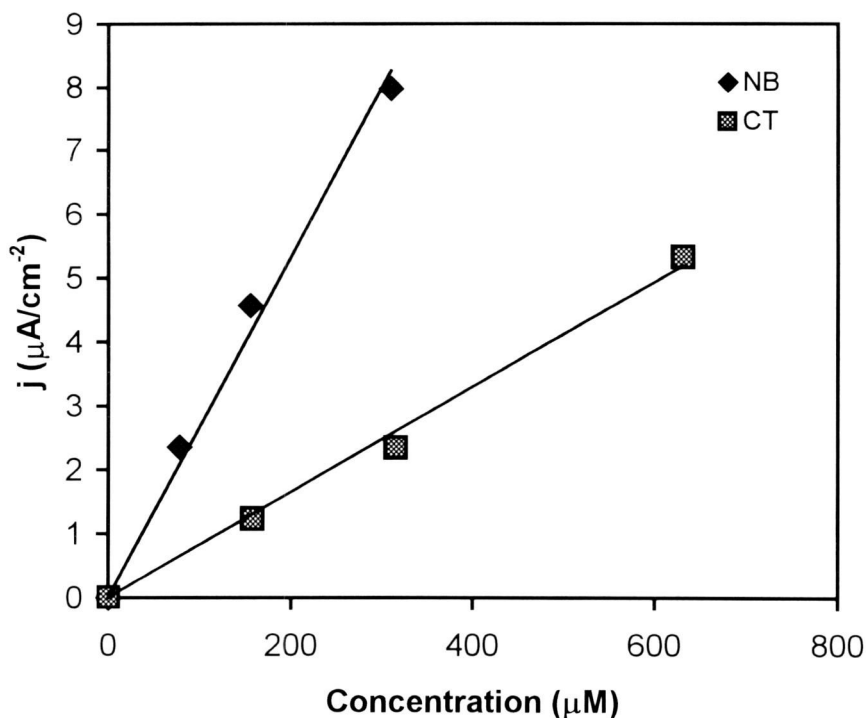
Figure 4.6. Current density of NB and CT reduction as a function of the concentration of electroactive species on a 8.1 μm oxide film. Potentiostat at -350 mV (vs. SHE) in borate buffer with a flow rate of 40 mL/hr. Linear regression of the data produced lines with the following statistics: $j = 29.6 \times 10^{-3} C^{\circ}$, $R^2 = 0.99$ for NB; $j = 7.5 \times 10^{-3} C^{\circ}$, $R^2 = 0.98$ for CT.

Fe(II) Content of the Iron-Oxide

Figure 4.7 illustrates how the fraction of Fe(II) in the iron-oxide affects the reduction rate of NB and CT. The current due to reduction of CT and NB remains constant as Fe(II) is electrochemically added to the iron-oxide, indicating that there is little dependence of reduction rates on the amount of Fe(II) contained in the iron-oxide. Conversely, the reduction rate of O_2 was found to be dependent on the amount of Fe(II) in the Fe(III)-oxide film, both in the current study (not shown) and by Stratmann and Müller (1994). Also, the reduction rate of NB has been found to be dependent on the

amount of Fe(II) adsorbed to an iron-oxide with no zero-valent metal present (Klausen et al., 1995).
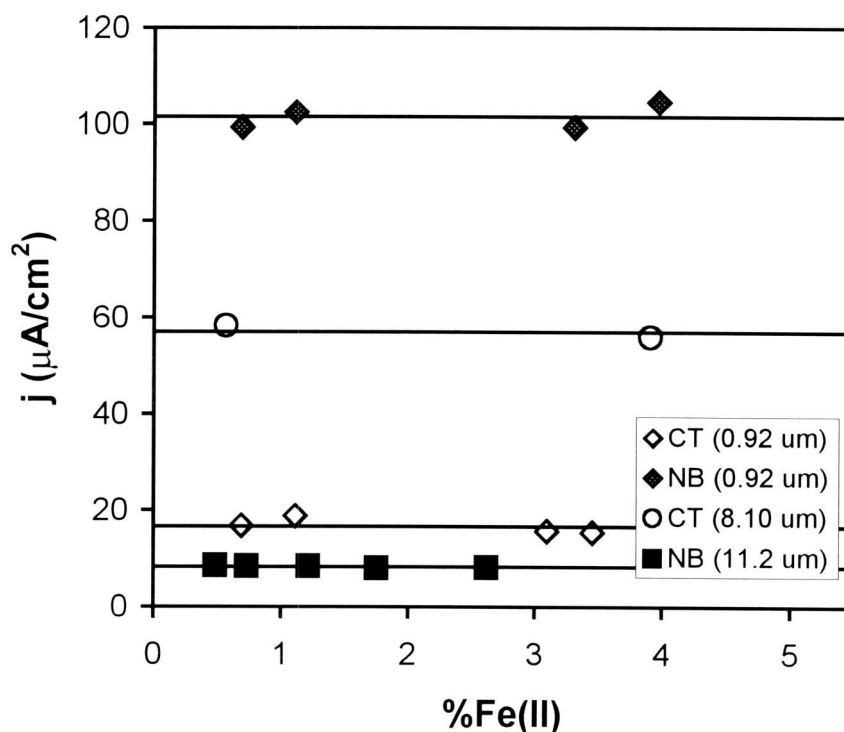
Figure 4.7. Dependence of rate on the fraction of Fe(II) present in the iron-oxide. Potentiostat at -350 mV (vs. SHE) in borate buffer with a flow rate of 40 mL/hr.

Assuming the Fe(II) sites are uniformly distributed throughout the oxide film, it seems that the location of CT and NB reduction is not at Fe(II) sites within the oxide film. The independence of CT and NB reduction on the Fe(II) content of the oxide film could be explained in two ways. First, CT and NB may not be penetrating the iron-oxide and only reacting at the surface of the oxide film, whereas, O_2 is able to flow into the pores of the oxide and react with the Fe(II) in the oxide film. If NB and CT were reacting only at the surface of the oxide film, the addition of Fe(II) sites within the film would not

influence their reduction rates. Second, CT and NB may only react on the gold surface and not with the Fe(II) incorporated in the Fe(III)-oxide. Therefore, no matter what fraction of Fe(II) is in the oxide film, the CT and NB would react at the same rate on the gold electrode (for the same oxide). To differentiate between these two mechanisms, the effect of thickness on the rates of NB and CT reduction was explored (see below).

Thickness of the Iron-Oxide

The dependence of k_{obs} (calculated with Equation 4.4) on the thickness of the iron-oxide (d) is reported in Table 4.3. The experimentally determined rate constants for each electroactive species on a bare gold electrode are also reported in Table 4.3 for reference to the maximum rate possible in these experiments. A two electron reduction reaction was assumed for CT and NB, and a four electron reaction was assumed for oxygen. It should be noted that we did not verify whether O_2 reduction was mass transport limited on an oxide-coated gold electrode.

The value of k_{obs} ranges three and two orders of magnitude for NB and CT, respectively (when an oxide film is present). It is obvious that oxide thickness controls the rate of reduction for both CT and NB. Yet, it cannot be discerned with Table 4.3 whether the CT and NB are being reduced at the surface of the oxide or the gold electrode.

Table 4.3. Rate of reduction for electroactive species on a bare gold electrode and Fe(III)-oxide coated gold electrodes of various thickness.

Oxide Thickness $(\mu m)^a$	k_{obs} $(\mu m\ s^{-1})^b$		
	CT	NB	O_2
no oxide	3.93 ± 0.17	20.4 ± 0.39	20.4 ± 1.05
0.92	1.37 ± 0.12	17.0 ± 0.43	ND
2.06	2.58 ± 0.21	18.4 ± 0.65	variable
8.10	0.479 ± 0.086	1.39 ± 0.037	ND
11.2	0.469 ± 0.013	0.274 ± 0.023	ND
23.7	0.022 ± 0.012	0.012 ± 0.002	ND

^{a} Calculated by assuming a density for γ-FeOOH and using the measured concentration of Fe(III) for each oxide.

^{b} Calculated with a 2 electron reaction for CT and NB and a 4 electron reaction for O_2.

To differentiate between the possible locations of reduction, the shapes of the current transients were studied to determine if the thickness of the oxide had any control over the time necessary for reduction rates to reach their final values. Figure 4.8 shows the lag time of NB reduction for three different oxides. The current is normalized to its final value and t^0 is the initial injection of the NB. The time necessary for the current to reach its final value increases with increasing oxide thickness. This indicates that as the thickness increases the NB must travel a longer distance to reach the site of the reduction reaction. Therefore, the NB must be travel into the oxide to be reduced, indicating that the location of NB reduction is at the surface of the gold electrode. Similar results were obtained for CT.
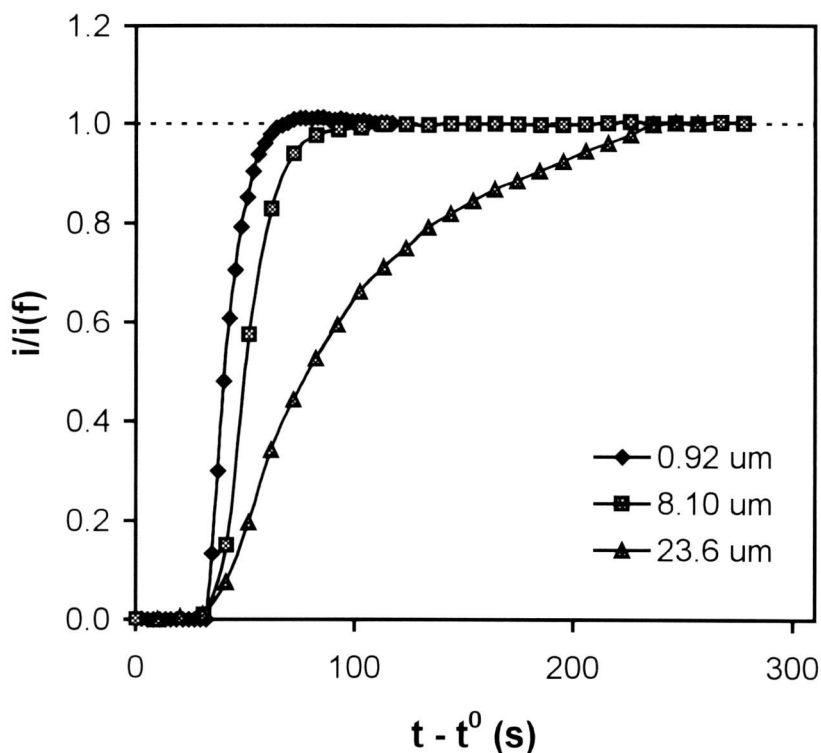
Figure 4.8. Time necessary for the current due to NB reduction to reach its final value for oxide films of various thickness. Potentiostat at -350 mV (vs. SHE) in borate buffer with a flow rate of 40 mL/hr.

If the thickness of the oxide film controls the rate of reduction, mass transport through the oxide may be the rate-limiting step in the reduction of CT and NB. Equation 4.5 describes kinetics limited by mass transport of chemicals through porous media.

$$k_{mt} = \frac{D_{eff}}{d} \qquad (4.5)$$

where k_{mt} is rate constant that is used to quantify steady-state mass transport through a film, in this case, the oxide film. D_{eff} is the effective diffusion coefficient of CT or NB within the iron-oxide film and d is the thickness of the oxide film. The effective diffusion coefficient is some value lower than the diffusion coefficient of a chemical in electrolyte

solution. Several factors can act to reduce D_{eff}, such as: tortuosity, retardation, and constrictivity. It should be noted that Equation 4.5 does not take into account the reduction of electrode surface area available when the oxide film is deposited. Also, the surface area of gold available for facilitating the electron transfer reaction may or may not be constant as oxides of increasing thickness are deposited on the electrode. The important element of Equation 4.5 is that the rate of reduction is proportional to d^{-1}. Figure 4.9 represents the experimental data in these terms.

Except for the thinnest oxide film (Table 4.3), there is a good correlation between the experimental k_{obs} values and d^{-1}. Therefore, although Equation 4.5 does not account for some possible phenomena (i.e., changes in electroactive area of the electrode and changes in D_{eff} at different oxide thickness), the relationship between k_{obs} and the oxide thickness can be modeled by this equation for most of the data. The model provides evidence that the rate of reduction is controlled by mass transport through the oxide film.

The tortuosity, constrictivity, and retardation factors that determine the value of D_{eff} can all change as oxide thickness changes. At constant oxide thickness, tortuosity and constrictivity should be fairly similar for NB and CT, because the molar volumes of these two compounds are very similar (assuming molar volume is a good indicator of special similarity). The diffusion coefficients of NB and CT in aqueous solution are also reasonably similar ($\sim9.5\times10^{-6}$ cm^2 s^{-1}). This similarity indicates that differences in retardation of NB and CT are most likely responsible for the differences in k_{obs} at small oxide thickness (< 11.2 μm), with CT retarded by the iron-oxide to a greater extent than NB. To our knowledge, specific adsorption of CT and NB on Fe(III)-oxides of this type have not been experimentally determined.
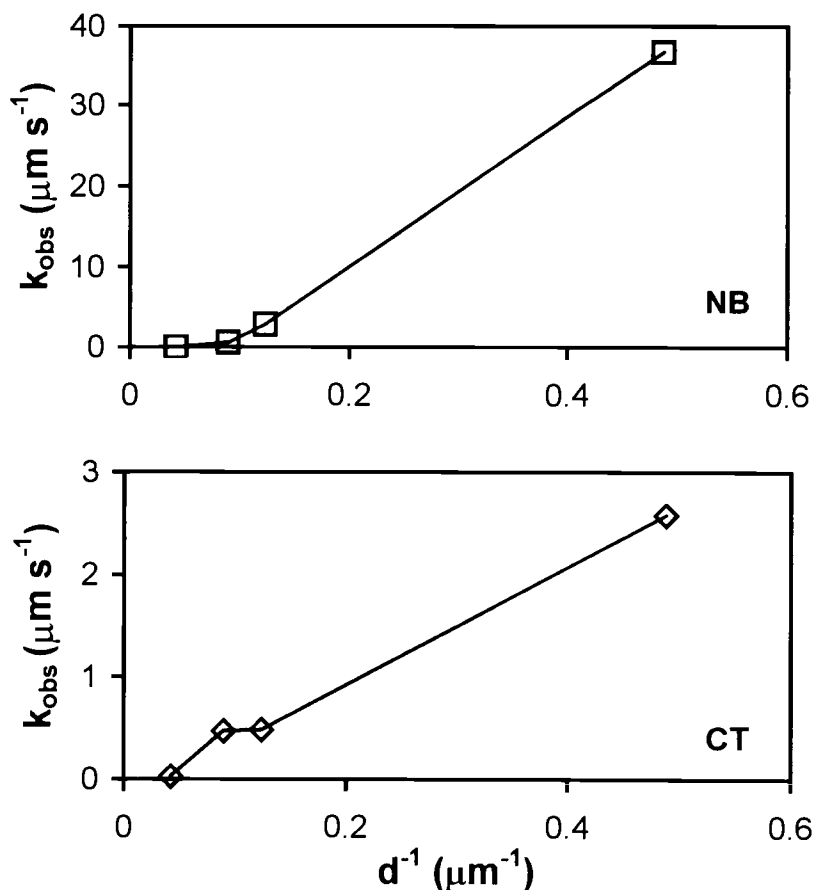
Figure 4.9. Dependence of the observed rate constant on mass transport through the oxide. Potentiostat at -350 mV (vs. SHE) in borate buffer with a flow rate of 40 mL/hr.

As seen in Figure 4.9, NB is more sensitive to changes in oxide thickness than CT. This enhanced sensitivity can be explained by considering the relative effect of constrictivity on NB and CT transport through the oxide film. NB is a much more rigid molecule than CT and would have to orient itself before entering small pores near the electrode surface, whereas, because of its greater flexibility, CT would not suffer as much from these constraints. If we assume that the pores near the electrode surface are

becoming smaller as more iron is deposited on the electrode, the reduction rate of NB would be more sensitive to changes in oxide thickness.

Steric limitations could also explain the non-zero intercepts for both CT and NB in Figure 4.9. The non-zero intercept for NB and CT can be explained if we consider that as the oxide thickness increases, diffusion paths near the gold surface may decrease in size and even fill in completely. Therefore, because of steric limitations, the reduction of CT and NB could effectively cease before the oxide was infinitely thick.

Considering Figures 4.8 and 4.9, the location of the reduction reaction for CT and NB appears to be at the surface of the gold electrode.

Where does CT and NB reduction take place and what limits the rate of reduction?

Mass transport to the surface of the oxide and the fraction of Fe(II) within the Fe(III)-oxide have little effect on the reduction rates of CT and NB. Conversely, the rates of reduction greatly depend on thickness of the iron-oxide, with mass transport through the oxide film playing an important role in the rate of CT and NB reduction (Figure 4.9). The thickness of the oxide film affects not only the magnitude of k_{obs}, but also the shape of the current transient, increasing the time necessary for the current to reach its final value. It is obvious from Figures 4.8 and 4.9 that the CT and NB must enter the oxide film to be reduced. If these compounds were being reduced at the Fe(II) sites within the film, it would be expected that the fraction of Fe(II) in the oxide would influence the rate of reduction of NB and CT. This is not the case.

Based on the evidence presented in this study, the reduction reaction of CT and NB is most likely occurring at the surface of the gold electrode, with transport through

the film limiting rates of reduction. Therefore, it appears that the oxide acts as a physical barrier, inhibiting direct contact between the gold and the electroactive species, increasing the diffusion length (tortuosity), and creating adsorption sites for the NB and CT (retardation).

Conclusions

The rates of CT and NB reduction are controlled by the thickness of the oxide film. It was found that the fraction of Fe(II) within the oxide film was unimportant in determining the rates of reduction of these two compounds, and that CT and NB penetrate the oxide film before being reduced. Therefore, the location of CT and NB reduction is near the surface of the gold electrode. The oxide film acts as a physical barrier to restrict contact between the gold electrode and the electroactive species, with mass transport through the oxide being the rate limiting step in the reduction reaction.

The observations found in this study may explain the large difference in literature values sited for the reduction constants of CT on elemental iron. Most workers attempting to measure these rate constants use column or batch type experiments with no control over the growth or type of oxide film on elemental iron. As seen in Table 4.3, the observed rate constant (k_{obs}) can differ by two orders of magnitude, depending on the thickness of an oxide film. Little control over the type and size of an oxide film in batch or column experiments may account for literature values that differ by two orders of magnitude (Johnson et. al, 1996).

The findings of this study have important implications for remediation using zero-valent metal PRBs. Our investigation suggests that reduction of CT and NB by zero-valent metal PRBs can be enhanced in one of two ways: 1) limit the thickness of an oxide

film on a zero-valent metal or 2) enhance the reduction rate of the metal for the

electroactive species of interest (e.g. adding a catalyst to the metal). The first option may

be difficult when considering the difficulty in controlling the thickness of oxides in

aqueous environmental systems. Cathodic protection has been suggested as a means of

increasing the effective lifetime of a Pd catalyst on zero-valent iron (Li and Farrell, 2000)

and may be one way to slow the growth of oxides on zero-valent metals. Enhancing the

reduction rate of zero-valent metals in PRBs seems to a promising option. Several

investigations have tried to use this idea with varying degrees of success (Cheng et al.,

1997; Muftikian et al., 1996; Li and Farrell, 2000). Most have observed limited lifetimes

for the enhancements because of buildup of obstructing oxides, loss of the catalyst from

the supporting medium, poisoning of the catalysts, or other problems. If these limitations

can be overcome, it seems that increasing the activity of the metal for an electroactive

species of interest is a promising way to enhance degradation of organic contaminants

with PRBs.

Acknowledgments

References

Abdel-Samad H. and Watson P. R. (1998) An XPS Study of Adsorption of Lead on Goethite (α-FeOOH). *Appl. Surf. Sci.* **136**, 46-54.

Agrawal A. and Tratnyek P. G. (1996) Reduction of Nitro Aromatic Compounds by Zero-Valent Iron Metal. *Environ. Sci. Technol.* **30**, 153-160.

Bard A. J. and Faulkner L. R. (1980) Electrochemical Methods. John Wiley and Sons.

Cheng I. F., Fernando Q. and Korte N. (1997) Electrochemical Dechlorination of 4-Chlorophenol to Phenol. *Environ. Sci. Technol.* **31**, 1074-1078.

Doyle R. W. (1968) The Origin of the Ferrous Ion-Ferric Oxide Nerst Potential in Environments Containing Dissolved Ferrous Iron. *Am. J. Sci.* **266**, 840-859.

Ernst K. (1984) Unterschungen über Phasenumwandlungen an reinen Eisenoxiden im Hinblick auf die atmosphärische Korrosion. Thesis. der Universität Erlangen-Nürnberg.

Johnson T. L., Scherer M. M., and Tratnyek P. G. (1996) Kinetics of Halogenated Organic Compound Degradation by Iron Metal. *Environ. Sci. Technol.* **30**, 2634-2640.

Johnson T. L. and Tratnyek P. G. (1994) A Column Study of Geochemical Factors Affecting Reductive Dechlorination of Chlorinated Solvents by Zero-Valent Iron. In *In-Situ Remediation: Scientific Basis for Current and Future Technologies* (ed. G. W. Gee and N. R. Wing), pp. 931-947. Battelle Press.

Klausen J., Tröber S. P., Haderlein S. B., and Schwarzenbach R. P. (1995) Reduction of Substituted Nitrobenzenes by Fe(II) in Aqueous Mineral Suspensions. *Environ. Sci. Technol.* **29**, 2396-2404.

Li T. and Farrell J. (2000) Reductive Dechlorination of Trichloroethene and Carbon Tetrachloride Using Iron and Palladized-Iron Cathodes. *Environ. Sci. Technol.* **34**, 173-179.

Liger E., Charlet L., and VanCappellen P. (1999) Surface Catalysis of Uranium(VI) Reduction by Iron(II). *Geochim. Cosmochim. Acta* **63**, 2939-2956.

Muftikian R., Nebesny K., Fernando Q., and Korte N. (1996) X-ray Photoelectron Spectra of the Palladium-Iron Bimetallic Surface Used for the Rapid Dechlorination of Chlorinated Organic Environmental Contaminants. *Environ. Sci. Technol.* **30**, 3593-3596.

Sayles G. D., You G., Wang M., and Kupferle M. J. (1997) DDT, DDD, and DDE Dechlorination by Zero-Valent Iron. *Environ. Sci. Technol.* **31**, 3448-3454.

Scherer M. M., Westall J. C., Ziomek-Moroz M., and Tratnyek P. G. (1997) Kinetics of Carbon Tetrachloride Reduction at an Oxide-Free Iron Electrode. *Environ. Sci. Technol.* **31**, 2385-2391.

Seaman J. C., Bertsch P. M., and Schwallie L. (1999) In Situ Cr(VI) Reduction within Coarse-Textured, Oxide-Coated Soil and Aquifer Systems Using Fe(II) Solutions. *Environ. Sci. Technol.* **33**, 938-944.

Sørensen J. and Thorling L. (1991) Stimulation by Lepidocrocite (γ-FeOOH) of Fe(II)-Dependent Nitrite Reduction. *Geochim. Cosmochim. Acta* **55**, 1289-1294.

Stratmann M. and Müller J. (1994) The Mechanism of the Oxygen Reduction on Rust-covered Metal Substrates. *Corr. Sci.* **36**, 327-359.

Tratnyek P. G. (1996) Putting Corrosion to Use: Remediating Contaminated Groundwater with Zero-Valent Metals. *Chem. Ind. (London)*, 499-503.

Yamada J. and Matsuda H. (1973) Limiting Diffusion Currents in Hydrodynamic Voltammetry: III. Wall Jet Electrodes. *Electroanal. Chem. Interfacial Electrochem.* **44**, 189-198.

Chapter 5: Summary

Some processes by which iron-oxides affect the transport and degradation of inorganic and organic contaminants in the subsurface environment were studied. Iron-oxides were found to control the adsorption of U(VI) on iron-rich sands. Extraction of U(VI) from these materials could be promoted by the use of citrate, of which the primary effect was dissolution of the oxide rather than complexation of U(VI). The thickness of the oxide film was the determining factor in the rate of carbon tetrachloride (CT) and nitrobenzene (NB) reduction on an iron-oxide coated gold electrode.

With regard to the modeling of U(VI) adsorption on iron-rich sands, a number of conclusions could be reached. A classical surface complexation model, based on published parameters that were derived for a pure iron-oxide, predicted adsorption to natural materials remarkable well. This result indicates that U(VI) adsorption on the sand behaves almost as if U(VI) were adsorbing to a pure iron-oxide. Then, at least for some heterogeneous environmental sorbents, a preliminary model can be produced from published parameters and simple characterization of the environmental sorbent. Even though the model calibrated on pure iron-oxides does a good job modeling U(VI) adsorption on the natural sands, it appears that calibrating the model on natural sands produces a much better model of the true U(VI) adsorption behavior. Lastly, affinity spectrum models are more effective at representing real material over a range of uranium concentrations than are classical 1- or 2-site models.

The presence of organic complexing agents in the subsurface can greatly complicate adsorption phenomena. In this study, addition of citrate to extract U(VI) from iron-oxide coated sands resulted in dissolution of the iron-oxide and removal of

adsorption sites. This surface alteration by citrate extraction was found to change both the *chemical* reactivity (i.e., removal of extremely reactive iron-oxides) and the bulk *physical* properties (i.e., decrease in specific surface area) of the iron-rich sorbent. Alteration of the *chemical* composition of the surface, resulting a decrease in affinity of the sorbent, was found to be the determining factor in the adsorption of U(VI). Over the course of this study, experimental evidence was also found for an extremely reactive phase of iron that is extracted by citrate. Without this reactive surface phase the adsorption of U(VI) dramatically decreases. Two more levels of reactivity of the sand were indicated when the sand was extracted with different extraction techniques. Multiple levels of affinity for U(VI) by the iron-rich sand support the use of multiple reactivity sites for surface complexation modeling of heavy metal adsorption (e.g. strong and weak site types).

The rates of CT and NB reduction were controlled by the thickness of an iron-oxide film. CT and NB were found enter the oxide film to be reduced, yet the fraction of Fe(II) within the oxide film was unimportant in determining the rates of reduction of these two compounds. The results of this study suggest that the oxide film acts as a physical barrier to restrict contact between the gold electrode and the organic contaminants. The location of reduction of CT and NB was determined to be near the surface of the gold electrode and mass transport through the oxide being the rate limiting step in the reduction reaction.

Bibliography

Agrawal A. and Tratnyek P. G. (1996) Reduction of Nitro Aromatic Compounds by Zero-Valent Iron Metal. *Environ. Sci. Technol.* **30**, 153-160.

Azizian M. F. and Nelson P. O. (1998) Lead Sorption, Chemically Enhanced Desorption, and Equilibrium Modeling in an Iron-Oxide-Coated Sand and Synthetic Groundwater System. In *Adsorption of Metals by Geomedia* (ed. E.A. Jenne), Chap. 6, pp. 165-180. Academic Press.

Bailey E. H., Kemp A. J., and Ragnarsdottir K. V. (1993) Determination of Uranium and Thorium in Basalts and Uranium in Aqueous Solution by Inductively Coupled Plasma Mass Spectrometry. *J. Anal. At. Spectrom.* **8**, 551-556.

Bard A. J. and Faulkner L. R. (1980) Electrochemical Methods. John Wiley and Sons.

Bertetti, F. P., Pabalan R. T., Turner D. T., and Almendarez M. (1995) Experimental and Modeling Study of Uranium(6+) Sorption on Quartz. Draft manuscript, Center for Nuclear Waste Regulatory Analyses, San Antonio, TX.

Bose P. and Reckow D. A. (1997) Modeling pH and Ionic Strength Effects on Proton and Calcium Complexation of Fulvic Acid: A Tool for Drinking Water-NOM Studies. *Environ. Sci. Tech.* **31**, 765-770.

Brooks S. C., Taylor D. L., and Jardine P. M. (1996) Reactive Transport of EDTA-Complexed Cobalt in the Presence of Ferrihydrite. *Geochim. Cosmochim. Acta* **60**, 1899-1908.

Brunauer S., Emmett P. H., and Teller E. (1938) Adsorption of Gases in Multimolecular Layers. *J. Am. Chem. Soc.* **60**, 309-319.

Černík M., Borkovec M., and Westall J. C. (1995) Regularized Least-Squares Methods for the Calculation of Discrete and Continuous Affinity Distributions for Heterogeneous Sorbents. *Environ. Sci. Tech.* **29**, 413-425.

Černík M., Borkovec M., and Westall J. C. (1996) Affinity distribution Description of Competitive Ion Binding to Heterogeneous Materials. *Langmuir* **12**, 6127-6137.

Cheng I. F., Fernando Q. and Korte N. (1997) Electrochemical Dechlorination of 4-Chlorophenol to Phenol. *Environ. Sci. Technol.* **31**, 1074-1078.

Cowan C. E., Zachara J. M., Smith S. C., and Resch C. T. (1992) Individual Sorbent Contributions to Cadmium Sorption on Ultisols of Mixed Mineralogy. *Soil Sci. Soc. Amer. J.* **56**, 1084-1094.

Davis J. A. and Kent D. B. (1990) Surface complexation modeling in aqueous geochemistry. In *Mineral-Water Interface Geochemistry* (ed. M.F. Hochella and A.F. White); *Rev. Mineral.* 23, pp. 177-260. Mineralogical Society of America.

DeFlaun M. F., Murray C. J., Holben W., Scheibe T., Mills A., Griffin T., Majer E., and Wilson, J. L. (1997) Preliminary observation on bacterial transport in a coastal plain aquifer. FEMS *Microbiol. Review* 20, 473-487.

Doyle R. W. (1968) The Origin of the Ferrous Ion-Ferric Oxide Nerst Potential in Environments Containing Dissolved Ferrous Iron. *Am. J. Sci.* 266, 840-859.

Dzombak A. D. and Morel F. M. M. (1990) *Surface Complexation Modeling: Hydrous Ferric Oxide*. John Wiley and Sons.

Elliott H. A. and Denney C. M. (1982) Surface Ionization and Complexation at the Oxide/Water Interface. 3. Adsorption of Anions. *J. Colloid Interface Sci.* 74, 32-43.

Ernst K. (1984) Unterschungen über Phasenumwandlungen an reinen Eisenoxiden im Hinblick auf die atmosphärische Korrosion. Thesis. der Universität Erlangen-Nürnberg.

Geelhoed J. S., Hiemstra T., and Van Riemsdijk W. H. (1997) Phosphate and Sulfate Adsorption on Goethite: Single anion and Competitive Adsorption. *Geochim. Cosmochim. Acta* 61, 2389-2396.

Geipel G., Bernhard G., Brendler V., and Nitsche H. (1996) Sorption of Uranium(VI) on Rock Material of a Mine Tailing Pile: Solution Speciation by Fluorescence Spectroscopy. *Radiochim. Acta* 74, 235-238.

Girvin D. C., Gassman P. L., and Bolton H. (1993) Adsorption of Aqueous Cobalt Ethylenediaminetetraacetate by δ–Al_2O_3. *Soil Sci. Soc. Am. J.* 57, 47-57.

Greenberg A. E., Clesceri L. S., and Eaton A. D. (1992) *Standard Methods for the Examination of Water and Waste Water*. American Public Health Association.

Grenthe I., Fuger J., Lemire R. J., Muller A. B., Nguyen-Trung C., and Wanner H. (1992) *Chemical Thermodynamics of Uranium*. Elsevier.

Herbelin A. L. and Westall J. C. (1999) *FITEQL: A Computer Program for Determination of Chemical Equilibrium Constants from Experimental Data, Version 4.0.* Chemistry Department, Oregon State Univ.

Hesse P.R. (1971) *A Textbook of Soil Chemical Analysis*. Chemical Publishing Company.

Holmen B. A. and Casey W. H. (1996) Hydroxamate Ligands, Surface Chemistry, and the Mechanism of Ligand-Promoted Dissolution of Goethite [α-FeOOH(s)]. *Geochim. Cosmochim. Acta* 60, 4403-4416.

Hsi C. D. and Langmuir D. (1985) Adsorption of Uranyl onto Ferric Oxyhydroxides: Application of the surface complexation site-binding model. *Geochim. Cosmochim. Acta* **49**, 1931-1941.

Jackson M. L., Chin H. L., and Zelazny L. W. (1986) Oxides, Hydroxides, and Aluminosilicates. In *Methods of Soil Analysis* (ed. A. Klute) Vol. 1, Chap. 6, pp. 101-150. Soil Science Society of America.

Johnson T. L. and Tratnyek P. G. (1994) A Column Study of Geochemical Factors Affecting Reductive Dechlorination of Chlorinated Solvents by Zero-Valent Iron. In *In-Situ Remediation: Scientific Basis for Current and Future Technologies* (ed. G. W. Gee and N. R. Wing), pp. 931-947. Battelle Press.

Johnson T. L., Scherer M. M., and Tratnyek P. G. (1996) Kinetics of Halogenated Organic Compound Degradation by Iron Metal. *Environ. Sci. Technol.* **30**, 2634-2640.

Killey R.W., McHugh J. O., Champ D. R., Cooper E. L., and Young J. L. (1984) Subsurface Cobalt-60 Migration from a Low-level Waste Disposal Site. *Environ. Sci. Technol.* **18**, 148-157.

Klausen J., Tröber S. P., Haderlein S. B., and Schwarzenbach R. P. (1995) Reduction of Substituted Nitrobenzenes by Fe(II) in Aqueous Mineral Suspensions. *Environ. Sci. Technol.* **29**, 2396-2404.

Klewiki J. K. and Morgan J. J. (1999) Dissolution of β-MnOOH particles by ligands: Pyrophosphate, Ethylenediaminetetraacetate, and Citrate. *Geochim. Cosmochim. Acta* **63**, 3017-3024.

Kohler M., Curtis G. P., Kent D. B., and Davis J. A. (1996) Experimental Investigation and Modeling of Uranium(VI) Transport under Variable Chemical Conditions. *Water Resour. Res.* **32**, 3539-3551.

Kraemer S. M., Chiu V. Q., and Hering J. G. (1998) Influence of pH and Competitive Adsorption on the Kinetics of Ligand-Promoted Dissolution of Aluminum Oxide. *Environ. Sci. Technol.* **32**, 2876-2822.

Langmuir D. (1978) Uranium solution-mineral equilibria at low temperatures, with applications to sedimentary ore deposits. *Geochim. Cosmochim. Acta* **42**, 547-569.

Li T. and Farrell J. (2000) Reductive Dechlorination of Trichloroethene and Carbon Tetrachloride Using Iron and Palladized-Iron Cathodes. *Environ. Sci. Technol.* **34**, 173-179.

Lieser K. H., Quandt-Klenk S., and Thybusch B. (1992) Sorption of Uranyl Ions on Hydrous Silicon Dioxide. *Radiochim. Acta* **57**, 45-50.

Liger E., Charlet L., and VanCappellen P. (1999) Surface Catalysis of Uranium(VI) Reduction by Iron(II). *Geochim. Cosmochim. Acta* **63**, 2939-2956.

Logue B. A., Westall J. C., and Smith R. W. (2000) U(VI) Adsorption on Natural Iron Coated Sands: Comparison of Surface Complexation Approaches to Modeling Adsorption on Heterogeneous Environmental Materials. In preparation.

Loux N. T., Brown D. S., Chafin C. R., Allison J. D., and Hassan S. M. (1989) Chemical Speciation and Competitive Cationic Partitioning on a Sandy Aquifer Material. *Chem. Speciation Bioavailability* **1**, 111-125.

McKinley J. P., Zachara J. M., Smith S. C., and Turner G. D. (1995) The influence of uranyl hydrolysis and multiple site binding reactions on adsorption of U(VI) to montmorillonite. *Clays Clay Mineral.* **43**, 586-598.

Means J. L., Crerar D. A., and Duguid J. O. (1978) Migration of radionuclide wastes: Radionuclide Mobilization by Complexing Agents. *Science (Washington, DC)* **200**, 1477-1486.

Mixon R. B. (1985) Stratigraphic and geographic framework of uppermost Cenozoic deposits in the southern Delmarva Peninsula, Virginia and Maryland. *USGS Profess. Pap.* 1067-J.

Morel, F. M. M. and Hering, J. G. (1993) *Principles and Applications of Aquatic Chemistry.* John Wiley.

Mueller B. and Sigg L. (1990) Interaction of Trace Metals with Natural Particle Surfaces: Comparison between adsorption experiments and field measurements. *Aquatic Sci.* **52**, 75-92.

Muftikian R., Nebesny K., Fernando Q., and Korte N. (1996) X-ray Photoelectron Spectra of the Palladium-Iron Bimetallic Surface Used for the Rapid Dechlorination of Chlorinated Organic Environmental Contaminants. *Environ. Sci. Technol.* **30**, 3593-3596.

NAG Fortran Library, Mark 16 (1993), Numerical Algorithm Group Ltd., Wilkinson House, Jordan Hill Road, Oxford, UK OX2 8DR.

Olsen C. R., Lowry P. D., Lee S. Y., Larsen I. L., and Cutshall N. H. (1986) Geochemical and Environmental Processes Affecting Radionuclide Migration from a Formerly Used Seepage Trench. *Geochim. Cosmochim. Acta* **50**, 593-607.

Pabalan R. T., Turner D. R., and Bertetti F. P. (1994) *Sorption Modeling for High Level Waste Performance Assessment; NRC High-Level Radioactive Waste Research at CNWRA January-June, 1994.* Center for Nuclear Waste Regulatory Analyses, San Antonio.

Payne T. E., Davis J. A. and Waite T. D. (1994) Uranium Retention by Weathered Schists: The role of Iron Minerals. *Radiochim. Acta* **66/67**, 297-303.

Payne T. E., Davis J. A., and Waite T. D. (1996) Uranium Adsorption on Ferrihydrite – Effects of Phosphate and Humic Acid. *Radiochim. Acta* **74**, 239-243.

Price S. M. and Ames L. L. (1976) Transuranium Nuclides in the Environment. Publication SM-199/87, Int. Atomic Energy Agency.

Raven K. P., Jain A., and Loeppert R. H. (1998) Arsenite and Arsenate Adsorption on Ferrihydrite: Kinetics, Equilibrium, and Adsorption Envelopes. *Environ. Sci. Technol.* **32**, 344-349.

Redden G., Li J., and Leckie J. (1998) Adsorption of Uranium (VI) and citric acid on Goethite, Gibbsite, and Kaolinite: Comparing Results for Binary and Ternary Systems. In *Adsorption of Metals by Geomedia* (ed. E.A. Jenne), Chap. 13, pp. 291-315. Academic Press.

Reyes I. and Torrent J. (1997) Citrate-Ascorbate as a Highly Selective Extractant for Poorly Crystalline Iron Oxides. *Soil Sci. Soc. Am. J.* **61**, 1647-1654.

Riley R. G. and Zachara J. M. (1992) Chemical Contaminants on DOE lands and Selection of Contaminant Mixturesfor Subsurface Science Research. U.S. Department of Energy, Washington DC.

Rosentretter J. R., Quarder H. S., Smith R. W., and McLing T. (1998) Uranium Sorption onto Natural Sands as a Function of Sediment Characteristics and Solution pH. In *Adsorption of Metals by Geomedia* (ed. E.A. Jenne), Chap. 7, pp. 181-192. Academic Press.

Sayles G. D., You G., Wang M., and Kupferle M. J. (1997) DDT, DDD, and DDE Dechlorination by Zero-Valent Iron. *Environ. Sci. Technol.* **31**, 3448-3454.

Scherer M. M., Westall J. C., Ziomek-Moroz M., and Tratnyek P. G. (1997) Kinetics of Carbon Tetrachloride Reduction at an Oxide-Free Iron Electrode. *Environ. Sci. Technol.* **31**, 2385-2391.

Schwetmann U. (1964) Differenzierung der Eisenoxide des Bodens durch photochemische Extraktion mit saurer Ammoniumoxalate-Losung. *Z. Pflansenenahr. Dueng. Bodenk.* **105**, 194-202.

Seaman J. C., Bertsch P. M., and Schwallie L. (1999) In Situ Cr(VI) Reduction within Coarse-Textured, Oxide-Coated Soil and Aquifer Systems Using Fe(II) Solutions. *Environ. Sci. Technol.* **33**, 938-944.

Smith K. S. (1991) Factors Influencing Metal Sorption onto Iron-Rich Sediments in Acid-Mine Drainage. Ph.D. dissertation, Colorado School of Mines.

Sørensen J. and Thorling L. (1991) Stimulation by Lepidocrocite (γ-FeOOH) of Fe(II)-Dependent Nitrite Reduction. *Geochim. Cosmochim. Acta* **55**, 1289-1294.

Stratmann M. and Müller J. (1994) The Mechanism of the Oxygen Reduction on Rust-covered Metal Substrates. *Corr. Sci.* **36**, 327-359.

Tratnyek P. G. (1996) Putting Corrosion to Use: Remediating Contaminated Groundwater with Zero-Valent Metals. *Chem. Ind. (London)*, 499-503.

Tripathi V. S. (1983) Uranium Transport Modeling: Geochemical data and submodels. Ph.D. dissertation, Stanford University.

Waite T. D., Payne T. E., Davis J. A., and Sekine K. (1992) *Uranium Sorption: Alligator Rivers Analogue Proj., Final Rept., 13*. Australian Nuclear Science and Technology Organization.

Waite T. D., Davis J. A., Payne T. E., Waychunas G. A., and Xu N. (1994) Uranium (VI) adsorption to Ferrihydrite: Application of a surface complexation model. *Geochim. Cosmochim. Acta* **58**, 5465-5478.

Westall J. C., Černík M., and Borkovec M. (1998) Modeling Metal Speciation in Aquatic Systems. In *Metals in Surface Waters* (ed. H.E. Allen et. al), Chap. 10, pp. 191-216. Ann Arbor Press.

Westall J. C., Jones J. D., Turner G. D., and Zachara J. M. (1995) Models for Association of Metal Ions with Heterogeneous Environmental Sorbents. 1. Complexation of Co(II) by Leonardite Humic Acid as a Function of pH and $NaClO_4$ Concentration. *Environ. Sci. Technol.* **29**, 951-959.

Zachara J. M., Gassman P. L., Smith S. C., and Tayler, D. (1995) Oxidation and adsorption of $Co(II)EDTA^{2-}$ complexes in subsurface materials with iron and manganese oxide grain coatings. *Geochim. Cosmochim. Acta* **59**, 4449-4463.

Yamada J. and Matsuda H. (1973) Limiting Diffusion Currents in Hydrodynamic Voltammetry: III. Wall Jet Electrodes. *Electroanal. Chem. Interfacial Electrochem.* **44**, 189-198.